

**The Use of Nanoindentation to Determine Composite Interfacial Shear Strength
and the Effects of Environmental Aging**

by

David Claibourne Haeberle

Thesis submitted to the Faculty of
Virginia Polytechnic Institute and State University
in partial fulfillment of the requirements for the degree of

Master of Science
in
Engineering Science and Mechanics

John J. Lesko, Chair
Scott W. Case
Judy S. Riffle

June 8, 2001
Blacksburg, VA

Keywords: fiber-reinforced polymer composites, interfacial shear strength,
nanoindentation, microindentation, composite strength

The Use of Nanoindentation to Determine Composite Interfacial Shear Strength and the Effects of Environmental Aging

David Claibourne Haerberle

(ABSTRACT)

Fiber sizings are used to improve the performance of fiber-reinforced polymer composites made from low-cost fiber and matrix materials. Evaluation of three sizings, poly(vinylpyrrolidone) (PVP), a carboxyl modified polyhydroxyether (PHE), and a standard industrial sizing (G'), have revealed tremendous improvements in static mechanical and enviro-mechanical properties. The focus of this work is to determine if these improvements in performance can be ascertained from a micromechanical test for interfacial shear strength (IFSS) on as-processed materials. The accomplishment of this goal would create more information with fewer experiments and a need for less experimental materials. In this study, a nanoindenter uniquely outfitted with a blunt tip is effectively used to obtain microindentation results where the debond load is extracted directly from the experimental load-deflection curve. Shear lag and finite element analyses are used to evaluate the mechanics of the system, but both methods show limitations with regard to determining interfacial stresses in an experimental system. In the results obtained, the PHE and G' materials outperform the PVP in IFSS, but the bulk properties for PVP and PHE outperform the G' material, suggesting the presence of another dominant mechanism. Despite better retention of bulk properties after hygrothermal exposure, PHE experiences degradation in IFSS that PVP does not. The PHE loses 10% of its original IFSS after 576 hours of 65°C moisture exposure, while PVP improves by 25%. The tensile strengths for PHE and PVP decrease 7% and 10% respectively at 576 hours exposure. Finite element modeling shows that matrix swelling due to moisture absorption increases interfacial shear stresses, a finding supported by a comparison of wet and dry specimens subjected to equivalent aging times. Matrix

swelling is not, however, responsible for the increase in IFSS of the PVP material. The relationship between tensile strength and IFSS proves to be small as predicted by a tensile strength model, but processing defects and other failure processes that are not included in the tensile strength model appear to have strong influences over the experimental results. IFSS is important in composite materials, but in the case of the G', PHE and PVP materials, other factors dominate fiber direction tensile performance. Therefore, this one simple micromechanical test provides significant insight into the composite material behavior, but it does not provide the same magnitude of information as from bulk composite experiments.

Acknowledgements

The accomplishment of this work would not have been possible without the support of many people. First, I would like to thank my parents, Ron and Harriet Haerberle, for their support and encouragement over the years, allowing me to grow and learn as an individual. Jack Lesko, my advisor, has provided me with tremendous insight and plenty of work experience over the past several years, all of it very enjoyable, and I could not have asked for much more out of my graduate experience. My other committee members, Scott Case and Dr. Judy Riffle, have offered excellent support, lending me their knowledge and previous work to guide me through the project. The folks of the Materials Response Group and Dr. Riffle's group in chemistry, have given me help every step of the way, so I would like to acknowledge Tozer Bandorawalla, John Bausano, Maggie Bump, Jason Burdette, Art Callahan, Rob Carter, Howard Halverson, Linda Harris, Michael Hayes, David Jungkuist, Mac McCord, Don Ohanehi, Sneha Patel, Steve Phifer, Blair Russell, Jolyn Senne, Austin Smith, Tim Schniepp, Joseph South, and Brian Starr. I would also like to pay a special thanks to Beverly Williams and Shelia Collins for their constant help and support, and also to Pat Baker, Wanda Robertson, and Paul Sibert, whose lives I seemed to make difficult at least once a week. Last, but certainly not least, I would like to thank and acknowledge Dr. Nikhil Verghese for his ideas, direction, and enthusiasm. Nikhil worked with me through the beginning of this project and has continued his support. I am looking forward to becoming is neighbor in Texas.

This work would not have been possible without the financial support of the Oak Ridge National Laboratory and intellectual support of our contacts there, Dr. J. Greg Swadener and Dr. George Pharr. Research at the Oak Ridge National Laboratory SHaRE User Facility was sponsored by the Division of Materials Sciences and Engineering, U.S. Department of Energy, under contract DE-AC05-00OR22725 with UT-Battelle, LLC, and through the SHaRE Program under contract DE-AC05-76OR00033 with Oak Ridge Associated Universities. This work was also sponsored in part by the National Science Foundation under CMS-9713943.

Table of Contents

Acknowledgements.....	iv
List of Figures.....	vii
List of Tables	xi
Chapter 1 Introduction and Motivation	1
1.1 Introduction	1
1.2 Background	3
1.2.1 Fiber Sizings	3
1.2.2 Pultrusion.....	4
1.2.3 Static Mechanical Testing.....	5
1.2.4 Enviro-Mechanical Testing.....	8
1.2.5 Summary	12
Chapter 2 Literature Review	13
2.1 Introduction	13
2.2 Tests For Interfacial Adhesion	13
2.3 Microindentation	15
2.4 Tensile Strength Modeling.....	36
2.5 Summary	37
Chapter 3 Objectives.....	38
3.1 Project Objectives.....	38
Chapter 4 Materials and Experimental Procedure.....	40
4.1 Materials.....	40
4.2 Experimental	42
4.2.1 Hygrothermal Aging.....	42
4.2.2 Mechanical Fatigue	42
4.2.3 Tensile Testing.....	43
4.2.4 Specimen Polishing and Preparation.....	43
4.2.5 Nanoindentation	44
4.3 Analysis Procedure	50

4.3.1 Data Reduction.....	50
4.3.2 Statistical Analysis	51
Chapter 5 Results and Discussion.....	53
5.1 Evaluation of the Nanoindentation Technique.....	53
5.1.1 Sample Polishing.....	53
5.1.2 Resolution of the Nanoindenter	54
5.1.3 Selection of Indenter Tip	55
5.1.4 Continuous Stiffness Measurements	56
5.1.5 Verification of Debonding.....	57
5.2 Evaluation of Analysis Method.....	60
5.2.1 Finite Element Analysis.....	60
5.2.2 Inclusion of Poisson’s Effect in Shear Lag Analysis	68
5.3 Comparison of Fiber Sizings.....	72
5.3.1 Effect of Fiber Sizings on Interfacial Shear Strength.....	72
5.3.2 Comparison to Microbond Technique.....	73
5.3.3 Tensile Strength Predictions	74
5.4 Effects of Hygrothermal Aging on IFSS and Composite Strength	77
5.4.1 Effect of Hygrothermal Aging on Interfacial Shear Strength.....	77
5.4.2 Evaluation of Matrix Swelling using a Finite Element Analysis	83
5.4.3 Comparison of IFSS to Tensile Strength in Hygrothermally Aged Samples .	88
5.4.4 Tensile Strength Predictions	90
5.5 Effect of Mechanical Fatigue on IFSS and Composite Strength.....	92
Chapter 6 Conclusions	93
6.1 Conclusions	93
6.1.1 Evaluation of Technique and Analysis Methods	93
6.1.2 Comparison of Fiber Sizings	93
6.1.3 Effects of Hygrothermal Aging on IFSS and Composite Strength	94
6.1.4 Summary.....	95
6.2 Recommendations for Future Work	95
References.....	97
Vita	101

List of Figures

Figure 1-1. Chemical Structure for the PVP Repeat Unit	4
Figure 1-2. Chemical Structure for the PHE Repeat Unit.....	4
Figure 1-3. Normalized Tensile Strength Results for Composites with Different Sizings	6
Figure 1-4. Shear Response of Laminates with Different Sizings.....	7
Figure 1-5. Moisture Uptake Curves for the Individual Unidirectional Composites Aged by Immersion in a 65°C Water Bath	8
Figure 1-6. Remaining Strength of Moisture Saturated Composite Specimens	10
Figure 1-7. Stress Normalized ‘S-N’ Curves for the Individual Unidirectional Composites, $R = 0.1$ and Frequency = 10Hz	11
Figure 1-8. Fatigue Life of Saturated vs. Unsaturated Composite Laminates.....	12
Figure 2-1. Load-Displacement Curve for Single Fiber using Nanonindenter	20
Figure 2-2. Load Displacement Curve showing Fiber Splitting	20
Figure 2-3. Finite Element Model Description.....	24
Figure 2-4. Load-Displacement from a Single Fiber using Microindentation	27
Figure 2-5. Illustration of Displacement Components in Microindentation	27
Figure 2-6. Reduced Indentation Curve, Experimental and Fit.....	28
Figure 2-7. Reduced Indentation Curve with Weak Interface	34
Figure 2-8. Reduced Indentation Curve with Progressive Debonding.....	35
Figure 2-9. Predicted Normalized Strength versus Interface/Matrix Yeilding Stress	37
Figure 4-1. Photograph of NANO II Indenter at ORNL	45
Figure 4-2. Schematic of the NANO II Indenter	46
Figure 4-3. SEM Image of Tip Indent in Epoxy Substrate.....	46
Figure 4-4. Polished Specimen for Nanoindentation	48
Figure 4-5. Indentation Region shown in Microscope Image	48
Figure 4-6. G' Single Fiber Load-Deflection Curve.....	49
Figure 4-7. G' Single Fiber Stiffness-Load Curve from Continuous Stiffness Measurement.....	49
Figure 4-8. Curve Fits to Experimental Load-Deflection Curve through the Analysis of Zidi et. al.....	51

Figure 4-9. Weibull Probability Distribution Function of G' Sized Fiber Interfacial Shear Strength.....	52
Figure 5-1. SEM Image of Polished Carbon/Vinyl Ester Surface (Large Field).....	53
Figure 5-2. SEM Image of Polished Carbon/Vinyl Ester Surface (Narrow Field).....	54
Figure 5-3. Nanoindentation Load-Displacement Curve for G' with Berkovich Indenter	55
Figure 5-4. Description of Fiber/Matrix Behavior during Indentation Test.....	57
Figure 5-5. G' Single Fiber Load-Displacement Curves, Increasing Maximum Load	58
Figure 5-6. G' Single Fiber Stiffness-Load Curve, Increasing Maximum Load	59
Figure 5-7. Progressive Debonding of the G' Fiber (a) 0 mN (b) 65 mN (c) 70 mN.....	59
Figure 5-8. SEM Image of Fiber/Matrix Debond as a Result of Microindentation.....	59
Figure 5-9. Schematic for the Finite Element Analysis	60
Figure 5-10. SEM Image of G' Fiber Evaluated using FEA	62
Figure 5-11. Optical Microscope Image of LSP Fiber Evaluated using FEA	62
Figure 5-12. Comparison between FEA and Shear Lag Interfacial Shear Stress Distributions for LSP and G' Composites	63
Figure 5-13. Comparison between FEA and Shear Lag Fiber Translation Distributions for LSP and G' Composites	63
Figure 5-14. Indentation across a Bi-Layer Blend of PHE and Vinyl Ester	65
Figure 5-15. Effect of Matrix Thickness on Fiber Translation in G' Material.....	66
Figure 5-16. Effect of Matrix Thickness on Interfacial Shear Stress in G' Material.....	66
Figure 5-17. Effect of Fiber Diameter on Fiber Translation in the G' Material.....	67
Figure 5-18. Effect of Fiber Diameter on Interfacial Shear Stress in the G' Material.....	68
Figure 5-19. Fiber Poisson's Expansion Affect on Interfacial Shear Stress and Fiber Translation through Analytical Interpretation.....	71
Figure 5-20. Weibull Cumulative Distribution Curves for the IFSS of Different Fiber Sizings.....	72
Figure 5-21. Comparison of Composite Tensile Failure for Two Different Fiber Sizings, PVP and PHE	74
Figure 5-22. Predicted Tensile Strength versus Interfacial Shear Strength.....	75
Figure 5-23. Comparison of Experimental and Predicted Tensile Strength Values	76

Figure 5-24. Moisture Uptake Curves for Composites in 65°C Water Bath	77
Figure 5-25. Weibull Cumulative Distribution Curves for LSP Aged in 65°C at for Different Aging Times.....	79
Figure 5-26. Weibull Cumulative Distribution Curves for PVP Aged in 65°C at for Different Aging Times.....	79
Figure 5-27. Weibull Cumulative Distribution Curves for G' Aged in 65°C at for Different Aging Times.....	80
Figure 5-28. Weibull Cumulative Distribution Curves for LSP Aged 288 hours in a 65°C Water Bath, Tested Wet and Dry	81
Figure 5-29. Weibull Cumulative Distribution Curves for LSP Aged 576 hours in a 65°C Water Bath, Tested Wet and Dry	81
Figure 5-30. Weibull Cumulative Distribution Curves for PVP Aged 288 hours in a 65°C Water Bath, Tested Wet and Dry	82
Figure 5-31. Weibull Cumulative Distribution Curves for PVP Aged 576 hours in a 65°C Water Bath, Tested Wet and Dry	83
Figure 5-32. Increase in Radial Stresses on the Fiber due to Matrix Swelling	84
Figure 5-33. Change in Interfacial Shear Stresses due to Matrix Swelling.....	85
Figure 5-34. Change in Fiber Translation due to Matrix Swelling.....	85
Figure 5-35. Translations of Fibers with Equivalent n values: (1) due to higher local volume fraction, (2) due to matrix swelling.....	87
Figure 5-36. Interfacial Shear Stresses of Fibers with Equivalent n values: (1) due to higher local volume fraction, (2) due to matrix swelling	87
Figure 5-37. Comparison of LSP IFSS to Tensile Strength at Different Aging Times in a 65°C Water Bath.....	89
Figure 5-38. Comparison of PVP IFSS to Tensile Strength at Different Aging Times in a 65°C Water Bath.....	89
Figure 5-39. Comparisons of Actual Tensile Strengths and Predicted Tensile Strengths from IFSS Results for LSP Material at Different Aging Times.....	91
Figure 5-40. Comparisons of Actual Tensile Strengths and Predicted Tensile Strengths from IFSS Results for PVP Material at Different Aging Times	91

Figure 5-41. Weibull Cumulative Density Curves for LSP and G' Composites: Control
versus Mechanically Fatigued..... 92

List of Tables

Table 1-1. Summary of Static Mechanical Properties.....	7
Table 1-2. Equilibrium Moisture Content and Diffusivities for Sized Fiber Composites ..	9
Table 2-1. Experimental Results	17
Table 2-2. Material Properties	18
Table 2-3. Nanoindentation Results	22
Table 2-4. Microindentation Results using Shear Lag Analysis Method.....	33
Table 4-1. Basic Properties for the Pultruded Composites and Components.....	41
Table 4-2. Buehler Polishing Procedure.....	44
Table 5-1. Resolutions of Instruments used for Microindentation	55
Table 5-2. Properties for the Finite Element Analysis	61
Table 5-3. Normal and Weibull Results for Intefacial Shear Strength	73
Table 5-4. Comparison of Nanoindentation and Microbond Results for IFSS	73
Table 5-5. Tensile Strength Model Input Parameters	75
Table 5-6. Interfacial Shear Strength Values for Hygrothermally Aged Specimens.....	90

Chapter 1 Introduction and Motivation

1.1 Introduction

Fiber-reinforced polymer composites are being used more frequently in civil infrastructure, automotive, and offshore oil applications where rapid processing, reduced cost, and environmental resistance are important requirements. Materials created for these applications must utilize low-cost components while maintaining the strength, stiffness, and resistance to enviro-mechanical exposure of their high cost predecessors. Rapid evaluation of these materials is also very important to helping screen various prototypical materials for given applications before an extensive analysis is completed. Very often micromechanical predictions of strength and modulus are obtained based on fiber and matrix properties, and the fatigue and environmental resistances are calculated for composite shapes and laminates based upon more sophisticated life prediction techniques.

The fiber/matrix interface or interphase is the region in the composite material that strongly influences strength and durability. As the interphase degrades due to fatigue or environmental exposure, so does the strength of the material. The ability to manipulate and evaluate this area of the material is very important in the effort to make high-quality/low-cost composites from low-quality/low-cost components. The Designed Interphase Group at Virginia Tech has created fiber sizings, coatings applied to the individual fibers, that have lead to improved processability, the creation of a durable interphase region, and ultimately greater strength and life.

The evaluation of these composites involved a series of tests, including tensile tests, compression tests, and fatigue tests on both as-processed samples as well as hygrothermally aged ones. This study required large amounts of materials and a significant time commitment to show the improvements resulting from the new fiber sizings. The need exists for a small-scale test that can evaluate many of the same

properties with minimal amounts of time and material expense. An experimental test that evaluates fiber/matrix interfacial properties would be such a test.

Several techniques exist that evaluate the fiber/matrix interface and measure interfacial shear strength, one of the dominant interface properties affecting composite strength and life. There is only one test, however, that measures interfacial shear strength in as-processed composites: microindentation. Many other techniques utilize single fibers embedded in a matrix, but those techniques do not capture the effects of processing conditions or the influence of neighboring fibers. Microindentation can be used on many types of composites, with various fibers, matrices, sizing materials, and environmental histories. While this technique is very advantageous, several disadvantages exist, such as experimental difficulty, the complex stress-state, and the inability to detect interfacial failure easily.

The focus of this work is to improve the microindentation technique in order to evaluate the composites manufactured using the sizings developed by the Designed Interphase Group at Virginia Tech. The technique will be improved by building upon the work of other authors in the field, focusing on equipment and analysis of results. Attempts will be made at simplifying the experimental process, making the test attractive to those needing to evaluate prototypical composite materials. The interfacial shear strength results are related to bulk composite properties through a tensile strength prediction model. Samples subjected to fatigue loading and hygrothermal exposure are also evaluated with their microindentation properties compared to their respective residual tensile strengths.

1.2 Background

A major thrust of composites research at Virginia Tech has been in the area of civil infrastructure. Researchers have evaluated various bridge support girders and bridge decks for potential use in the near future and have even implemented composite materials at two field sites on actual roadways [1-4]. The materials are processed through a method of pultrusion and are composed of low-cost polymer resins, carbon fibers, and glass fibers. Test material, processed in the same pultrusion process, was created to evaluate the effects of two new thermoplastic sizings on processing, mechanical performance, and enviro-mechanical durability. The results were compared to a control fiber, sized with a standard industrial thermosetting fiber sizing. All tests were completed on carbon fibers in a vinyl ester matrix.

1.2.1 *Fiber Sizings*

Fiber sizings are a thin coating applied to the fiber surface before matrix impregnation, originally applied to improve the handling of the fiber and to aid in processing. It has been shown that fiber sizings can affect mechanical performance and can do so in many different ways [5]. An unsized carbon fiber is very brittle and susceptible to damage, but once a sizing is applied, the fiber tow is more pliable and easier to handle in a production situation. A good fiber sizing does three things for processability: (1) protects the fiber, (2) improves fiber alignment, and (3) improves fiber wettability. The fiber sizing can also improve the performance of the composite through material improvements, such as fiber/matrix adhesion and interphase formation [5]. Using tensile failure of a unidirectional specimen as an example, when a fiber breaks the load is transferred back into the fiber through the interphase and surrounding matrix. In this transfer zone, the surrounding composite is in a higher stress state, which increases the probability of additional fiber failure. If the shear stress level at the fiber/matrix interface in the transfer zone overcomes the interfacial shear strength, a crack propagates up the fiber expanding the transfer zone, and thus increases the probability of additional fiber failure. Therefore, good fiber/matrix adhesion is important to improving a material

by a fiber sizing. The formation of an interphase, with its gradient of properties, is also important to composite strength. Following the same example, after the fiber breaks a stress concentration is formed by the resulting penny-shaped crack. The resistance of the interphase to transverse crack propagation is important in preventing surrounding fibers from feeling the effects of the stress concentration that could ultimately lead to additional fiber failure. Due to the brittle nature of vinyl ester when compared with its more expensive counterpart, epoxy, thermoplastic sizings are studied to improve interfacial adhesion and interphase toughness.

Three different fiber sizings were applied to Hexcel AS-4 fibers for comparison: K-90 poly(vinylpyrrolidone) (PVP), a carboxyl modified polyhydroxyether of bisphenol A (PHE), and the standard industrial sizing, an epoxy oligomer (G', applied by Hexcel). The thermoplastic sizings, PVP and PHE, were applied as discussed in Broyles et al. [5], and their respective repeat units are shown in Figure 1-1 and Figure 1-2. The PHE was applied in two different ways, low spread (LSP) and high spread (HSP), differing based on the tow tension during the sizing operation. Results are reported for both the LSP and HSP materials.

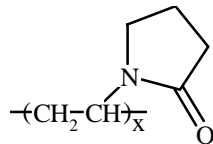


Figure 1-1. Chemical Structure for the PVP Repeat Unit [6]

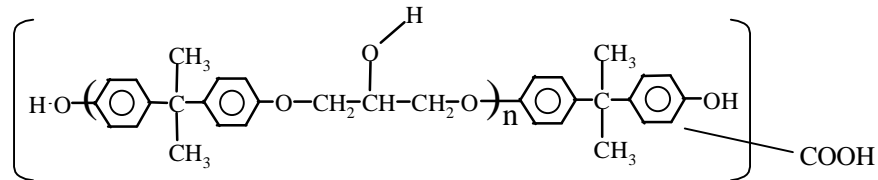


Figure 1-2. Chemical Structure for the PHE Repeat Unit [6]

1.2.2 Pultrusion

Pultrusion is a rapid processing technique for components with constant cross-sectional shapes and sizes. It is one of the few techniques that is currently fast and cost-effective enough to support the industries that are investigating low-cost composite materials, such as civil infrastructure. In this process, spools of fiber are pulled through a resin dip bath and then a heated/shaped die where resin material is cured very rapidly. The completed composite part emerges from the exit port of the die. The samples created to evaluate the effects of fiber sizings were impregnated with Derakane 411-35 LI vinyl ester oligomer supplied by the Dow Chemical Company, comprised of 42 wt% monomer, 42 wt% styrene, 15 wt% fillers such as clay, 0.5 wt% release agents, and 0.5 wt% of a proprietary initiator package. The resulting shape was 12.7 mm wide by 2.0 mm thick and pultruded at 10 mm/sec [5].

Differences were noted in processing due to the sizings applied to the carbon fiber. The G' fibers suffered extensive fiber fraying and damage in the process that resulted in a rough surface finish with fiber breaks and kink-bands readily observed. The LSP, HSP, and PVP fibers all processed very efficiently with no fiber damage or fraying. The wettability of the fiber with the matrix resin also appeared to improve with the thermoplastic sizings. The resulting composite had a very glassy surface finish without any trace of fiber breaks [5].

1.2.3 Static Mechanical Testing

Experiments were conducted to characterize the results of processing differences and material improvements due to the fiber sizings. Static mechanical tests were conducted to evaluate tensile strength, tensile modulus, compression strength, compression modulus, and shear strength. Results from these tests are reported in Table 1-1. Quasi-static tension tests were performed as described in Broyles et al. [5]. The results, shown in Figure 1-1, clearly demonstrate the improvement in tensile strength by the thermoplastic sizings with all of them outperforming G' by at least 25%. No

appreciable change in composite modulus was discovered (HSP: 121.7 GPa, PVP: 125.2 GPa, and G': 120.3) when normalized to the G' volume fraction.

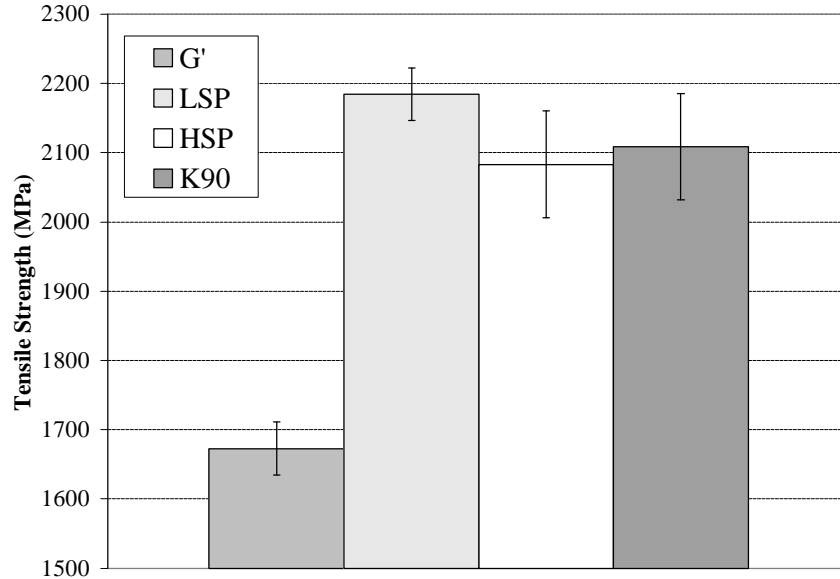


Figure 1-3. Normalized Tensile Strength Results for Composites with Different Sizings [5]

Compression Tests were executed in accordance with ASTM D 3410 [7]. The compressive strength and moduli were determined for the LSP, PVP, and G' materials and reported in Table 1-1. The compressive strength of the thermoplastic sized fiber composites was shown to be 31% greater than that of the G' composite. The average fiber misalignment angle, which plays a major role in compression strength, was 3.0 degrees for the G' composite versus 1.2 degrees for the LSP composite. The kink-bands observed in the G' composite during processing can also significantly affect the compressive strength of the material. The compressive moduli were found to be statistically equal at about 122 GPa, which is equivalent to the tensile moduli [5].

Data was also obtained on $\pm 45^\circ$ laminates manufactured using a resin infusion molding process [8]. These laminates were used to obtain shear data through simple tensile tests, and the results are presented here because they show the strong influence of the fiber sizing on composite performance. Figure 1-4 shows the representative shear

stress-strain curves for the LSP, PVP, and G' sizings. Two interesting observations can be readily made. First, the response changes from the brittle behavior for the G' sizing to elastic-perfectly plastic behavior for the PVP sizing, resulting in a large increase in the strain-to-failure. Second, in the case of the G' composite, upon reaching a critical strain, surface cracks develop that shortly lead to complete failure. For the PVP, however, crack saturation occurs and results in the system being pulled in a plastic manner until failure. In addition to the change in loading response, the shear modulus and strength appear to be different.

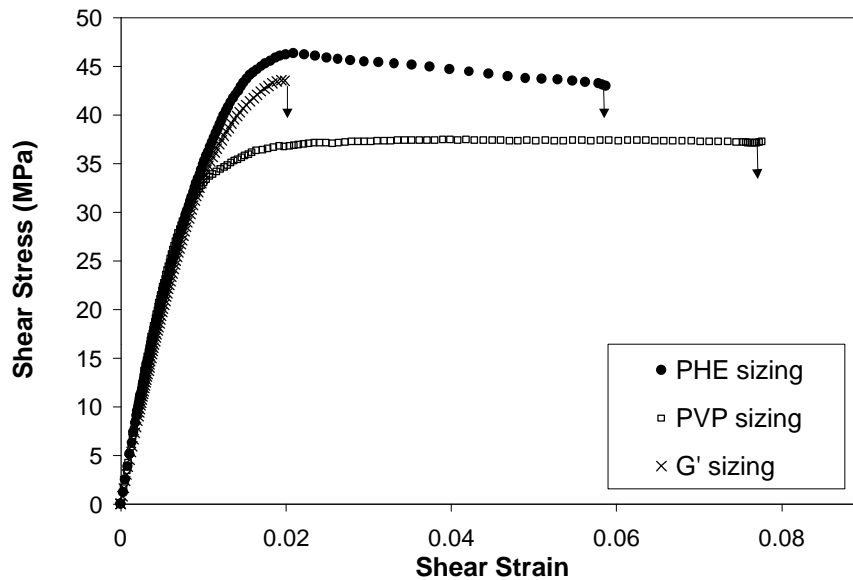


Figure 1-4. Shear Response of Laminates with Different Sizings [8]

Table 1-1. Summary of Static Mechanical Properties [5]

Property	G'	LSP	HSP	PVP
Fiber Volume Fraction (%)	60.8	57.7	52.9	55.8
Tensile Strength (MPa)	1673 ± 39	2035 ± 35	1940 ± 72	1964 ± 71
Normalized Strength (MPa)*	1673 ± 39	2185 ± 38	2083 ± 77	2109 ± 76
Tensile Modulus (GPa)	120.3	NA	105.0	113.3
Normalized Modulus (GPa)*	120.3	NA	121.7	125.2
Strain-to-Failure (%)	1.47 ± 0.08	1.41 ± 0.09	1.08 ± 0.46	1.33 ± 0.11
Compressive Strength (MPa)	747 ± 110	913 ± 98	NA	932 ± 84
Normalized Strength (MPa)*	747 ± 110	980 ± 105	NA	1000.5 ± 90
Compressive Modulus (GPa)	136 ± 13	121 ± 13	NA	116 ± 15
Normalized Modulus (GPa)*	136 ± 13	135 ± 14	NA	130 ± 17

*Normalized properties normalized to the G' Volume Fraction

1.2.4 Enviro-mechanical Testing

In order to evaluate how the fiber sizing affects moisture absorption and retention of static mechanical properties in actual composites, unidirectional pultruded composite specimens were placed in a 65°C tap water bath. The moisture uptake curves for the individual samples are shown in Figure 1-5. The composites with the G' sizing absorbed the highest amount of water. This result, although not completely surprising, did initially prove to be difficult to understand especially when compared against the PVP sizing, which is known to be hydrophilic. The relatively poor processability of the G' sized composites could be a cause for this large uptake. The moisture uptake data was used to evaluate the diffusivity (Table 1-2). The solid line in Figure 1-5 is the 1-D Fickian fit to the absorption data [9].

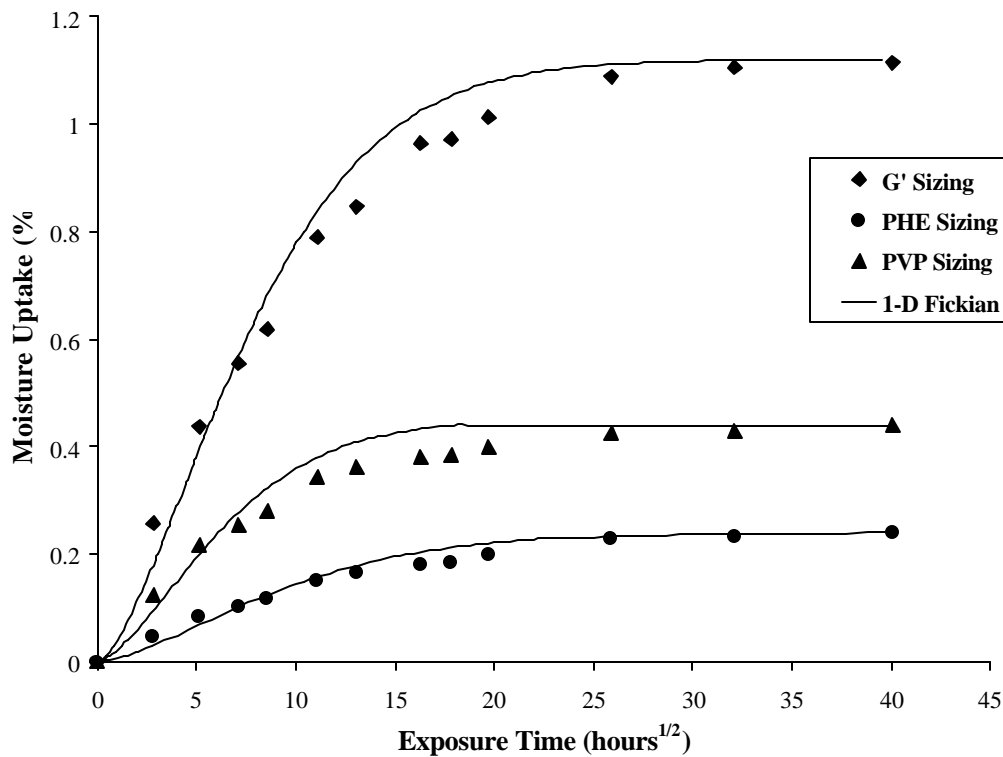


Figure 1-5. Moisture Uptake Curves for the Individual Unidirectional Composites Aged by Immersion in a 65°C Water Bath [9]

Table 1-2. Equilibrium Moisture Content and Diffusivities for Sized Fiber Composites [9]

Specimen	Diffusivity, D_z (cm^2/sec)	Equilibrium Moisture Content, M_∞ (%)
PHE Sizing	6.2×10^{-9}	0.24
PVP Sizing	1.3×10^{-8}	0.45
G' Sizing	8.7×10^{-9}	1.12

After saturation in the 65°C tap water bath, static mechanical properties were measured on the aged material. Figure 1-6 shows the changes in tensile strength after saturation for the different composites. The ordinate in the figure has been normalized with respect to the particular composite's tensile strength prior to aging. As seen in the figure, although the G' composite has the highest diffusivity and moisture content its tensile strength did not greatly reduce as compared to the thermoplastic fiber sized composites that had lower moisture contents. This result again leads to speculation that the poor processability of the G' composites resulted in the formation of voids that acted as reservoirs for water entrapment during moisture uptake. It is believed that there was preferential moisture absorption in the interphase region of the two thermoplastic sized composites. Since the processing was of superior quality with the thermoplastic sizings, the nature of the sizing resin made the difference in mechanical durability. As noted previously, PVP is an extremely hydrophilic polymer whereas PHE tends to be hydrophobic. It is clear from the location of the absorbed water (the interphase), that the residual strength of the PVP composite should be lower than the PHE, proof of which is shown in Figure 1-6 [9].

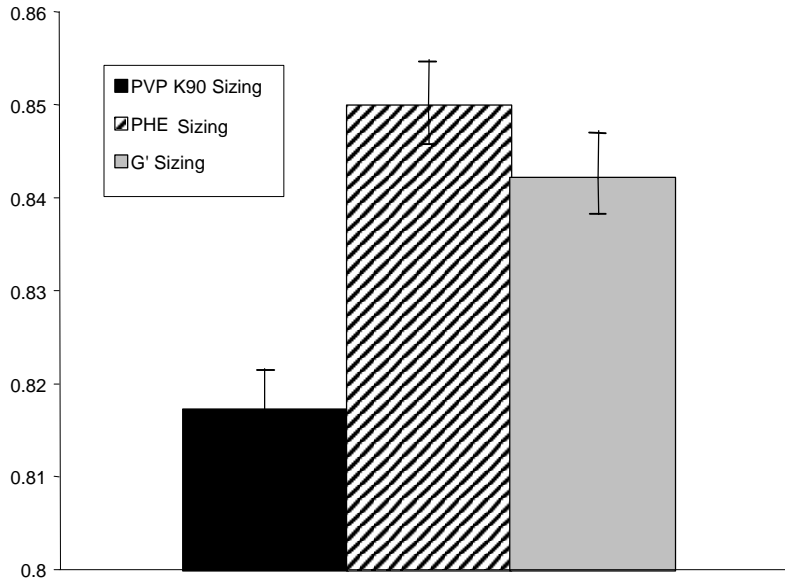


Figure 1-6. Remaining Strength of Moisture Saturated Composite Specimens [9]

The effect of the fiber sizing on mechanical fatigue and fatigue coupled with moisture saturation is also of interest. Cyclic fatigue tests were performed on PHE, PVP, and G' composites on an MTS test frame under sinusoidal loading. The frequency of the test was 10 Hz with an R-ratio equal to 0.1, tension-tension loading. Figure 1-7 shows the resulting S-N curve, which indicates the number of cycles to failure obtained on the material subjected to fatigue at some fractional load compared to its ultimate tensile strength. In the figure, the stress axis is normalized with respect to each composite's ultimate strength in order to facilitate fair comparison of the data. Although the two thermoplastic sizings are comparable, the life of the industrial G' sized composite is consistently lower than that of the two thermoplastic sizings. Thus, once again the thermoplastic sizings out performed the industry standard in a key material property [9].

Notched composite cross-ply laminates sized with PHE were evaluated under a combination of moisture and fatigue to determine the resistance of the thermoplastic sized composites to the coupled effects. The samples were saturated in a 65°C tap water bath and then tested on an MTS load frame under sinusoidal loading with $R = -1$ (tension-compression loading). The results, shown in Figure 1-8, indicate that moisture saturation

does not decrease the fatigue life of the composite laminates and confirms again the benefits attained by the use of the PHE sizing [9].

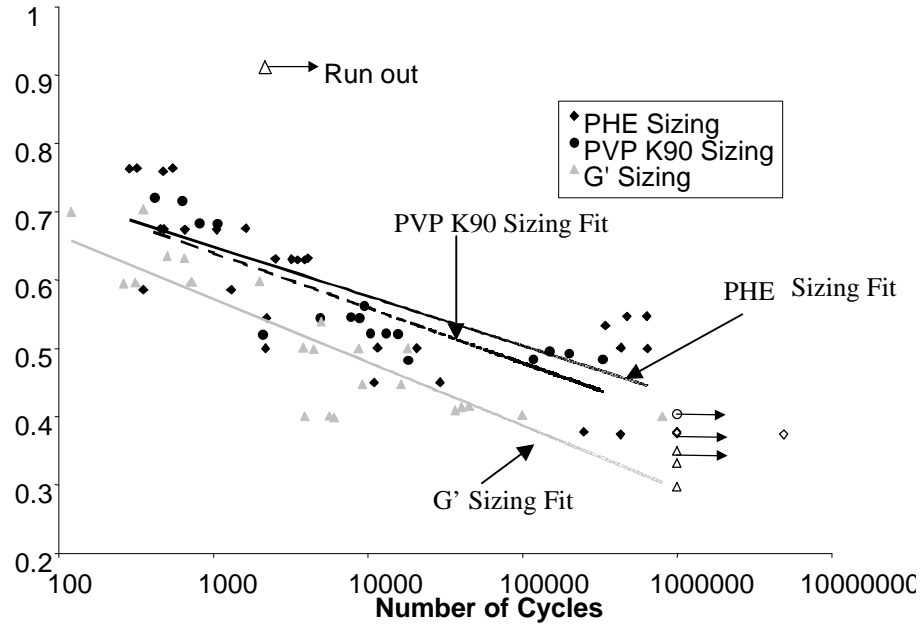


Figure 1-7. Stress Normalized ‘S-N’ Curves for the Individual Unidirectional Composites, R = 0.1 and Frequency = 10 Hz [9]

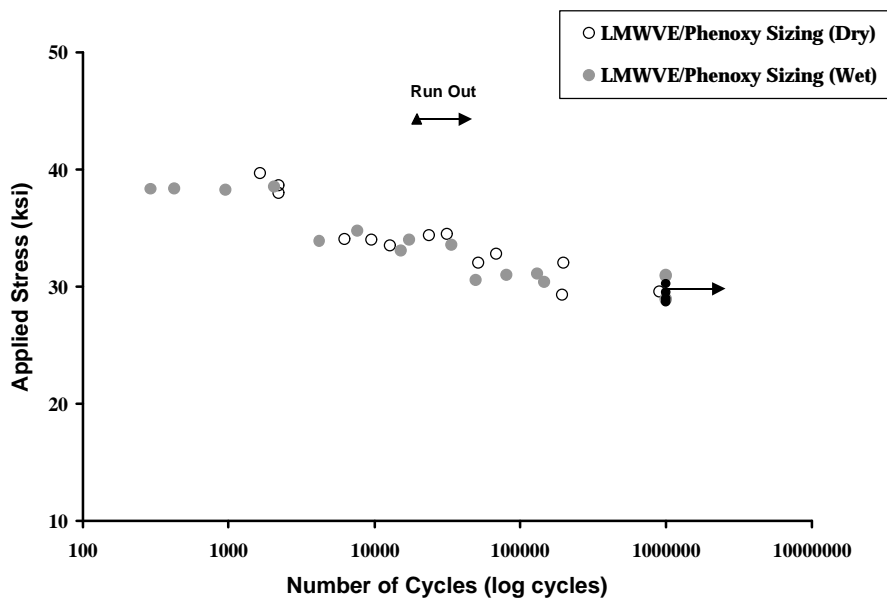


Figure 1-8. Fatigue Life of Saturated vs. Unsatrated Composite Laminates [9]

1.2.5 Summary

Unidirectional, pultruded composites were systematically altered by the use of two different thermoplastic sizings: PVP and PHE. Results of static mechanical tests and fatigue tests suggest that the performance of the two thermoplastic sizings (particularly the PHE) is superior to that of the commercial G' sizing. Additionally, processibility is improved. Results for hygrothermal aging followed by fatigue loading suggest that the performance of the composites with the PHE sizing is unaffected by the presence of the moisture. The ability to predict the durability of these composites based on the influential interphase properties will allow for the design of an interphase that optimizes the components produced for transportation and infrastructure. There are currently several techniques available to measure adhesion at the fiber/matrix interphase, each with their own advantages and disadvantages.

Chapter 2 Literature Review

2.1 Introduction

The measurement of interfacial shear strength, IFSS, has been accomplished in many different ways, each method with its own advantages and disadvantages. The ultimate goal is to determine an accurate measurement of interfacial shear strength so that fiber-reinforced polymer materials can be compared based on their interfacial adhesion. Interfacial adhesion is important because it is a critical component in the strength of a composite material along with fiber and matrix properties. In fact, several researchers have included interfacial shear strength in their analytical tensile strength models.

2.2 Tests for Interfacial Adhesion

Various authors have evaluated the different techniques developed to determine interfacial shear strength [10-11]. Fiber pull-out, single-fiber fragmentation, and microindentation are three of the main techniques used to determine IFSS. Fiber pull-out, similar in theory to the microbond technique, involves embedding a single fiber in a matrix block, disk, or bead. The fiber is then steadily loaded with an increasing force until pull-out occurs or the fiber fractures. The load and displacement of the fiber are monitored in order to determine the load at which the fiber slips. The interfacial shear strength is then extracted using a shear lag analysis to calculate the maximum shear stress at the failure load [12]. In the single-fiber fragmentation test, a single fiber is embedded in a tensile specimen of matrix material. The tensile specimen is loaded in a normal fashion, and the loading results in multiple fiber fractures. The sample is loaded until no more fiber fractures occur, and the final fiber length, called the critical length, is measured and converted to an average shear strength based on a force balance [13]. The microindentation test is performed on composite samples that have been cut and polished, producing a smooth surface perpendicular to the fiber direction. An individual fiber is then put in compression using an indenter tip. The debond load is then extracted from either visual observation of the fiber/matrix interface or from the load-deflection curve.

The load is then converted into interfacial shear strength by a shear lag or finite element analysis [10].

According to Franco and Drzal [10], the advantages of the fiber pull-out, microbond technique are that the force at the moment of debonding can be measured and the technique can be used on almost any fiber/matrix combination. There are, however, numerous disadvantages to this method. The debonding force is proportional to the embedded length of the fiber, which creates two difficulties: (1) the fiber can only be embedded short distances due to problems with fiber breakage, and (2) measuring the embedded fiber depth can be problematic due to the meniscus that forms between the fiber and matrix at the surface. The meniscus may also be responsible for affecting the interfacial stresses on the fiber, and if the meniscus fails prematurely, it can lead to premature debonding between the fiber and matrix. In addition to the physical limitations of this interfacial adhesion test, it has been shown that the mechanical properties in the microdrop of matrix will vary depending on size, thus further affecting the results. Results are often highly scattered due to the many parameters and variables involved [10]. Narkis, Chen and Pipes [11] have also noted in their research the problems of short embedment length, large data scatter, and a non-uniform shear stress distribution along the interface with this method.

Single-fiber fragmentation is a test that can yield large amounts of data that can be studied statistically. The test represents what happens to a fiber when loaded *in situ* in a composite material. The failures can actually be observed with polarized light when transparent matrices are used. There are fewer parameters involved in the analysis of interfacial properties in this test than in the fiber pull-out procedure, making it more robust. One of the biggest limitations to single-fiber fragmentation is that the matrix must have a strain limit at least three times greater than that of the fiber. The matrix should also have sufficient toughness to avoid fracture when a fiber break occurs within the specimen. Another deficiency of this method is that the state of stress at the interface is very complicated due to the many cracks formed as a result of fiber breaks. This complicated state of stress is oversimplified in the effort to determine interfacial shear

strength. Other effects, such as Poisson effects, can result in misleading interfacial shear strength numbers. The contraction of the matrix due to Poisson effects increases transverse normal forces on the fiber, resulting in incorrectly higher numbers for strength [10]. Narkis et al. [11] adds that the method depends on fiber tensile strength and that the results are scattered due to the wide distribution of fiber fragment lengths obtained.

The microindentation technique's main advantage is the ability to make *in situ* measurements of interfacial shear strength, thus allowing the researcher to evaluate a composite in its post-processed form. This technique is fast and automated, making it simple to obtain multiple data points rather quickly. However, as the fiber is loaded and failed it is not possible to observe the failure mode or location of failure, which can be a major disadvantage when evaluating various fiber/matrix systems. There is also the possibility of creating damage to the interface through the surface polishing procedure that could cause misleading results. As with all of these interfacial tests, there is some doubt that the assumptions made to calculate the interfacial shear strength are completely valid [10]. Another disadvantage in this method is that the loading mechanism can cause splitting or crushing of the fiber, limiting the types of fibers tested [11].

2.3 Microindentation

The microindentation method, described briefly in the previous section, is a very important tool because it measures interfacial shear strength values on actual composites. This gives the researcher the ability to evaluate the effects of processing and environment on the interfacial adhesion. The authors who have explored microindentation have done so with various types of hardware and analysis methods. There is much agreement among the authors on the difficulties of the experiment, but there is yet to be a standard procedure for this technique.

Mandell et al. [14] developed the microindentation test as an improvement over other interfacial test methods that did not investigate realistic composites. The lack of knowledge on interfacial shear strength often prevented consideration of this property in many studies, such as tensile strength models. The vision for microindentation was to

provide the ability to monitor the effects of fatigue and environment on interfacial degradation and possibly use the technique for failure analysis or monitoring of parts in service.

The procedure described by Mandell et al. [14] has been generally followed in subsequent investigations of the microindentation technique. The samples were prepared utilizing standard metallographic polishing techniques, where the composites are potted in a polyester resin with the fibers perpendicular to the surface. The potted specimens were polished with alumina (down to 0.05 μm particle size) with rayon bonded cotton cloth or diamond compound on silk cloth. The samples were secured in the testing apparatus under the microscope. Single fibers were selected one at a time for testing under the indenter. After a fiber was selected, the turntable was rotated under the indenter head, where a compressive force was applied to the fiber and held for five seconds. The indenter head was a ground diamond tip (6 μm radius for carbon fibers and 13 μm radius for glass fibers). The load was increased incrementally with a visual inspection of the fiber after each load step. The test was stopped and load recorded when the presence of debonding was observed, indicated by a black circle around the fiber. A test was discarded if loading did not occur in the center of the specimen. The resolution of the turntable was about 1 μm , and the load accuracy was about 0.1 g (\cong 0.1 mN).

The debond load was converted into interfacial shear strength through an axisymmetric finite element analysis. The conversion was based on model results where $T_m/D_f = 0.4$ (T_m is the matrix thickness to the nearest neighbor fiber and D_f is the fiber diameter). Results for other local volume fractions were shifted based on Equation 2-1 and converted to the debond load through Equation 2-2 [14].

$$\overline{s}_{0.4} = \overline{s} \left[0.4 / \left(\frac{T_m}{D_f} \right) \right]^{0.1} \quad 2-1$$

$$t_{DEB} = \overline{s}_{0.4} \left(\frac{t_{\max}}{\overline{s}_{0.4}} \right)_{FEA} \quad 2-2$$

The experimental results are reported in Table 2-1 and compared to another test for interfacial shear strength based on critical length. The large difference between the two conjures up questions on the validity of the microindentation test and its analysis. Sources of experimental error were mostly linked to limitations of the current apparatus and test procedure, including loading increments of 0.5g and the inability to measure the fiber diameters accurately [14].

Table 2-1. Experimental Results [14]

Material	Critical Length τ_{DEB}	Microindentation τ_{DEB}	Microindentation Coefficient of Variation
	<i>MPa</i>	<i>MPa</i>	<i>%</i>
Graphite/Epoxy	67	44	13.3
T300/5208 Graphite/Epoxy	-	88	7.6
S-Glass/Epoxy #1	-	69	10.5
S-Glass/Epoxy #2	-	68	5.4
E-Glass/Epoxy	-	57	-
E-Glass/Epoxy (single strand)	79	56	6.4
E-Glass/Polyester (single strand)	28	23	8.2

The authors Desaeger and Verpoest [15] accomplished microindentation using a nanoindenter, improving upon the test apparatus used by Mandell et al. [14]. The goal of their work was to analyze the microindentation technique and remark on applications, advantages and disadvantages, and the validity of the results. They believed the microindentation method to be superior to single fiber techniques on model composites because it utilizes a real composite that includes the role of neighboring fibers, thermal stresses, and polymer morphology issues such as cross-link density and spherulite dimensions. According to Desaeger and Verpoest [15] the realistic testing conditions of microindentation outweigh the trouble of calculating the stress-state around the fiber.

The materials tested in this work covered a wide range fiber and matrix combinations. Both carbon and glass fibers were employed and combined with thermoplastic and thermosetting matrices. The various properties and fiber/matrix

combinations are shown in Table 2-2. The samples were prepared by cutting a sample described as “thick” in the fiber direction and then performing a “perfect” polish on the sample. “Perfect” polishing was defined as causing no damage and creating very little additional stresses at the interface, and it was noted that this step is essential in obtaining a good evaluation of interface properties. Comparisons of results of specimens under two different polishing conditions show a 40% reduction in interfacial shear strength when great care is not taken. The tests were performed on a nanoindenter obtained from NANO-instruments, an instrument very similar to the microindentation instruments mentioned previously. The nanoindenter is outfitted with an optical microscope, where fibers are selected for indentation and recorded in the computer for testing. The force is applied through a pyramidal diamond tip to the positions selected by the user through the optical microscope. The accuracy of the load applied is $\pm 1 \mu\text{N}$ with a resolution in vertical displacement of $\pm 1 \text{ nm}$. The x-y table that carries the specimen from the microscope to the indenter has an accuracy of $\pm 2 \mu\text{m}$ depending upon temperature, humidity, and external vibration [15].

Table 2-2. Material Properties [15]

Material	1	2	3	4	5	6	7	8	9
C = Carbon G = Glass	C/Ep ^a	C/Ep ^a	C/Ep ^a	C/BMI ^b	C/BMI ^b	C/BMI ^b	G/TP- polyester	G/PA ^c	G/PA ^c
E _f (GPa)	234	234	230	317	317	197	70	77	77
D _f (mm)	7	7	7	6	6	9	8	10	10
E _m (GPa)	3.7	3.7	3.1	4.7	4.7	3.6	2.8	3.2	3.2
v _m	0.41	0.41	0.35	0.35	0.35	0.40	0.45	0.35	0.35
V _f (%)	60	60	58	62	62	55	50	30	30
IFSS (MPa)*	92		135	127	70	45			

*Reported by authors from additional literature

^aEpoxy

^bBismaleimide

^cPolyamide

A test procedure was outlined by Deseager and Verpoest [15] after trial and error. The specimen is placed in the machine one night before testing to obtain thermal equilibrium of the specimen. Several calibrations are done on the distance from the microscope to the indenter to make sure the fibers selected are indented accurately. Fibers are selected that have approximately the same diameter and neighboring fiber environment, an environment which best represents the global volume fraction. The

fibers are video recorded before indentation to compare to the post-indentation fibers. About 80 fibers per material were indented at different loads varying from 1 to 100 mN. The individual fiber experiments were considered valid if the indent occurred in the middle of the fiber. An example of the load-displacement curve is shown in Figure 2-1. Debonding was assumed when an interface crack, optically observed as a black rim around the fiber, of more than 25% of the fiber circumference was observed. There was a 30% experimental success rate, mostly due to a lack of positioning accuracy. Problems with fiber splitting also occurred, and only fibers where splitting did not occur were included in the results. Figure 2-2 shows the effect of fiber splitting on the load-displacement curve from the nanoindenter. A spherical indenter tip was successfully used in an attempt to reduce fiber splitting, but the different shape of the tip affected the results. Each fiber/matrix combination produced a range of debond load values, with the value for each combination being denoted as the load for which the probability of debonding was 50%. The calculation of the debond load optically was a necessity because no curvature was detected in the load-displacement curve, even when full debonding was observed optically. The authors also attempted to determine the presence of debonding by comparing the slopes of the loading and unloading curves in an effort to see a change in compliance that would be associated with the separation of fiber and matrix. This method failed to show that debonding had occurred. Hysteresis loops were also examined in load cycles on the fiber, but unlike in ceramic composites, no reliable correlation was seen to the debonding. It is assumed this is a result of non-perfect elasticity.

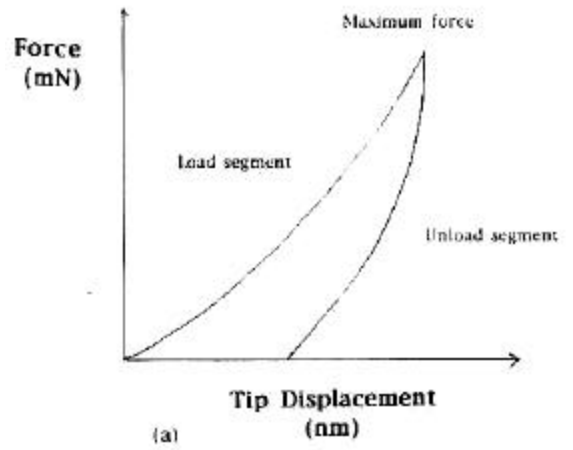


Figure 2-1. Load-Displacement Curve for Single Fiber using Nanoindenter (Reprinted with permission from Elsevier Science) [15]

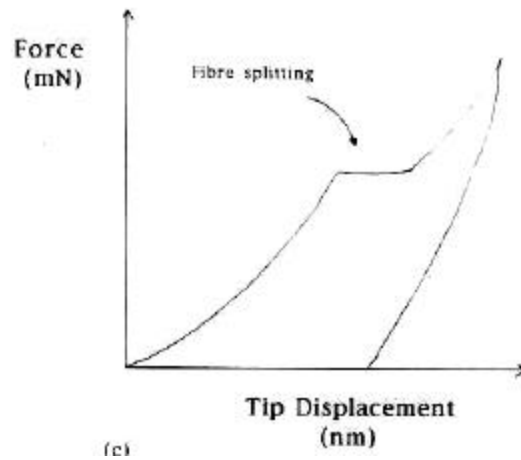


Figure 2-2. Load Displacement Curve showing Fiber Splitting (Reprinted with permission from Elsevier Science) [15]

The debonding was also observed using a scanning electron microscope. Some of the carbon/epoxy fiber interfaces tested showed gaps representative of debonding, while others showed no sign of the debond. It was hypothesized by the authors that part of the deformed matrix might cover part of the fiber and hide the interface crack. Overall, the optical evaluation of debonding, the only method that worked, was deemed difficult and highly subjective, but results were within 13% of previous results from other micromechanical experiments. It is believed that the various detection techniques provide a debond load based on different critical phenomena, and it is advised that any chosen technique be compared to that of another for confirmation [15].

The site of the optically located debonding was also of interest to the authors. They found that if the fiber is indented off-center the debonding is partial and on the side closest to the indenter. They also discovered that partial debonding most often occurred on the side of the fiber nearest the more matrix rich region. It was found that in a test of fibers in fiber and matrix rich regions that the fibers in the matrix rich region debonded more rapidly than those in the fiber rich region. This finding contradicts the finite element predictions of the authors, which state that a decrease in the matrix region between fibers leads to an increase in the maximum shear stress. It was suggested that this phenomenon might be related to the thermal stresses in the real composite or the effect of tip shape, which is not taken into account in the finite element modeling [15].

The conversion of the debond load to interfacial shear strength was computed using a shear lag analytical approach and compared with a simple finite element analysis. Equation 2-3 shows the result of the shear lag analysis that is used to determine IFSS.

$$t_{debond} = \frac{nF_{debond}}{2pr^2}$$

$$n = \frac{2E_m}{E_f(1+u_m) \ln\left(\frac{2p}{\sqrt{3}}V_f\right)}$$

2-3

F_{debond} = Measured Debond Load

r = Fiber Radius

E_f = Fiber Modulus

E_m = Matrix Modulus

u_m = Matrix Poisson's Ratio

V_f = Local Fiber Volume Fraction

The fiber radius of the tested fiber has a significant effect on this equation, and the authors recommend precise measurement of each fiber tested. A mistake of one micron on a seven micron fiber can cause a 30% change in the calculated value. IFSS results for

the various carbon and glass fiber systems are shown in Table 2-3. A finite element approach was utilized to confirm the results of the shear lag analysis. A simple model was developed including fiber, matrix, and bulk composite. The correlation between the finite element model and the shear lag analysis was good, but only if a flat tip is modeled to compress the entire fiber surface, as is the assumption used in the shear lag analysis [15].

Table 2-3. Nanoindentation Results

Material	1	2	3	3	4	5	6	7	8	9	9
C = Carbon G = Glass	C/Ep	C/Ep	C/Ep	C/Ep	C/BMI	C/BMI	C/BMI	G/TP- polyester	G/PA	G/PA	G/PA
			Fiber Zone	Matrix Zone						Badly Polished	Well Polished
F_{splitting} (mN)	50	45	40	30	40	40	45	50	-	-	-
F_{debond} (mN)											
Pyramidal Tip	52±5	38±5	59±8	57±2	71±10	65±5	56±5	20±8	45±8	28±2	
Round Tip										19±2	32±10
IFSS (MPa)											
Pyramidal Tip	102±10	75±9	85±11	82±3	109±15	103±7	117±10	59±24	45±8	31±3	
Round Tip										21±5	36±11

Desaeger and Verpoest [15] concluded that the method of microindentation was advantageous due to the *in situ* nature of the testing. They did however find disadvantages in the subjectivity of determining the debond load and the validity of the maximum shear strength calculated from the shear lag analysis. They do however state that while the absolute value of the interfacial shear strengths may not be valid, they can be used for comparisons of various fiber/matrix systems.

Drzal et al. [16] have produced many excellent results on interfacial adhesion using the microindentation method. Experimentally, an Interfacial Testing System (ITS), developed by the Dow Chemical Company, is used to examine the samples. The ITS system uses a diamond-tipped stylus to push on the single fibers. Composites samples are cut to about 1/4" x 1/4" x 1/8" and mounted in metallographic specimen holders with the fibers perpendicular to the surface. Polishing is accomplished utilizing conventional metallographic techniques. The polished specimen is placed upon the microscope stage, and fibers are selected individually from a television monitor with the coordinates recorded electronically. The stage is then moved under the indenter, where the test

occurs on a selected fiber at a pre-selected rate. Force-displacement data is obtained during the process and is sometimes used to determine the load at which debond occurs. Optical methods are also used to determine the debond load by basically using a microscope to determine the load at which debonding has occurred along twenty-five percent of the fiber perimeter. Once the debond load is discovered, an interfacial shear strength is calculated using Equation 2-4, an empirically based equation called the ITS equation that requires the matrix shear modulus, fiber modulus, distance between the tested fiber and the fiber closest to it, and the diameter of the tested fiber itself. [16]

$$\frac{t_i}{s_{fd}} = 0.8757 \left(\frac{G_m}{E_f} \right)^{0.5} - 0.1863 \times \ln \left(\frac{t_m}{d_f} \right) - 0.026496 \quad 2-4$$

The ITS equation was compared with two different shear lag models that are based on interphase properties rather than the formulation by Mandell et al. [14], which was based purely on fiber and matrix properties. The shear lag models are shown in Equations 2-5 and 2-6, where the "i" subscript represents an interfacial property. Equation 2-5 requires a measurement of the interphase thickness, t_i , and ignores the existence matrix deformation. The second shear lag model, Equation 2-6, takes into account the matrix deformation and requires measurements of r_f , r_i , and r_m , which are the fiber, interphase, and matrix radii in a cylindrical representative volume element [16].

$$t_i = \frac{P \left[\frac{4G_i}{t_i d_f E_f} \right]^{0.5}}{p d_f} \quad 2-5$$

$$t_i = 0.707s_{fd} \left(\frac{G_m}{E_f} \right)^{0.5} \frac{\tanh(al)}{\left[\frac{G_m}{G_i - 1} \ln \left(1 + \frac{2t_i}{d_f} \right) + \ln \left(1 + \frac{2t_m}{d_f} \right) \right]^{0.5}}$$

2-6

$$a = \left\{ 2G_i / E_f r_f^2 \ln \left(\frac{r_i}{r_f} \right) \right\} / \left\{ 1 + G_i \ln \left(\frac{r_m}{r_i} \right) / G_m \ln \left(\frac{r_m}{r_f} \right) \right\}$$

Finite element modeling was also conducted to evaluate the validity of the ITS equation and to perform parametric studies by varying the properties of the constituent materials and the sample geometry. The non-linear finite element model is depicted pictorially in Figure 2-3 and consists of an indenter, fiber, an interphase, matrix, bulk composite, and a foundation representative of the metallographic sample mount. The first discovery of the model was the conclusion that the effect of the sample foundation is eliminated at a critical value of thirty-six fiber diameters. It also showed that the effect of local volume fraction can cause a 35% change in interfacial shear strength by changing the fiber volume fraction from 10% to 50%. In comparison with the ITS equation and the two shear lag models, the finite element model agrees well with the ITS equation when the fiber volume fraction was between 30% and 50%, with the best agreement occurring at a volume fraction of 36%. The shear lag models did not agree well with the ITS equation or finite element model and was found to only be accurate at a volume fraction of 10% [16].

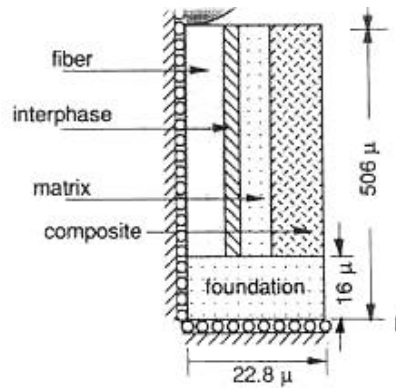


Figure 2-3. Finite Element Model Description (Reprinted with permission from Elsevier Science) [16]

It was concluded by the authors that the ITS equation was valid for volume fractions from 30% to 50% and that the debond load should be determined by optical evaluation of the fiber/matrix interface [16]. Relying on this method results were obtained on several fiber/matrix systems, including carbon fiber/vinyl ester matrix composites. Results from microindentation tests on composites composed of Panex33 carbon fibers coated with a 5 wt% epoxy-403 with a Derakane 411-C50 vinyl ester matrix show a 30% improvement in interfacial shear strength over an untreated fiber. The interfacial shear strength for the untreated fiber was 37.5 MPa while the epoxy treated fiber had a higher value at 48.4 MPa [17]. It was also concluded by the authors that the load-displacement curve could not be used to provide the location where debonding occurs.

The work by Chateauminois et al. [18, 19, 20] attempts to address some of the difficulties encountered by Drzal et al. [16,17], particularly the inability to detect fiber debonding from the load-displacement curve. Glass/epoxy composites were evaluated using a Vicker's indenter in this study. The goal of the work was to treat the load-deflection curve in order to reveal the debond load without the need for optical verification of debonding. The pursuit of interfacial shear strength by this group of authors is to measure the durability of the composite because it is their belief that long-term performance of a material is controlled by the extent of micromechanical damage at the interface. The microindentation test was chosen over the single-fiber tests because the effects from neighboring fibers, residual thermal stresses, and differences in polymer morphology lead to significant differences between "real" and model composites. As mentioned previously, the microindentation test has its own disadvantages, including the detection of debonding and evaluation of interfacial shear stresses in the complex, non-axisymmetric fiber environment, problems addressed by the authors [18].

The procedure for their microindentation tests begins with sample preparation. The unidirectional glass/epoxy composite samples were cut to 10 mm x 10 mm x 3 mm with a diamond saw. The specimens were polished with grinding papers and diamond

pastes of 6 to 1 μm on cotton cloths. The goal of the polishing techniques was to minimize the polishing stresses that could result in interfacial damage. The researchers observed no such damage with this polishing technique by using a scanning electron microscope to search for premature debonding, indicated by black circles around the fiber [18].

The prepared samples were mounted on an indenter outfitted with an optical microscope. The specimen is moved from the microscope to indenter on a moving table with a linear stepping motor of $\pm 0.1 \mu\text{m}$ resolution. An 80% success rate was achieved at hitting the fiber selected in the microscope for indentation. Fibers were selected that had nearly the same fiber diameter with a similar neighboring environment. Indentation speeds from 0.05 to 1 $\mu\text{m/s}$ were attempted, but no speed effect was discovered, and a rate of 0.2 $\mu\text{m/s}$ was selected for the test procedure. The normal load and penetration depth were continuously recorded during the indentation process. The indenter had a maximum displacement of 200 μm with a resolution of $\pm 0.05 \mu\text{m}$ and a maximum load of 600 mN with a resolution of $\pm 1 \text{ mN}$ [18].

The specimens were optically evaluated after testing, and full or partial debonding was detected depending upon the fiber environment. The load-displacement curve showed no change in curvature, even when full debonding was optically observed. An example of the load-displacement curve is shown in Figure 2-4. The load-displacement curve was then treated to produce a reduced indentation curve that shows a change in curvature at the point of debonding. The reduced indentation curve is created by extracting the two components of the load-displacement curve: (1) the elasto-plastic indentation of the fiber surface, and (2) the displacement due to fiber compression into the epoxy and the deflection of the matrix [18]. The theory is shown pictorially in Figure 2-5. The goal of extracting the fiber plastic deformation is to simulate loading the fiber with a flat punch, a loading geometry more easily modeled analytically.

The plastic deformation of the glass fiber is determined by indenting a piece of bulk E-glass material (for glass fiber composites). The elasto-plastic indentation loading

in glass follows the empirical relationship in Equation 2-7, where K and m are constants related to the indenter geometry and behavior, and u_{ep} and P are the displacement and load respectively.

$$u_{ep} = KP^m \quad 2-7$$

The unloading portion of the curve is fitted by the empirical relationship in Equation 2-8.

$$u_{ep} = a + bP + gP^2 \quad 2-8$$

K , m , a , b , and g are obtained by fitting the Equations 2-7 and 2-8 to the experimental E-glass indentation curve. The resulting curve is subtracted from the fiber/matrix microindentation curve, shown in Figure 2-4, to give the displacement of the fiber surface.

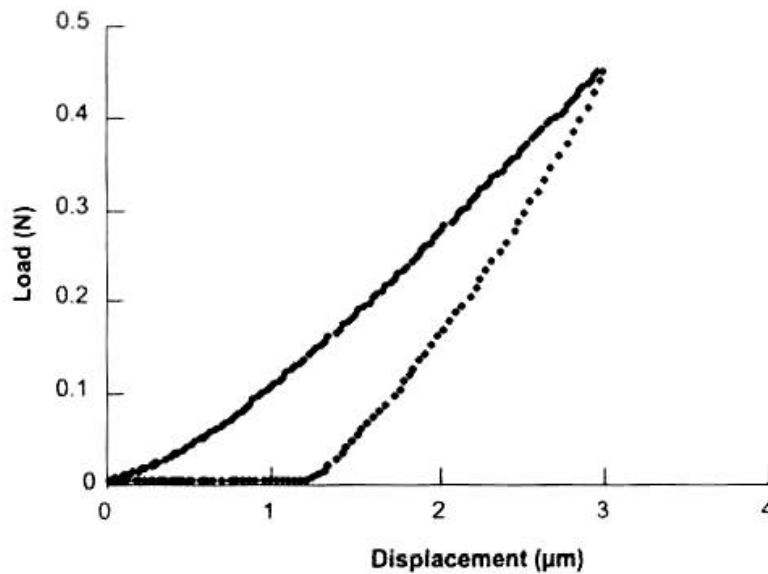


Figure 2-4. Load-Displacement from a Single Fiber using Microindentation (Reprinted with permission from Elsevier Science) [18]

The curve created is called the reduced indentation curve. The physical interpretation of this analysis is shown in Figure 2-4 as illustrated by the authors. The resulting curve, represented by (b) in Figure 2-5, is shown in Figure 2-1.

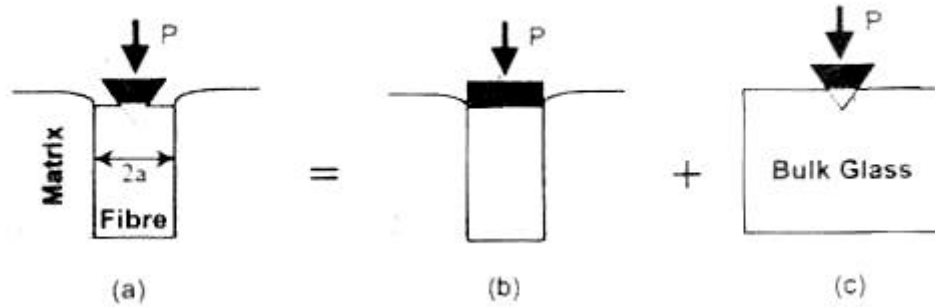


Figure 2-5. Illustration of Displacement Components in Microindentation (Reprinted with permission from Elsevier Science) [19]

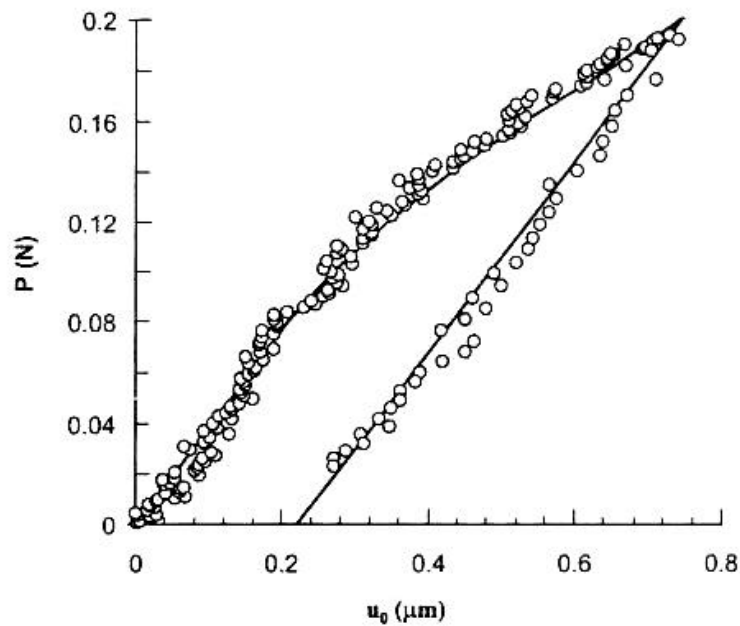


Figure 2-6. Reduced Indentation Curve, Experimental and Fit (Reprinted with permission from Elsevier Science) [19]

The characteristic curvature of the reduced indentation curve in Figure 2-6 is believed to be a result of fiber debonding or matrix/interphase yielding. The authors have uniquely extracted the debond load by fitting lines to the loading and unloading of these reduced indentation curves [19]. The curve is fitted and the interfacial shear strength is

determined by a simple shear lag analysis. The analysis is derived from a force balance on the fiber, Hooke's Law, and applied boundary conditions. The boundary conditions are shown in Equations 2-9 and 2-10, where s_0 is the stress applied to a fiber of radius a with an indenter load P and $s(\infty)$ is the far-field normal stress in the fiber.

$$s_0 = \frac{P}{\pi a^2} \quad 2-9$$

$$s(\infty) = 0 \quad 2-10$$

The differential equations are assembled by the result of the force balance, Equation 2-11, and a form of Hooke's Law, Equation 2-12.

$$\frac{ds}{dx} = -\frac{2t}{a} \quad 2-11$$

$$\frac{du}{dx} = -\frac{s}{E_f} \quad 2-12$$

The shear stress τ is related to the matrix deflection and a global stiffness constant, k , in Equation 2-13. The global stiffness constant takes into account the properties and environment surrounding the tested fiber. The value can be expressed analytically in terms of the matrix shear modulus, G_m , the fiber radius, and the average distance to the nearest fiber, R_{eq} , by Equation 2-14.

$$t = kw \quad 2-13$$

$$k = \frac{G_m}{a \log\left(\frac{R_{eq}}{a}\right)} \quad 2-14$$

The initial portion of the reduced indentation curve is defined as elastic deformation without debonding, which means that the matrix displacement is equal to the fiber displacement, $w = u$, at the interface. By combining Equations 2-11, 2-12, and 2-13, a second order differential equation, Equation 2-15, is formed and solved by the boundary conditions in Equations 2-9 and 2-10 for the initial indentation loading to arrive at Equations 2-16, 2-17, and 2-18 for displacement, normal fiber stress, and interfacial shear stress respectively.

$$\frac{d^2u}{dx^2} - n^2u = 0 \tag{2-15}$$

$$n = \sqrt{\frac{2k}{aE_f}}$$

$$u(x) = \frac{\mathbf{S}_0}{nE_f} e^{-nx} \tag{2-16}$$

$$\mathbf{s}(x) = \mathbf{s}_0 e^{-nx} \tag{2-17}$$

$$\mathbf{t}(x) = \frac{an\mathbf{S}_0}{2} e^{-nx} \tag{2-18}$$

Debonding occurs when the interfacial shear stress at $x = 0$ becomes equal to the interfacial shear strength, \mathbf{t}_d , which can be correlated to the normal stress at debonding by Equation 2-19. It is assumed that the debond occurs at a distance h below the surface and rapidly propagates to the free surface. This accounts for the fact that in reality the interfacial shear stress has a maximum away from the free surface and is equal to zero at the free surface. The shear lag analysis does not satisfy this boundary condition. It is assumed that $\mathbf{t} = \mathbf{t}_d$ in the debonded region in an attempt to estimate the frictional shear force.

$$\mathbf{s}_d = \frac{2\mathbf{t}_d}{an} \quad \mathbf{2-19}$$

With a constant normal fiber stress in the debonded region, a new second order differential equation is formed, Equation 2-20, with two new boundary conditions, Equations 2-21 and 2-22.

$$\frac{d^2u}{dx^2} - \frac{2\mathbf{t}_d}{aE_f} = 0 \quad 0 \leq x \leq h \quad \mathbf{2-20}$$

$$u(h) = \frac{\mathbf{t}_d}{k} \quad \mathbf{2-21}$$

$$E \frac{du}{dx}(h) = -\frac{2\mathbf{t}_d}{an} \quad \mathbf{2-22}$$

By solving the differential equation, the fiber displacement is determined in the debonded region. The original differential equation for a bonded system is again utilized to solve for the displacement outside the debonded region. The fiber displacements in the bonded and debonded areas are represented by Equations 2-23 and 2-24.

$$u(x) = \frac{\mathbf{t}_d}{aE_f} x^2 - \frac{\mathbf{s}_0}{E_f} x + \frac{a\mathbf{s}_0^2}{4\mathbf{t}_d E_f} + \frac{\mathbf{t}_d}{aE_f n^2} \quad 0 \leq x \leq h \quad \mathbf{2-23}$$

$$u(x) = \frac{\mathbf{t}_d}{k} e^{-n(x-h)} \quad x > h \quad \mathbf{2-24}$$

The unloading condition on the reduced indentation curve is based on a purely elastic recovery until the stress reaches a critical stress, called \mathbf{s}_s . This critical stress level is when sliding is initiated. The derivation for the unloading condition is shown in detail in Zidi et al. [19].

The shear lag analysis derived above for the loading and unloading case is applied to the reduced indentation curve by Equations 2-25, 2-26, 2-27, and 2-28. These equations represent the displacement of the fiber surface in terms of the applied surface normal stress, material properties, empirical parameters, the debond stress, and the sliding stress. Equation 2-25 is used to identify an empirically determined n value by fitting the initial linear region of the loading portion of the indentation curve. The debond load is then determined through a least squares fit of the entire loading curve. The unloading portion is fitted by the remaining two equations. The resulting curve fit is shown in Figure 2-6 on top of an experimental reduced indentation curve. The interfacial shear strength is then determined by rearranging Equation 2-19.

$$u_0 = \frac{\mathbf{s}_0}{nE_f} \quad \mathbf{s}_0 \leq \mathbf{s}_d \quad \mathbf{2-25}$$

$$u_0 = \frac{1}{2nE_f} \left(\frac{\mathbf{s}_0^2}{\mathbf{s}_d} + \mathbf{s}_d \right) \quad \mathbf{s}_0 > \mathbf{s}_d \quad \mathbf{2-26}$$

$$u_0 = \frac{1}{2nE_f} \left(\frac{\mathbf{s}_{\max}^2}{\mathbf{s}_d} + \mathbf{s}_d + 2(\mathbf{s}_0 - \mathbf{s}_{\max}) \right) \quad \mathbf{s}_s \leq \mathbf{s}_0 \leq \mathbf{s}_{\max} \quad \mathbf{2-27}$$

$$u_0 = \frac{1}{2nE_f} \left(\frac{\mathbf{s}_{\max}^2}{\mathbf{s}_d} - \mathbf{s}_d - \frac{(\mathbf{s}_0 - \mathbf{s}_{\max})^2}{2\mathbf{s}_d} \right) \quad \mathbf{s}_0 \leq \mathbf{s}_s \quad \mathbf{2-28}$$

Using this analysis technique, the results from indentations on thirty glass/epoxy fibers were evaluated successfully. The results, shown in Table 2-4, show a lower standard deviation than previously seen in microindentation. The authors believe that the improvement of results is due to taking into account an experimental value for n , the factor that accounts for the properties surrounding the fiber. The experimental values for n are validated by calculating R_{eq} , the distance to neighboring fibers, based on known matrix properties. The resulting values of R_{eq} closely match the distances to the nearest fiber in the experiments. It is also believed by the authors that the analysis is an

improvement of over previous work because the debond load is determined by fitting the entire indentation curve, therefore eliminating some of the subjectivity of determining when debonding actually begins [19].

Table 2-4. Microindentation Results using Shear Lag Analysis Method [19]

	Mean	Standard Deviation
Fiber Diameter, a (μm)	24.1	1.4
n (mm^{-1})	16.15	1.11
R_{eq} (μm)	26.01	5.57
t_d (MPa)	73	5

In later work, Zidi et al. [20] discovered that the curve fitting procedure that worked very well on some composites did not work as well for others, particularly a glass/polyester system. In order to improve their analysis to account for this problem, they improved upon the assumptions in their original work. The basic model assumed a constant shear stress in the debonded region equal to the interfacial shear strength. It was considered more realistic to consider a transition from the bonded to sliding state with a change in interfacial shear stress. The debond stress was multiplied by a factor α to create a new term t_g , where α is less than one. t_g replaces t_d in Equation 2-20, which was solved in the same manner as before. The solution was fitted simultaneously by the debond load and α to the experimental loading data by an iterative least-squares fitting technique. The resulting fit is shown in Figure 2-1.

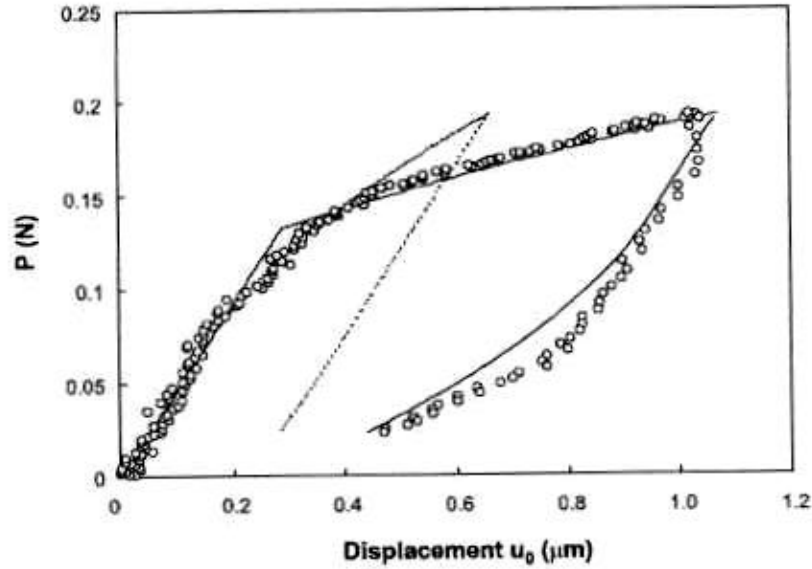


Figure 2-7. Reduced Indentation Curve with Weak Interface (Reprinted with permission from Elsevier Science) [20]

Although this modeled fitted the experimental data well, it created a kink in the loading curve that is considered physically impossible. Therefore, a progressive interfacial debonding mechanism was sought. A generalized interface law was created, related to the fiber displacement as shown in Equation 2-29, where u_h is the fiber displacement at the end of the debonded area ($x = h$) and b is a parameter used to describe the interfacial response by varying it between 0 and ∞ . Equation 2-30 is the new differential equation that must be solved to fit the post-debonding loading curve with the boundary conditions displayed in Equations 2-31 and 2-32. The resulting curve fit is shown with experimental data in Figure 2-8. It was concluded that the flexibility of these new interface laws allow a researcher to determine the fiber debond loads for various fiber/matrix systems that have various modes of interfacial failure, from perfectly plastic to brittle.

$$t = t_d \left(\frac{u_h}{u} \right)^b \quad 2-29$$

$$\frac{d^2u}{dy^2} - \frac{2t_d}{aE_f} \left(\frac{u_h}{u} \right)^b = 0 \quad 2-30$$

where $y = x - h$

$$\frac{du}{dy}(0) = \frac{2t_d}{anE_f} \quad 2-31$$

$$u(0) = \frac{2t_d}{aE_f n^2} \quad 2-32$$

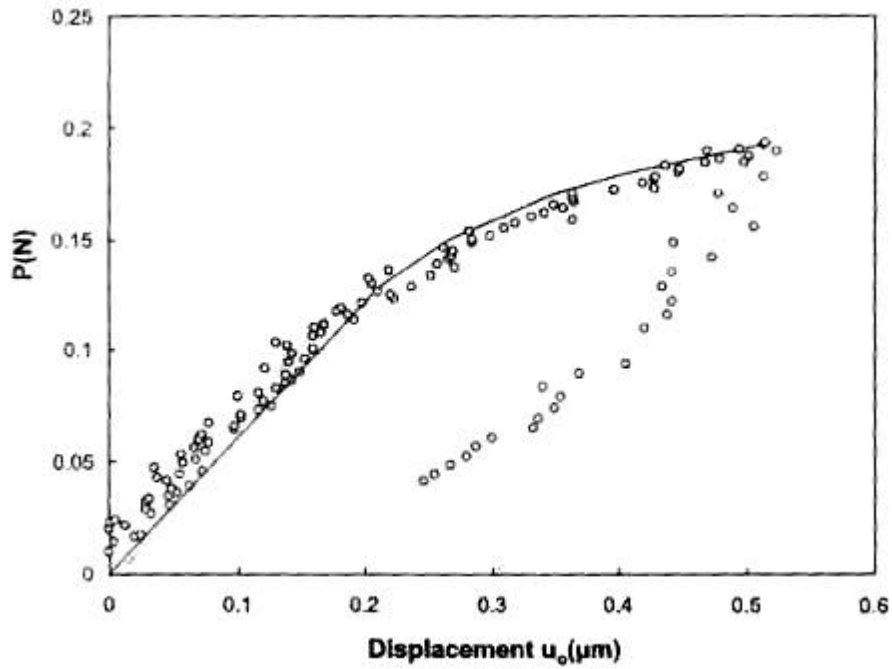


Figure 2-8. Reduced Indentation Curve with Progressive Debonding (Reprinted with permission from Elsevier Science) [20]

2.4 Tensile Strength Modeling

The modeling of the tensile strength including interfacial properties was attempted in the model created by Gao and Reifsnider [21,22] for use with polymer matrix composites. The prediction utilizes the probability analysis of Batdorf [23] and assumes damage due to loading consists solely of breaks in the fibers. The breaks of fibers occur in single isolated fibers, pairs of fiber breaks, and in general i adjacent fiber breaks. The breaks in the fiber cause a stress concentration that acts over the ineffective length of the fiber, which is assumed to follow a two-parameter Weibull distribution. It is in this ineffective length that shear stresses develop at the fiber/matrix interface that transfers the additional load in the matrix at the fiber break back into the fiber. The statistics presented by Batdorf [23] determines the distribution of adjacent fiber breaks. If the shear strength or yield strength of this interface is overcome in this region, fiber debonding or matrix/interphase yielding occurs. The stress concentrations and ineffective lengths for each number of adjacent fractures was determined by Gao and Reifsnider [21] using a shear lag model. In this model, the region of broken composite is surrounded by concentric cylinders of matrix, fiber, additional matrix, and bulk composite. The crack in the broken composite spans from matrix zone to matrix zone resulting in a region of yielded matrix. The length of the yielded (or debonded) zone affects the ineffective length, which is defined as the distance required for the stress on adjacent fibers to return to 5% of its far-field value. Results from this model for normalized strength versus interface/matrix yielding are shown in Figure 2-9. It is interesting to note that the yield or debond stress at the interface can be too large and result in decreased strength values.

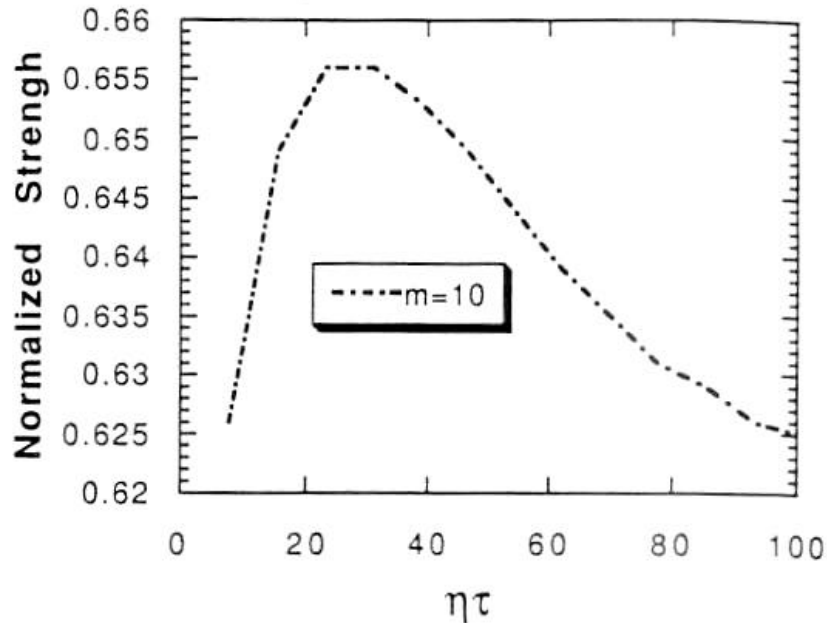


Figure 2-9. Predicted Normalized Strength versus Interface/Matrix Yield Stress (Reprinted with permission from the Journal of Composites, Technology & Research, Vol. 14, No. 4. Copyright ASTM) [21]

A model by Subramanian, Reifsnider, and Stinchcomb [24] modified the earlier ideas of Gao and Reifsnider [21]. The new model stressed the ideas of using interfacial shear strength and interfacial efficiency. Again, the model computed the stress concentrations and ineffective lengths based on the shear lag approach. The ineffective lengths utilized Batdorf's statistical tensile strength model [23].

2.5 Summary

The work of previous authors in the field of microindentation show that there is a need for further study. A standard test methodology and evaluation procedure have not been outlined for this useful test for interfacial shear strength. By combining the information presented here, a technique for microindentation can be utilized to evaluate the effect of fiber sizings, investigate enviro-mechanical damage to the interface, and relate interfacial changes to bulk composite properties, particularly tensile strength.

Chapter 3 Objectives

3.1 Project Objectives

The objectives of this work are as follows:

- **Evaluate the microindentation technique and improve upon the many disadvantages and shortcomings of the technique as outlined in previous works:** The goal is to provide a technique that is simple to use, expedient, and outputs useful interfacial shear strength numbers. Valid results will allow for inclusion in micromechanical modeling rather than just comparisons to other materials based on interfacial shear strength alone. The focus of improvements will be on creating a simple method for detecting interfacial debonding, creating a less complex loading situation on the fiber surface, and improving the experimental success rate. A sophisticated, highly accurate nanoindenter outfitted with a new blunt indenter tip will be used in the attempt to make these improvements and develop the desired microindentation technique.
- **Study the interfacial stresses present during the microindentation test and comment on the validity of various existing models used to calculate the maximum interfacial shear stress at the fiber/matrix debond load:** Shear lag and finite element approaches have dominated the analysis of this problem. The simplicity of the shear lag model makes it very advantageous for determining the interfacial shear strength and even the debond load as shown by Zidi et al. [19]. Attempts will be made to improve the validity of the shear lag model by inclusion of Poisson effects and radial forces from thermal/moisture contraction or expansion. An axisymmetric finite element model will be created for comparison with the shear lag model and to evaluate the effects of moisture expansion on the stress-state at the fiber/matrix interface.
- **Determine the interfacial shear strengths of the PHE, PVP, and G' sized materials and compare them to each other and their respective tensile strengths:** Results will be compared to those obtained from the single-fiber microbond test for the same materials.

Tensile strength predictions based on these interfacial shear strengths will be obtained utilizing the model by Gao and Reifsnider [21].

- **Examine the effects of hygrothermal aging on interfacial shear strength:** PHE, PVP, and G' composites will be hygrothermally aged at various lengths of time and evaluated for changes in interfacial shear strength. Residual tensile strength tests will be conducted on samples aged for an equivalent time period to see if a relationship exists between the two properties. Samples will be tested wet and dry (water removed after aging) to evaluate the effects of moisture in the sample on interfacial shear strength, tensile strength, and the microindentation technique itself. The tensile strength model will be employed for tensile strength predictions to compare to the residual strength results.
- **Examine the effects of mechanical fatigue on interfacial shear strength:** A preliminary investigation will be conducted on the effect of fatigue cycles on interfacial shear strength and its relationship to residual tensile strength.

Chapter 4 Materials and Experimental Procedure

4.1 Materials

The materials examined in this study are pultruded, unidirectional, fiber-reinforced polymer composites. The composites are comprised of Hexcel AS-4 carbon fibers sized with three fiber sizings and impregnated with a Dow Derakane™ vinyl ester matrix. The matrix resin is a modified Derakane™ 411-35 LI, which is a pultrudable resin, and contains approximately 42 wt% vinyl ester, 42 wt% styrene monomer, 15 wt% fillers such as clay, 0.5 wt% release agents, and 0.5 wt% of a proprietary initiator package. The matrix resin for the three types of composites came from a single batch.

Hexcel AS-4 12 K unsized carbon fiber was sized with two thermoplastics, a carboxyl modified poly(hydroxyether) of bisphenol A (PHE) and poly(vinylpyrrolidone) (PVP), at Virginia Tech. Samples were also tested that included Hexcel AS-4D G' sized 36K fiber, which is a fiber sized with a Hexcel commercial sizing for vinyl ester matrices. The AS-4 and AS-4D fibers do vary slightly in properties due to the higher draw ratio and improved crystal orientation in the AS-4D fibers. This results in a 4% higher modulus and a 10% increase in strength for the AS-4D fiber, but these results are accounted for in the comparisons

The poly(hydroxyether) is a material called Phenoxy™ that was obtained from Phenoxy Associates in Rock Hill, SC. The poly(hydroxyether) was carboxyl modified to enable its dispersion in water [6]. The PHE was applied in particle form from a liquid dispersion. The poly(vinylpyrrolidone) sizing material was obtained from BASF as K-90 PVP.

The materials were pultruded at the Strongwell Corporation in Bristol, VA on a pilot scale pultruder. The final pultruded composites had a cross-section of 12.7 mm x 2.0 mm. The Composite properties from characterization work [25] are reported in Table 4-1.

Table 4-1. Basic Properties for the Pultruded Composites and Components

Property	G'	PHE/LSP	PVP
Fiber Volume Fraction	60.8 %	57.7%	55.8%
Tensile Strength [25]	1673 ± 39 MPa	2035 ± 35 MPa	1964 ± 71 MPa
Tensile Modulus [25]	120.3 GPa	132.2 GPa	121.7 GPa
Fiber Diameter [26]	6.7 μm	7.1 μm	7.1 μm
Fiber Modulus [26]	241 GPa	228 GPa	228 GPa
Fiber Strength [26]	4550 MPa	4150 MPa	4150 MPa
Matrix Modulus* [27]	3.4 GPa	3.4 GPa	3.4 GPa
Matrix Strength* [27]	76 MPa	76 MPa	76 MPa
Sizing Strength	-	55 MPa	62 MPa
Sizing Strain-to-Failure	-	40-100%	0.9%

*Based on pure resin as produced by Dow Chemical Company

4.2 Experimental

4.2.1 Hygrothermal Aging

Samples of the pultruded unidirectional carbon composites were exposed to moisture in a water bath. The composites aged had G', PVP, and PHE fiber sizings. The samples were cut to 15.24 mm in length and had a constant cross section of 12.7 mm wide by 2.0 mm thick. This length is ideal for tensile testing of these composites and helps eliminate the effects of end diffusion on the saturation behavior of the composite. Aging was conducted in 65°C tap water in a self-contained Nalgene container. The 65°C temperature accelerates the moisture adsorption into the material. Weight measurements were made on a Mettler Toledo Balance to track the uptake of moisture in the sample. Samples were removed at various levels of moisture and also at different saturation times. The first moisture study involved all three composites and required removal at 24, 96, and 240 hours. Samples were removed for testing with nanoindentation and were kept wet. The second moisture study involved the PVP and PHE composites and required removal at 288 and 576 hours. Twelve samples were removed for each composite at both removal times: five samples for wet tensile testing, five for dry tensile testing, one for wet nanoindentation, and one for dry nanoindentation. The "dry" samples were dried in a vacuum oven at 60-65 °C for 29 hours at 30 mm Hg.

4.2.2 Mechanical Fatigue

Mechanical fatigue testing was completed on the composites containing G' and PHE sizings. The testing was completed on an MTS servo-hydraulic test frame utilizing an MTS 407 controller. Samples were cut to 15.24 mm in length with 3.81 mm end tabs adhered to specimen ends to prevent grip failures during the fatigue testing. The end tabs are a high pressure laminated glass-epoxy composite adhered with a two-part epoxy (3M's DP40) and cured overnight. The specimens were tested in tensile-tensile fatigue ($R = 0.1$) to 75% life at 50% of their respective ultimate tensile strengths. This was 4,536 cycles at a maximum load of 20.5 kN and 85,061 cycles at a maximum load of 24.6 kN for the G' and PHE composites respectively. Three samples were tested for each

material, two for residual strength and one for nanoindentation. Residual strengths were obtained on the same MTS servo-hydraulic test frame by following the tensile test procedure.

4.2.3 Tensile Testing

The tensile testing was completed on the same MTS servo-hydraulic machine used for mechanical fatigue testing. Samples were prepared by adhering high pressure laminated glass-epoxy composite tabs to the sample ends in order to produce an even load distribution and prevent grip failures. The end tabs were adhered to a sanded or grit-blasted composite surface and bonded with M-Bond 200 strain gage adhesive. The specimens were gripped at a grip pressure of 800 psi and were loaded at a ramp rate of 100 lbs/sec until failure [28].

4.2.4 Specimen Polishing and Preparation

In order to accurately apply the microindentation technique, the surface of the specimen must be polished in such a way to create a very flat surface, meaning very little relief between the fiber and matrix. The samples were cut to about one-half to three-quarters of an inch in length and placed in standard 1.25" diameter metallographic mounts. Careful attention was paid to the alignment of the sample so that the longitudinal, or fiber, direction was perpendicular to the surface to be polished. The specimens were mounted in a two-part epoxy supplied by Buehler and cured overnight. In an effort to obtain the best possible polish of the surface, the epoxy was mixed extensively until homogeneous and with little creation of air bubbles.

Polishing was completed on a Buehler[®] Ecomet[®] 3 polisher with a Automet[®] 2 automatic head. The procedure, suggested by Buehler[®] for polymer composites [29] and shown in Table 4-2, involves a series of silicon carbide sandpaper from 320 to 800 grit and a special polishing pad requiring diamond pastes and suspensions. Excess epoxy is removed prior to polishing with a lower grit sandpaper to make sure the sample is exposed on the surface. CARBIMENT[®], TEXMET[®], METADI[®], and MASTERPREP[™]

are brand names for products sold by Buehler[®]. CARBIMET[®] is a silicon carbide sandpaper, TEXMET[®] 1000 is an adhesively backed polishing pad, METADI[®] Paste is a diamond paste, and MASTERPREP[™] is a 0.05 μm alumina suspension. The relative rotations mentioned in Table 4-2 are with respect to the rotation of the automatic head versus the polisher. "Contra" represents opposite rotations, and "Comp" represents concurrent rotations. Polishing quality was maintained by using each piece of sandpaper or each polishing pad only one time. Completed polished samples were cleaned with an Aquasonic ultrasonic cleaner.

Table 4-2. Buehler[®] Polishing Procedure [29]

Surface	Lubricant Extender	Abrasive Type/Size	Time (min:sec)	Force per Specimen	Speed (RPM)	Relative Rotation
CARBIMET [®]	Water	SiC 320 grit	00:30	5 lbs.	250	Contra
CARBIMET [®]	Water	SiC 400 grit	00:30	5 lbs.	250	Contra
CARBIMET [®]	Water	SiC 600 grit	00:30	5 lbs.	250	Contra
CARBIMET [®]	Water	SiC 800 grit	00:30	5 lbs.	250	Contra
TEXMET [®] 1000	METADI [™] Fluid	METADI [™] Paste - 3 μm	04:00	6 lbs.	120	Comp
TEXMET [®] 1000	METADI [™] Fluid	MASTER- PREP [™]	03:00	10 lbs.	120	Comp

4.2.5 Nanoindentation

The indentation experiments were completed on the NANO II indenter located at the Oak Ridge National Laboratory in Oak Ridge, TN. The NANO II indenter was manufactured by MTS Nano Instruments and is shown in Figure 4-1. A schematic of the indenter is shown in Figure 4-2. The indenter operates in load-control with the load applied by the electro-magnetic coil shown in Figure 4-2 with a resolution of $\pm 75\text{nN}$. Displacements are measured to $\pm 0.04\text{ nm}$ with non-contact capacitance transducers that are placed near the center of the loading column. When enabled, continuous stiffness measurements are made using a lock-in amplifier that records the ratio of the displacement and force voltage signals and their phase difference [30]. The indenter tip, shown above the sample in the schematic, can be changed based on experimental needs. The most common tip type for the nanoindenter is the Berkovich, a three-sided pyramidal

diamond tip, but spherical and blunt tips are available. In this experimental procedure, a blunt four micron diameter conical diamond tip is utilized to push on the fibers in the composite. An impression of this tip, manufactured by Synton, Inc. in Switzerland, is shown in Figure 4-3. The impression was made in epoxy and imaged with a scanning electron microscope (SEM). The x-y-z table where the sample is secured has a resolution of ± 0.2 microns and is positioned optically. It is important to have high resolution on the x-y-z table because positioning of the fiber under the indenter tip is crucial to the success of the microindentation technique. The chosen fibers are selected under a microscope, recorded by the computer, and positioned under the indenter for loading. Multiple fibers may be selected for indenting during any experimental run, but error in positioning builds up over time making it difficult to hit the intended fiber target.

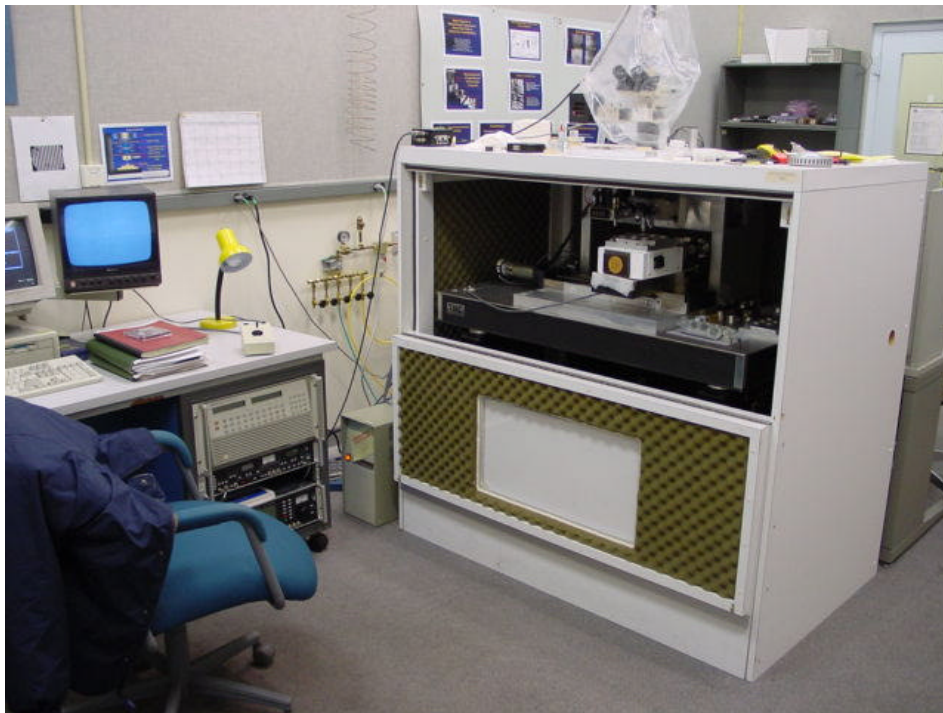


Figure 4-1. Photograph of NANO II Indenter at ORNL

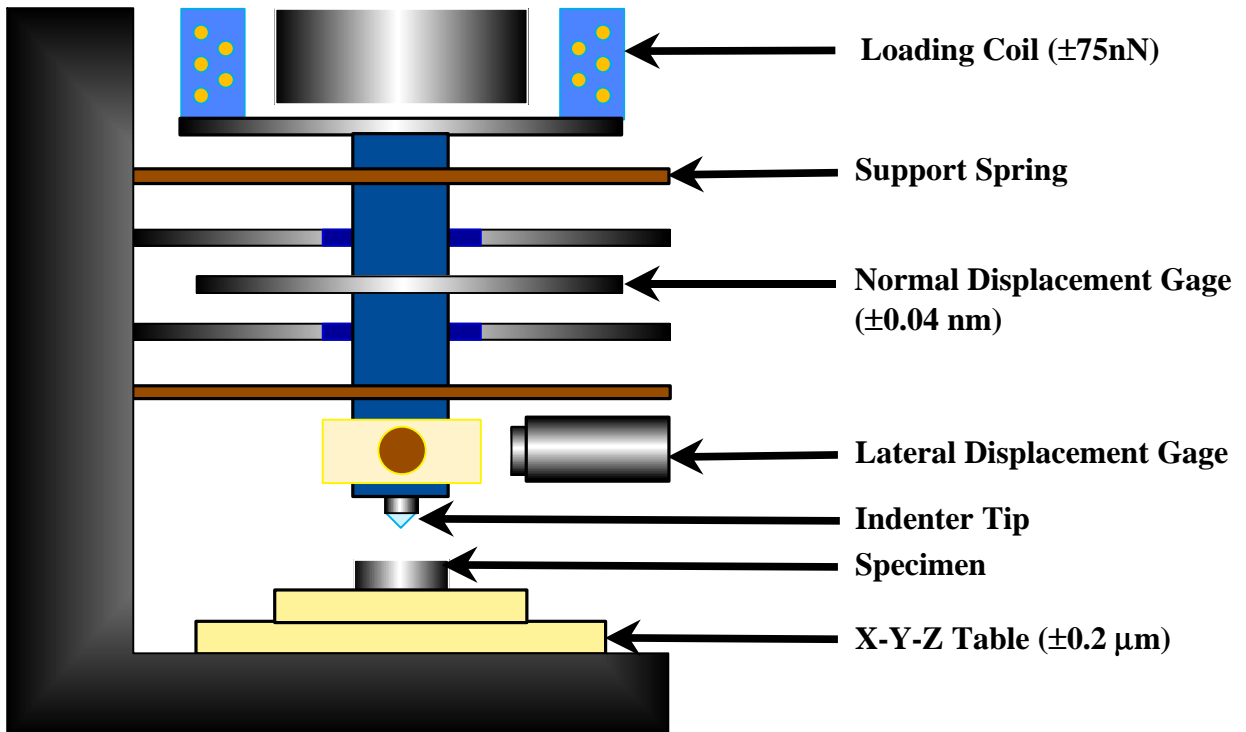


Figure 4-2. Schematic of the NANO II Indenter

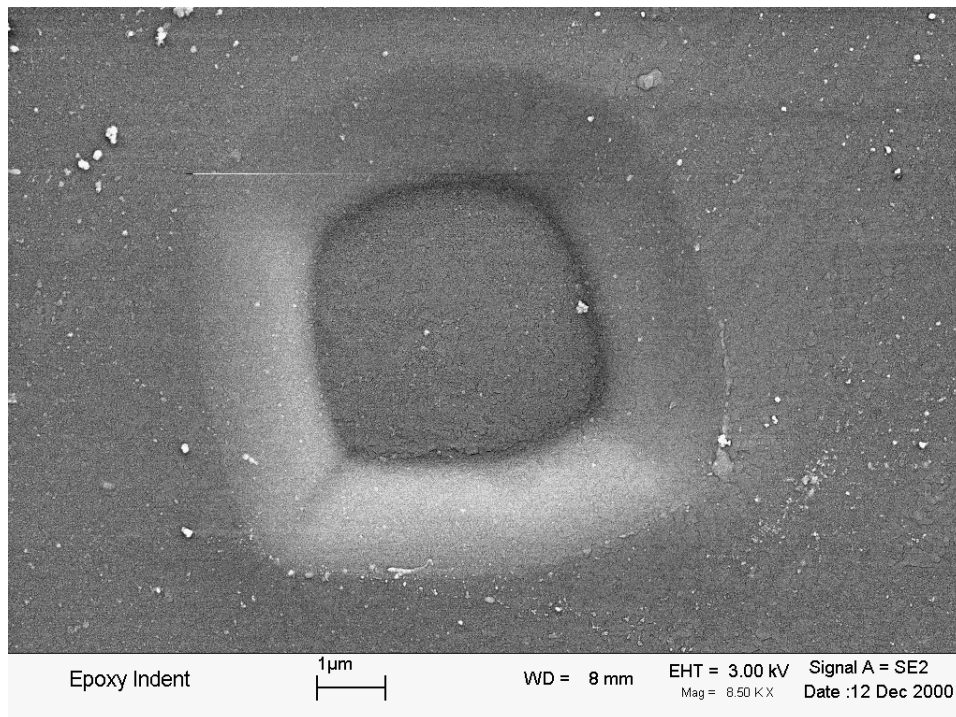


Figure 4-3. SEM Image of Tip Indent in Epoxy Substrate

Temperature in the laboratory is maintained at $74.0 \pm 0.2^{\circ}\text{F}$ and all samples are equilibrated to that temperature overnight in the indenter chamber to prevent thermal drift during the sensitive nanoindentation procedure. Specimens are mounted in holders specifically designed for 1.25" metallographic mounts, and several samples can be mounted at one time on the x-y-z table for evaluation. The procedure for testing the specimens involves a significant amount of computer and data acquisition setup. The first step is to determine the control system for the experiment. Two standard methods were used, simple load control and load control with the continuous stiffness option. For the continuous stiffness option, the indenter is set to apply a 2 nm peak-to-peak oscillation at a frequency of 45 Hz. In order to maintain the 2 nm oscillation, the load amplitude is adjusted within a control loop as the overall load-displacement procedure is carried out. Both control options were used for these experiments.

The fibers were selected optically, with a maximum of fifteen fibers at one time. Fibers were selected that appeared to be in good condition, had no previous debonding, and were not touching surrounding fibers. Attempts were made to choose fibers that were hexagonally packed with surrounding fibers, and from the same general region in each composite. Because of the hygrothermal aging, indents were made about 300 nm from the surface in the area depicted in Figure 4-4 and Figure 4-5. The loading procedure was then chosen for the entire set of fibers (although multiple procedures can be run during one test). The procedure developed loads the fiber at $0.5 \mu\text{N/s}/\mu\text{N}$ to a maximum load of 70 mN. A 70 mN load was sufficiently large enough to cause fiber debonding from the matrix for the fiber/matrix system under evaluation. The load was then held at the maximum load, and then unloaded at the current rate to 90% the maximum load. The load on the fiber is held again to calculate the thermal drift rate before completely unloading the fiber.



Figure 4-4. Polished Specimen for Nanoindentation



Figure 4-5. Indentation Region shown in Microscope Image

A typical result obtained from this procedure is shown in Figure 4-6 and Figure 4-7. The results are for the loading of a G' sized fiber with the presence of debonding indicated by the curvature of the load-displacement curve in Figure 4-6. Figure 4-7 shows the change in stiffness on this fiber during the loading cycle through the use of the continuous stiffness option on the nanoindenter. The same change in slope, representing fiber debonding, can be seen in the stiffness-load curve.

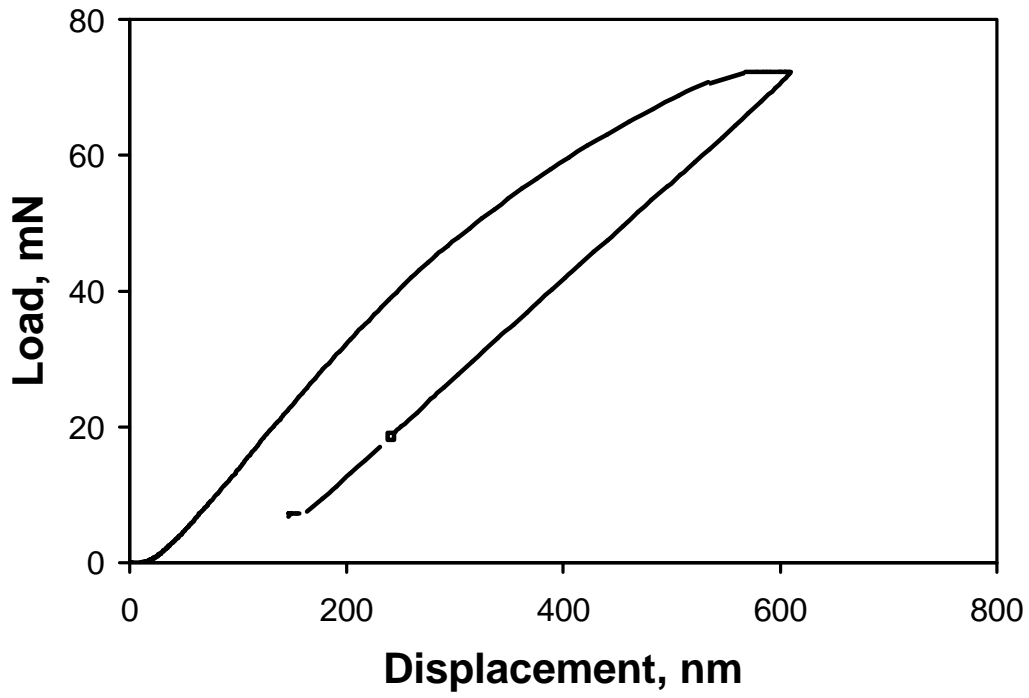


Figure 4-6. G' Single Fiber Load-Deflection Curve

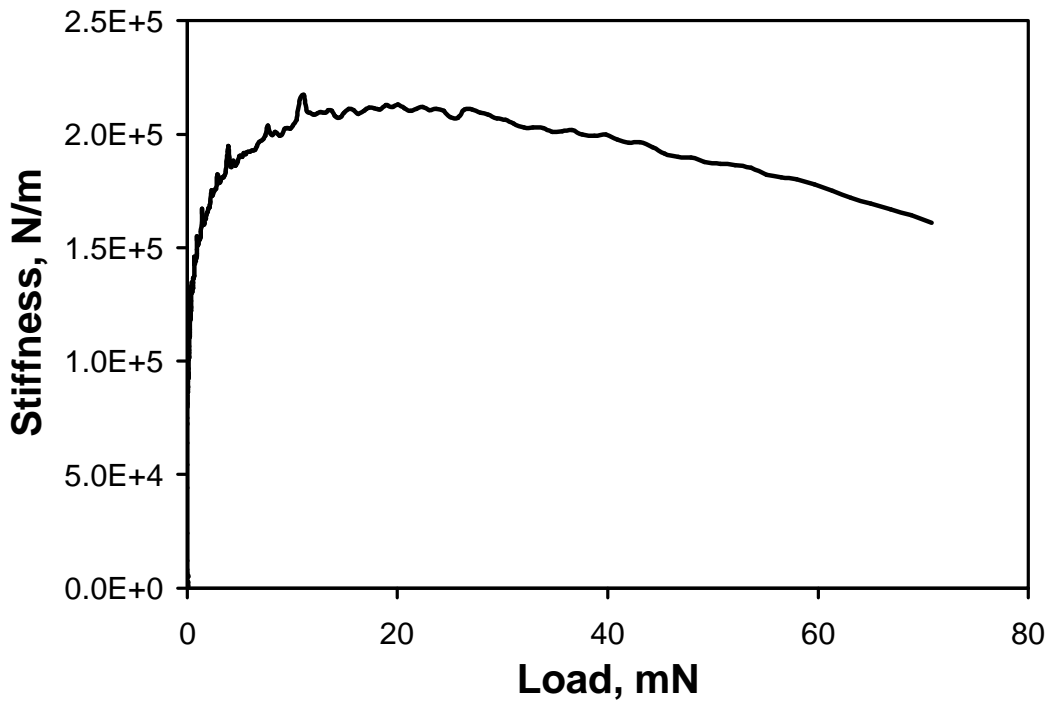


Figure 4-7. G' Single Fiber Stiffness-Load Curve from Continuous Stiffness Measurement

4.3 Analysis Procedure

4.3.1 Data Reduction

The interfacial debond loads are extracted from the indentation load-deflection curves via the shear lag formulation of Zidi et al. [19]. The linear part of the curve is fitted to Equation 4-1. The variables u_0 and s_0 are the surface displacement of the fiber and the applied stress to the fiber respectively, both obtained from the load-deflection curve. The compression modulus of the fiber, E , for this work has been assumed equivalent to the tensile modulus. The value n is determined by linearly fitting the curve and incorporates the effect of the matrix properties and the mean distance of surrounding fibers.

$$u_0 = \frac{s_0}{nE} \quad 4-1$$

The nonlinear portion of the curve is fitted with Equation 4-2, which takes into account that a debonded region exists, and that the shear stress due to friction in that region is equal to the interfacial shear strength. The debonding stress, s_d , represents the normal stress at which interfacial debonding occurs, but note that the nonlinear region in the curve is not necessarily related to debonding but could also be a sign of matrix or interfacial yielding [19].

$$u_0 = \frac{1}{2nE} \left(\frac{s_0^2}{s_d} + s_d \right) \quad 4-2$$

The current analysis does not take in to account the possible effects of plasticity. The interfacial shear stress is then obtained by Equation 4-3. All quantities are now known to solve Equation 4-3 with a equal to the fiber radius. The average fiber radii for the fibers

were used in these calculations, but a more accurate result can be obtained by actual measurements of each individual fiber indented.

$$t_d = \frac{ans_d}{2} \quad 4-3$$

The result of the curve fit is shown in Figure 4-8 plotted with the experimental data points obtained from nanoindentation.

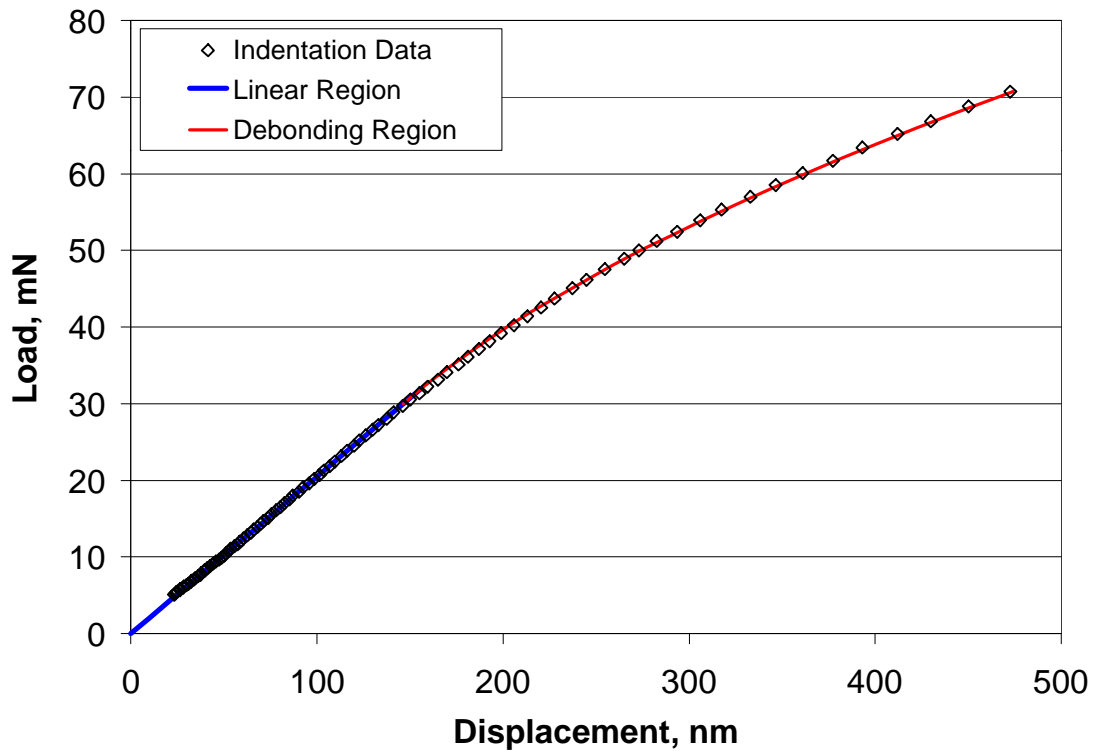


Figure 4-8. Curve Fits to Experimental Load-Deflection Curve through the Analysis of Zidi et al. [19]

4.3.2 Statistical Analysis

Weibull statistics are employed to define the variability of the interfacial shear strength due to its acceptance in the fiber-reinforced polymer composites community for describing the probability of failure for these material systems [31,32]. The cumulative

probability distribution function describing the distribution of measured values is given by Equation 4-4.

$$F(x) = 1 - e^{-\left(\frac{x}{\beta}\right)^\alpha} \quad 4-4$$

The two parameters used to fit the data are α and β . The value of α (the shape parameter) determines the breadth of the distribution while β (the location parameter) defines the value most closely representing the center of the distribution. The normal mean, normal standard deviation, Weibull mean, Weibull standard deviation, and Weibull distribution are calculated for each set of fiber indents, excluding indents where fiber splitting or crushing occurs. An example Weibull distribution curve for the G' sized composite system is shown in Figure 4-9.

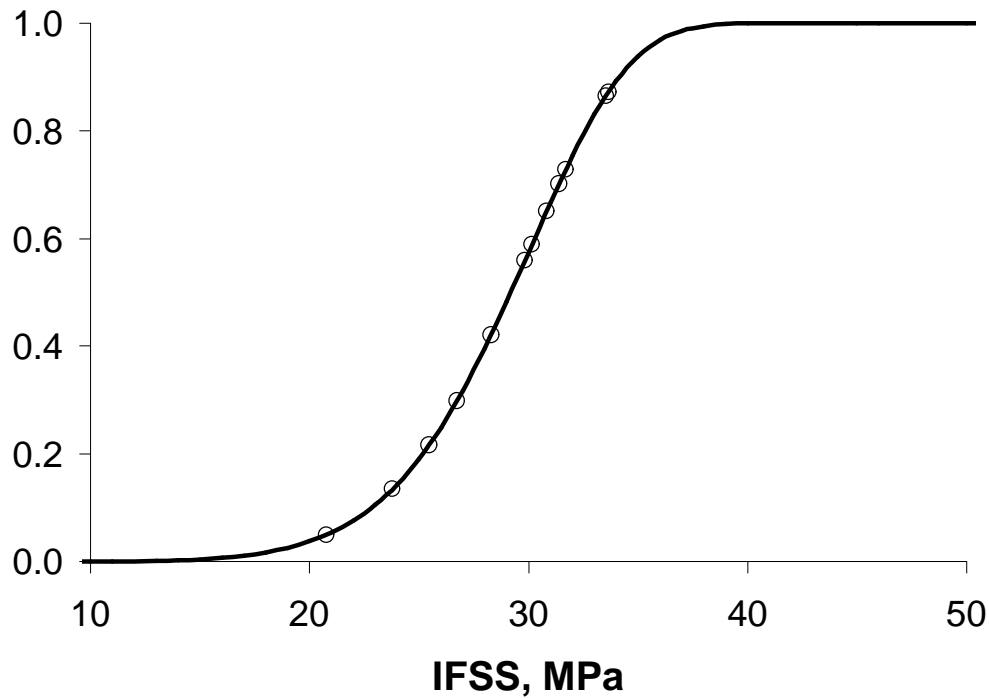


Figure 4-9. Weibull Probability Distribution Function of G' Sized Fiber Interfacial Shear Strength

Chapter 5 Results and Discussion

5.1 Evaluation of the Nanoindentation Technique

5.1.1 Sample Polishing

The importance of sample preparation, polishing in particular, was mentioned several times in Chapter 2 as key to the success of microindentation. Desaegeer and Verpoest [15] showed a 40% difference in debonding loads by simply changing the polishing procedure. The two important goals in polishing are to introduce very little interfacial stresses, causing premature interfacial cracking (denoted by black circles around the fibers), and produce a very flat surface with very little relief between the fiber and matrix. It is more likely for a fiber to split or crush if the fiber is raised above the surface. Standard metallographic techniques scrub the matrix away from the very hard carbon fibers, but the procedure outlined in Chapter 4 is designed to eliminate this problem. Scanning electron microscope (SEM) images of the carbon/vinyl ester polished surface are shown in Figure 5-1 and Figure 5-2.

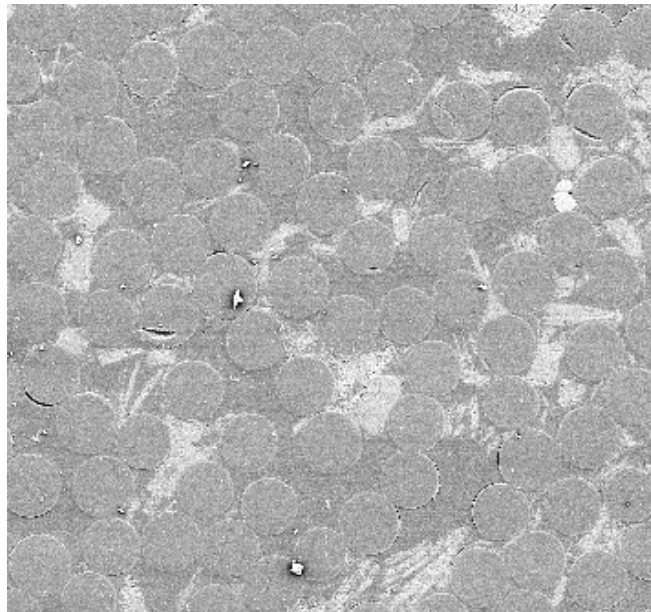


Figure 5-1. SEM Image of Polished Carbon/Vinyl Ester Surface (Large Field)

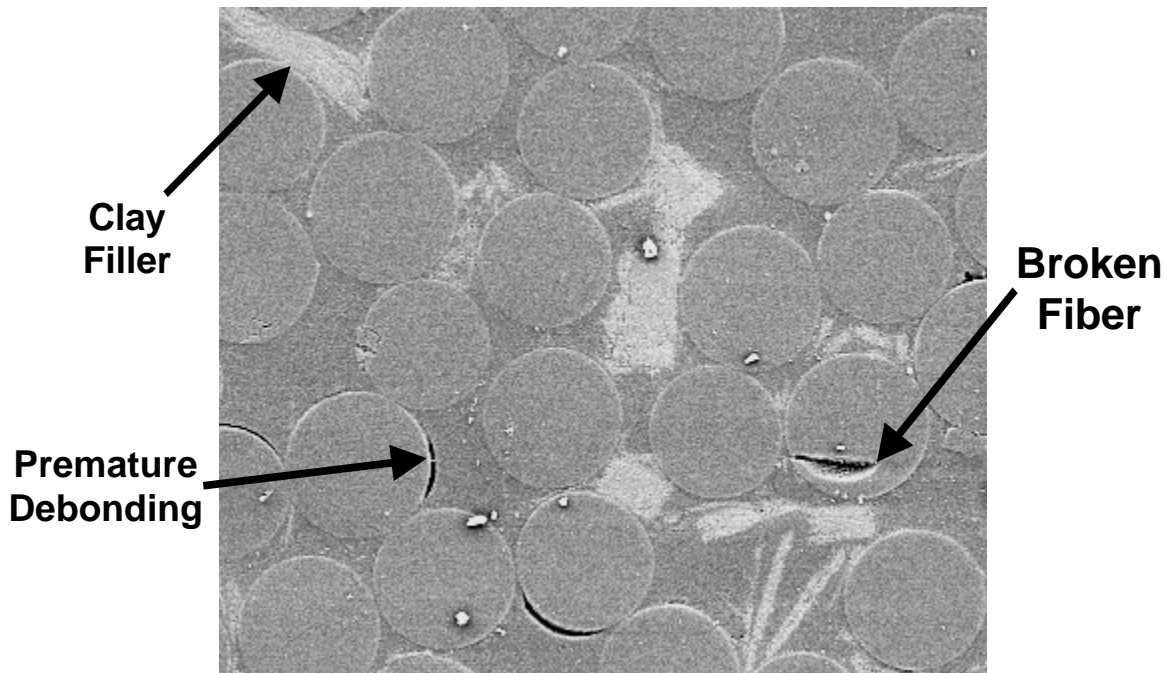


Figure 5-2. SEM Image of Polished As-Received Carbon/Vinyl Ester Surface (Narrow Field)

The majority of fibers show no premature interfacial debonding and appear to be level to the matrix surface. The black circles around some of the fibers could be the result of polishing but are more likely the result of residual stresses and other processing irregularities.

5.1.2 Resolution of the Nanoindenter

The nanoindenter used in these experiments is very sophisticated with high resolutions on load, displacement, and positioning. Positioning of the indenter is very important to the success of the interfacial test because the carbon fibers are only six to eight microns in diameter. Table 5-1 shows the resolution of the nanoindenter used in this study compared with the accuracy of the instruments discussed in the works of previous authors. The NANO II indenter is superior in the measurement of normal load and displacement to the other instruments. The x-y table on the NANO II is also only 0.1 micron less accurate than the best x-y table in Table 5-1, making it ideal for fiber

selection and accurate positioning. Overall, the instrument used in this study has the capability of producing more reliable results from the microindentation technique than from previous research.

Table 5-1. Resolutions of Instruments used for Microindentation

Instrument	Researcher	Load	Normal Displacement	X-Y Table
		$\pm nN$	$\pm nm$	$\pm mm$
NANO II	Present Study	75	0.04	0.2
Microindenter	Mandell et al. [14]	100	N/A	1
Nanoindenter	Deseager et al. [15]	1,000	1	2
Microindenter	Chateauinois et al. [18]	1,000,000	50	0.1

5.1.3 Selection of Indenter Tip

Initially, a Berkovich diamond, pyramidal tipped indenter was used to make the interfacial measurements with the nanoindenter. The resulting load-displacement curves did not show any conclusive evidence of debonding. In fact, at the loads where debonding is present, the stiffness of the system increases as shown in Figure 5-3 rather than decreasing as expected. Fiber splitting was a major problem, resulting in a poor success rate of accomplishing the load cycle. There was also concern that the plastic deformation of the fiber surface was causing a complex stress state at the interface near the surface, the place where debonding is assumed to occur at the maximum shear stress.

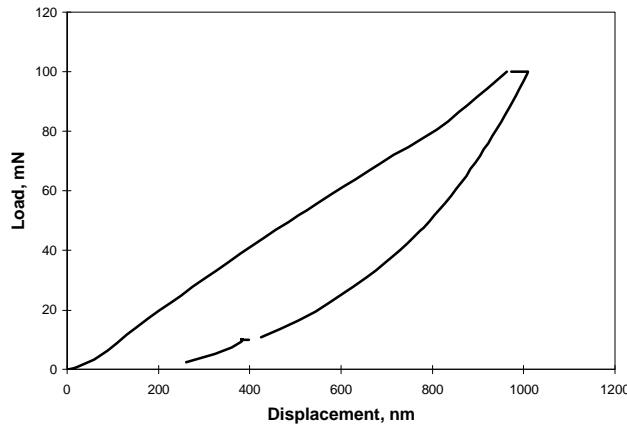


Figure 5-3. Nanoindentation Load-Displacement Curve for G' with Berkovich Indenter

The blunt tipped indenter is a conical diamond ground flat to about four microns in diameter. The flat tip eliminates the large stress concentration caused by the pyramidal tip, and from visual observations, it appears to cause little to no plastic deformation of the fiber surface. The flat shape loads the fiber in the manner sought after by Kharrat et al. [18] and Zidi et al. [19]. The preceding authors achieved similar results by subtracting the indentation curve of bulk fiber material from the microindentation curve accomplished using a pyramidal shaped indenter, but the use of the blunt indenter eliminates this step and possible source of error. The one concern with the blunt indenter is the difficulty in loading the fiber flush, which is dependent mostly upon mounting the specimen flat in the instrument relative to the surface on the indenter tip. A contact zone is observed at the beginning of each fiber test where the blunt indenter is coming into full contact with the fiber.

5.1.4 Continuous Stiffness Measurements

The continuous stiffness mode on the nanoindenter works very much like a dynamic mechanical analyzer, or DMA. The indenter head is oscillated at a peak-to-peak distance of one to five nanometers at 45 Hz. The results include a continuous stiffness measurement and a measurement of the phase angle. It was hypothesized that these measurements would show the debonding of the fiber from the matrix as a reduction in stiffness, but unfortunately, the progressive nature of debonding only shows a gradual reduction in stiffness. This same behavior was observed in the load-deflection curves. Figure 5-3 shows the correlation between the displacement-load curve and the stiffness-load curve and how those curves correlate to the physical processes taking place in the composite. In the diagram the contact zone (1) is followed by fiber compression (2), which is purely elastic deformation of the fiber/matrix/interphase system. The maximum shear stress, which occurs within a fiber diameter of the surface, causes a debond to occur (3) just below the polished surface. The debond then propagates in both directions (3), causing a gradual reduction in system stiffness as the support of the matrix and surrounding fibers is lost. At some point in time, the debonding stops and elastic compression (4) is once again observed. The unstable, unsupported fiber then buckles or

crushes under the applied load (5). These five processes can be observed in both the displacement-load curve and the stiffness-load curve.

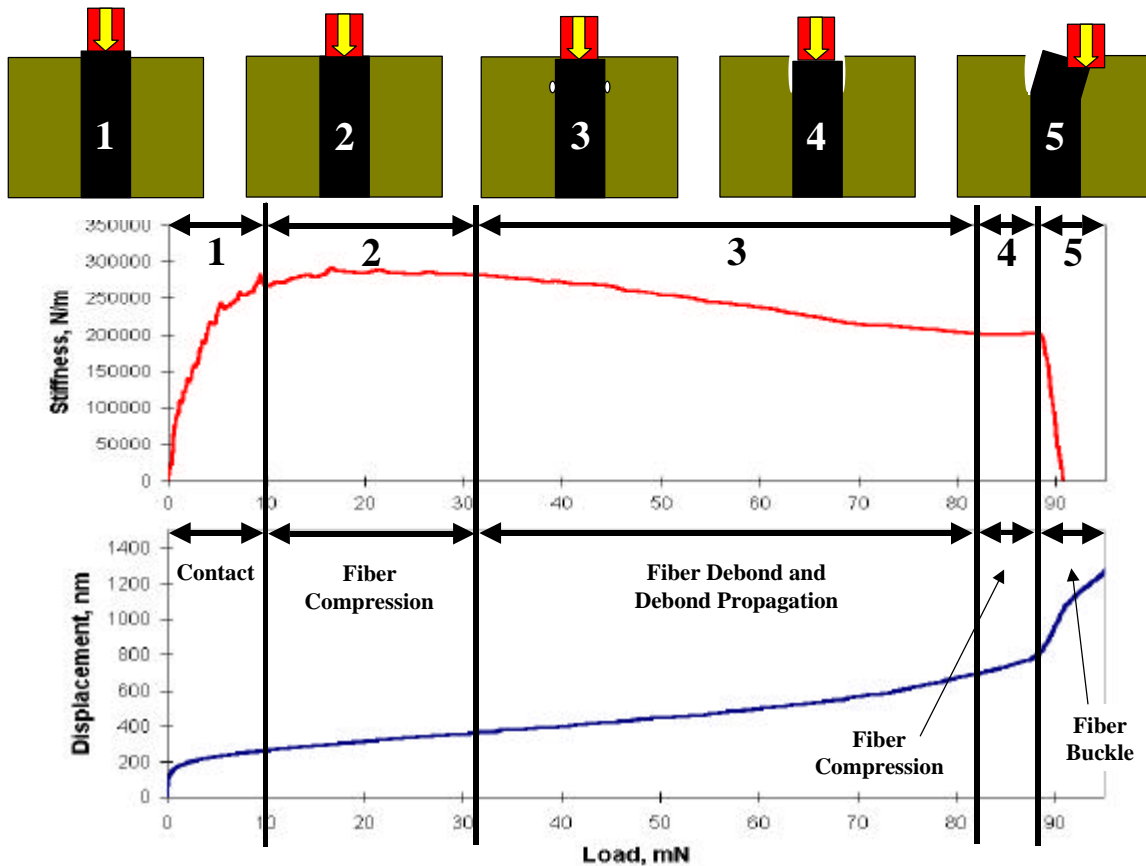


Figure 5-4. Description of Fiber/Matrix Behavior during Indentation Test

5.1.5 Verification of Debonding

Tests were run on single fibers at increasing loads to determine the onset of debonding by visual observation. The goal was to confirm that the change in slope of the load-displacement curve related to debonding on the surface, indicated by a full or partial black ring around the fiber. The tests revealed that repeated loading of the same fiber at increasing load levels caused a progressive reduction in the stiffness of the system. The reduction in stiffness can be related to either fiber/matrix debonding or matrix/interphase yielding. Debonding around the fiber was discovered through evaluation with the optical microscope, but not until very high loads at levels above the expected debond loads. The

progressive reduction in stiffness in the G' composite is shown in Figure 5-5 and Figure 5-6. The stiffness remains constant when loaded to 30 mN and 35 mN, but then begins to diminish at 40, 45 and 50 mN. The G' fibers evaluated typically debond between 30-35 mN of applied load, which is confirmed by this experiment. After debonding when loaded to 35 mN, the next indent on the same fiber shows the reduced stiffness that is incurred. The same phenomenon was observed on all fibers loaded at increasing increments. The progression of debonding on a fiber is shown in Figure 5-7 from optical microscope photos. An SEM image of a G' prime fiber loaded to 70 mN is shown in Figure 5-8 with the distinctive black ring representative of debonding. It can also be noted from this picture that no surface damage/plastic deformation is caused by the blunt indenter tip.

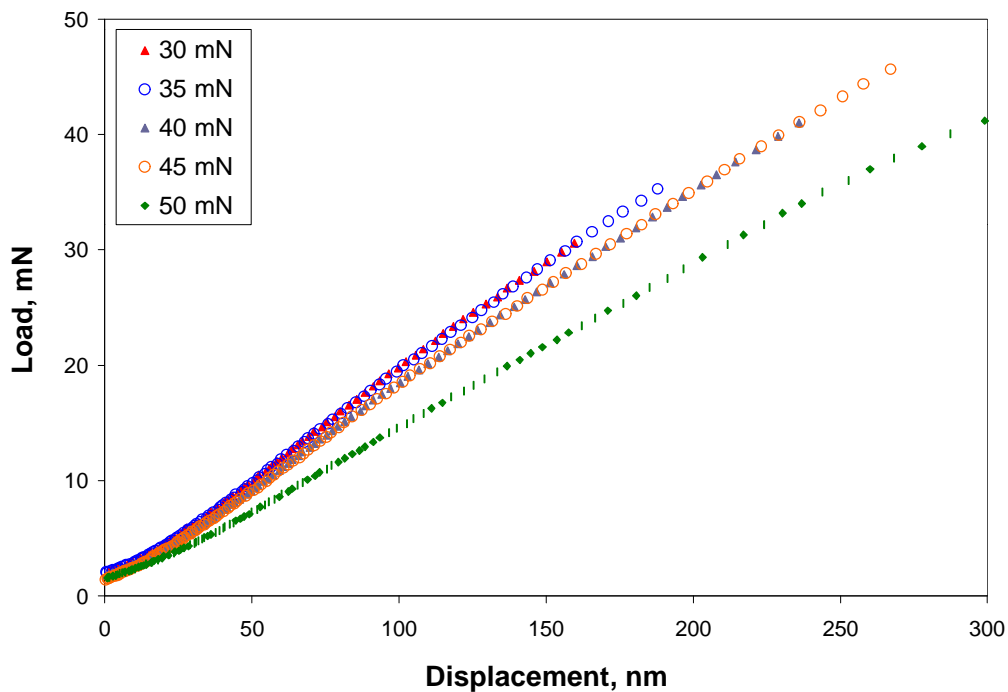


Figure 5-5. G' Single Fiber Load-Displacement Curves, Increasing Maximum Load

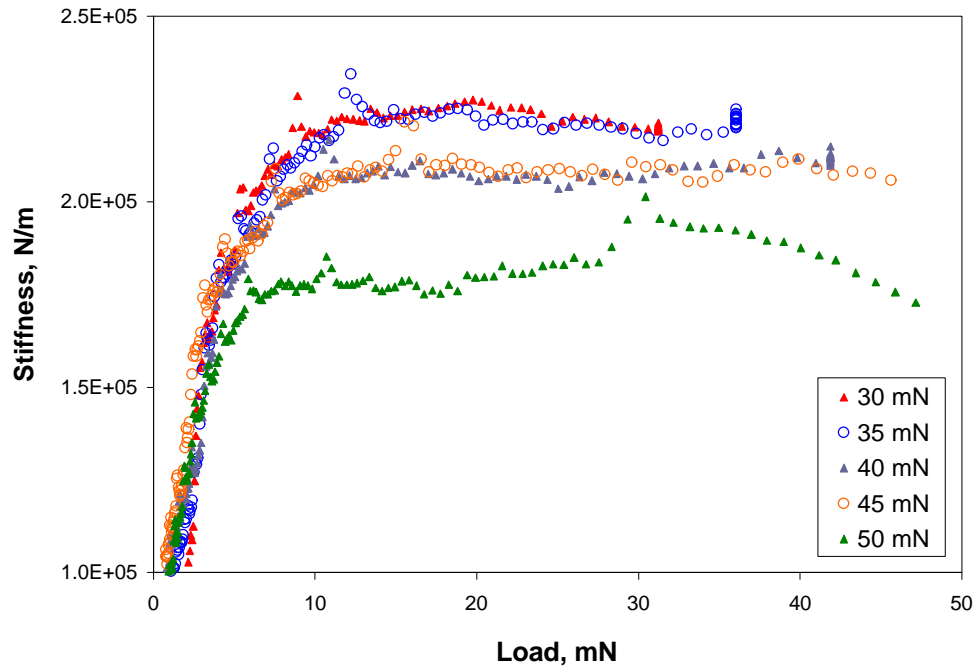


Figure 5-6. G' Single Fiber Stiffness-Load Curve, Increasing Maximum Load

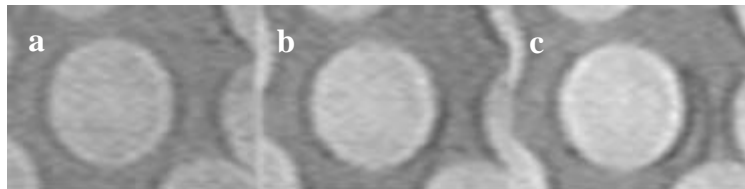


Figure 5-7. Progressive Debonding of the G' Fiber (a) 0 mN (b) 65 mN (c) 70 mN

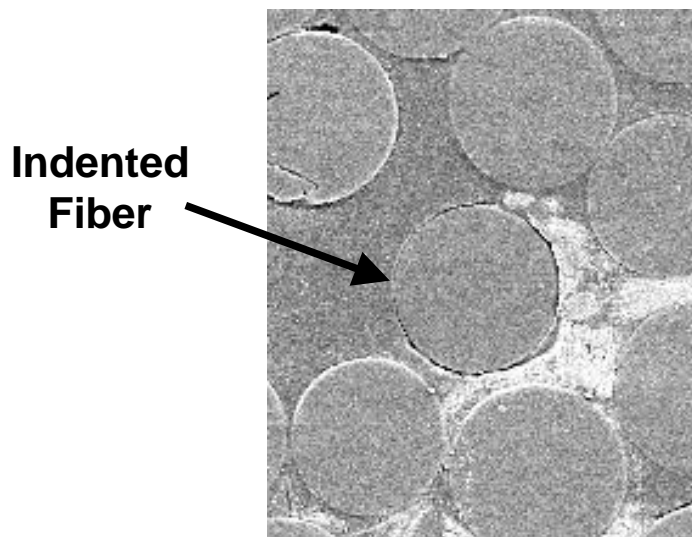


Figure 5-8. SEM Image of Fiber/Matrix Debond as a Result of Microindentation

5.2 Evaluation of Analysis Method

5.2.1 Finite Element Analysis

A finite element analysis was conducted to examine the validity of the shear lag analysis used to determine interfacial shear strength. The analysis was conducted using known fiber, matrix, and bulk composite properties. Unknown properties were predicted or estimated using micromechanical approximations. A schematic of the finite element geometry constructed using ANSYS is shown in Figure 5-9. The properties used for the analysis are shown in Table 5-2. A solid axisymmetric 4-node quad element was used for this analysis, and the mesh was biased to the fiber matrix interface.

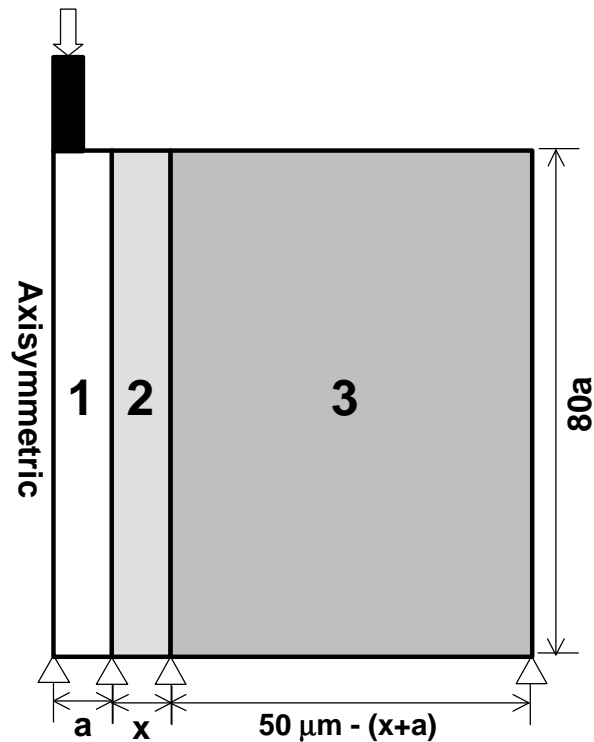


Figure 5-9. Schematic for the Finite Element Analysis

Table 5-2. Properties for the Finite Element Analysis

	PVP and LSP			G'		
	1	2	3	1	2	3
	Fiber	Matrix	Composite	Fiber	Matrix	Composite
E_x (GPa)	20.0	3.4	13.3	20.0	3.4	13.3
E_y (GPa)	228.0	-	130.0	241.0	-	130.0
E_z (GPa)	20.0	-	13.3	20.0	-	13.3
ν_{xy}	0.25	0.30	0.247	0.25	0.30	0.247
ν_{yz}	0.0219	-	0.0236	0.0219	-	0.0236
ν_{xz}	0.27	-	0.18	0.27	-	0.18
G_{xy} (GPa)	28.0	-	4.65	28.0	-	4.65
G_{yz} (GPa)	28.0	-	4.65	28.0	-	4.65
G_{xz} (GPa)	7.9	-	2.325	7.9	-	2.325
a (mm)	3.57	X	X	3.37	X	X

The geometry from two fiber tests, one on LSP and one on G', were modeled and used to compare to the shear lag analysis. The matrix thickness, x , was determined as the average distance to the surrounding fibers. The LSP fiber selected had an average distance to the nearest fiber of about 3.4 μm , and the G' fiber selected had an average distance to the nearest fiber of about 1.7 μm (assuming average fiber diameters in both cases). The two fibers evaluated are imaged in Figure 5-10 and Figure 5-11. The shear stresses at the interface and the downward translation of the fiber were calculated and compared to the shear lag distributions given by Equation 2-16 and Equation 2-18. The comparison was made in the linear experimental region at a load value of 30 mN, with the constant n (representative of the global stiffness value) equal to 17.3 mm^{-1} and 23.7 mm^{-1} for the LSP and G' fibers respectively. The shear stress distributions are shown in Figure 5-12, and the displacement distributions are shown in Figure 5-13. There is a 101% difference in the maximum interfacial shear stress for the LSP composite between the finite element result and the experimental shear lag result, but there is only a 64% difference for the G' composite. The finite element result for maximum fiber translation is 30% lower than measured for the LSP composite and 17% lower for the G' composite.

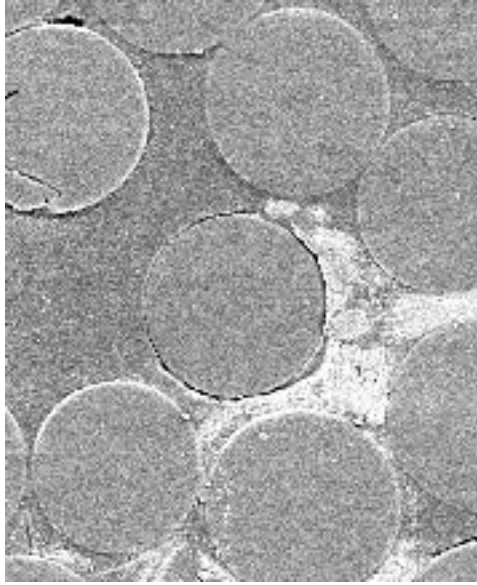


Figure 5-10. SEM image of G' Fiber Evaluated using FEA

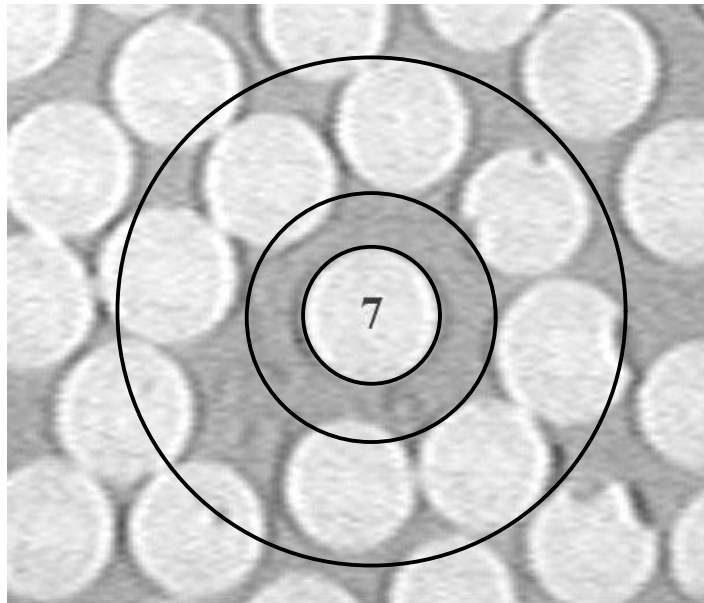


Figure 5-11. Optical Microscope Image of LSP Fiber Evaluated using FEA

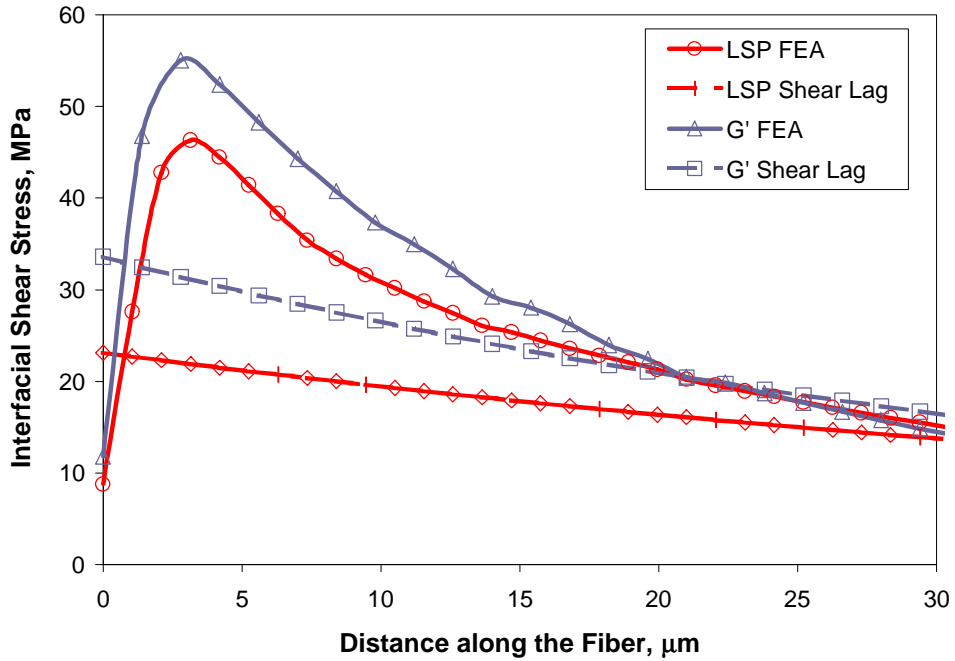


Figure 5-12. Comparison between FEA and Shear Lag Interfacial Shear Stress Distributions for LSP and G' Composites

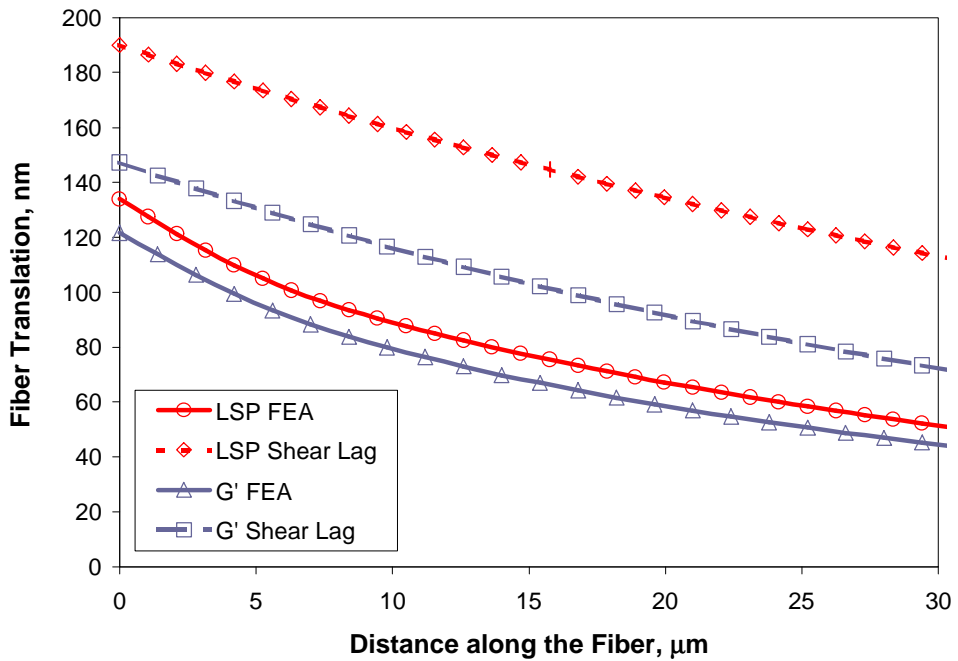


Figure 5-13. Comparison between FEA and Shear Lag Fiber Translation Distributions for LSP and G' Composites

The improved validity between shear lag and finite element for the G' composite is not surprising and is not unique for these particular fiber tests. Overall, the finite element model represents a stiffer system than what has been seen experimentally. The average global stiffness constant k , which takes into account matrix properties and the effects of surrounding fibers, was 224.3 MPa/ μm for the G' fibers tested and 146.9 MPa/ μm for the LSP fibers tested. This increase in the global stiffness constant is not purely a result of the G' composite having a higher volume fraction. The local volume fractions in the regions tested for the LSP and G' composites were nearly the same, i.e. the distances to the nearest fibers were about the same on average. The difference in global stiffness is a result of the different fiber sizings applied the material. The PHE sizing applied to the LSP is known to be more compliant than that of the G', therefore resulting in a more compliant stiffness measurement. It is for this reason, the finite element agreement is better with the G' composite, whose interphase properties are more like those of the matrix. Ho and Drzal [16] discussed the importance of including an interphase region in the finite element model in order to obtain accurate results due to the significant effects. This feat is difficult to accomplish, however, with limited knowledge of the interphase properties, especially on the LSP and PVP thermoplastic sized composites where diffusion occurs into the matrix and a gradient of properties is created [25]. The gradient of properties extending out from the fiber into the matrix region is shown in Figure 5-14. These results were obtained by indentation with an atomic force microscope from a bi-layer blend of PHE and vinyl ester.

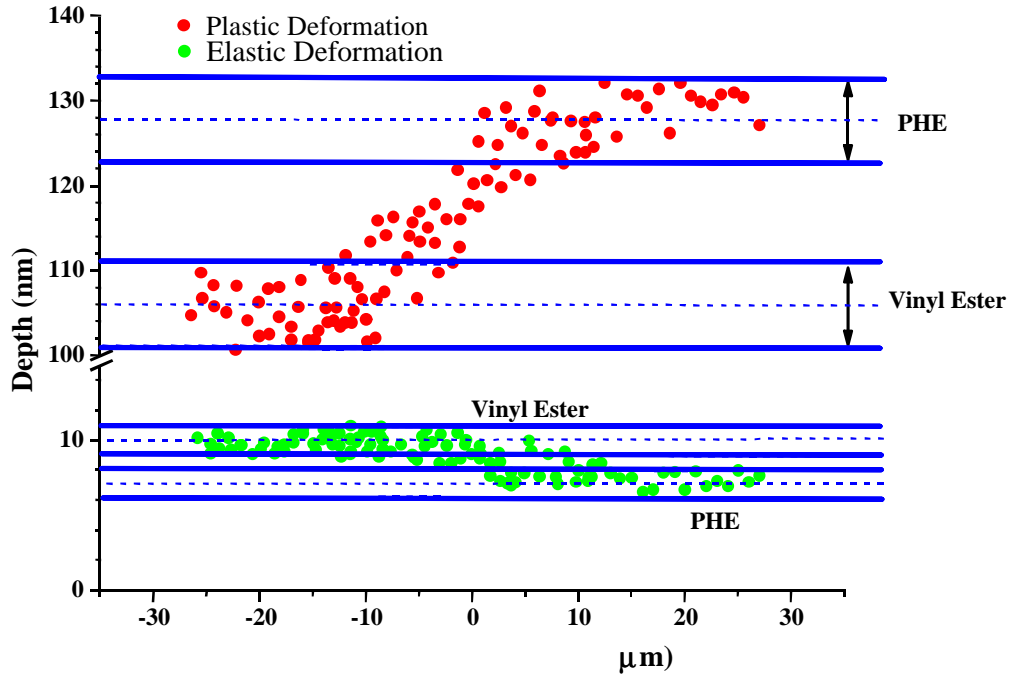


Figure 5-14. Indentation across a Bi-Layer Blend of PHE and Vinyl Ester [25]

The finite element model can be adjusted by matrix thickness to account for the lack of the interphase in the model. Increasing the matrix thickness leads to higher deformation and a decrease in interfacial shear strength, both approaching the shear lag analysis results. The effect of matrix thickness on the finite element fiber translation results for the G' material is shown Figure 5-15. The measured average value of 1.65 microns is increased to 3, 4, and 5 microns. At a matrix thickness of 5 microns, the finite element result for maximum displacement matches the measured fiber translation from the microindentation test. The interfacial shear stress does not, however, match the shear lag result at the same matrix thickness as shown in Figure 5-16 with a 21.7% difference in maximum interfacial shear strength. Overall, there is a 4.1 MPa change in maximum interfacial shear strength per 1 μm of matrix thickness.

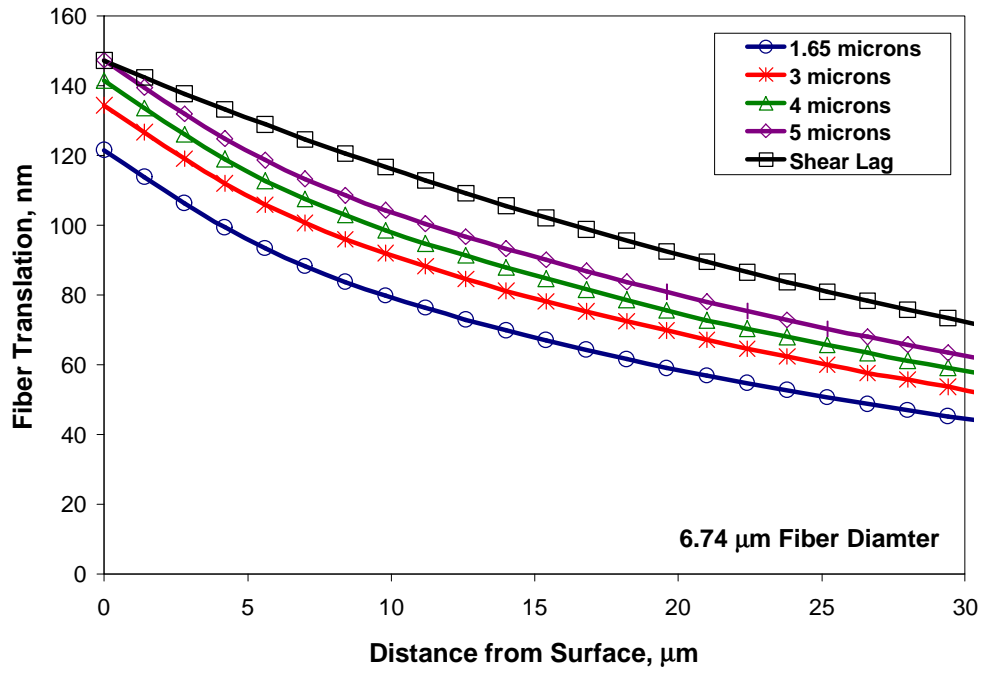


Figure 5-15. Effect of Matrix Thickness on Fiber Translation in G' Material

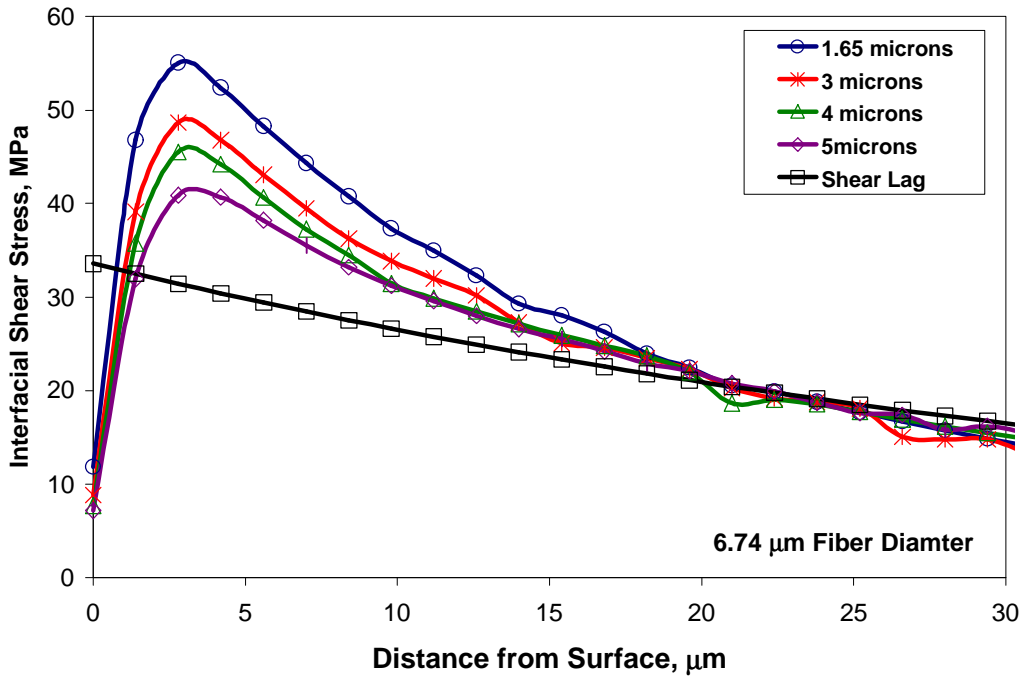


Figure 5-16. Effect of Matrix Thickness on Interfacial Shear Stress in G' Material

Since fiber diameter was not measured accurately in the experimental study, the fiber diameter was varied from six to eight microns to see the effect on fiber translation and interfacial shear stress. The increase in fiber diameter causes a decrease in fiber translation (Figure 5-17), but Figure 5-18 shows that the same increase causes a significant decrease in interfacial shear stress. There is a 13.7 MPa decrease in interfacial shear strength per 1 μm increase in fiber diameter. It appears that adjustments made to the fiber diameter and the matrix thickness can lead to a result closely resembling the shear lag analysis. The finite element result better resembles the shear lag result when using an 8 μm fiber diameter and a 5 μm matrix thickness. The maximum translation is within 12.8% and the maximum interfacial shear stress is within 9.8%. The sensitivity of the finite element analysis to these properties make its validity questionable when comparing it to an experimental situation. The shear lag analysis has inherent problems due to the assumptions made in its derivation, but it is apparent that finite element analysis has its limitations as well.

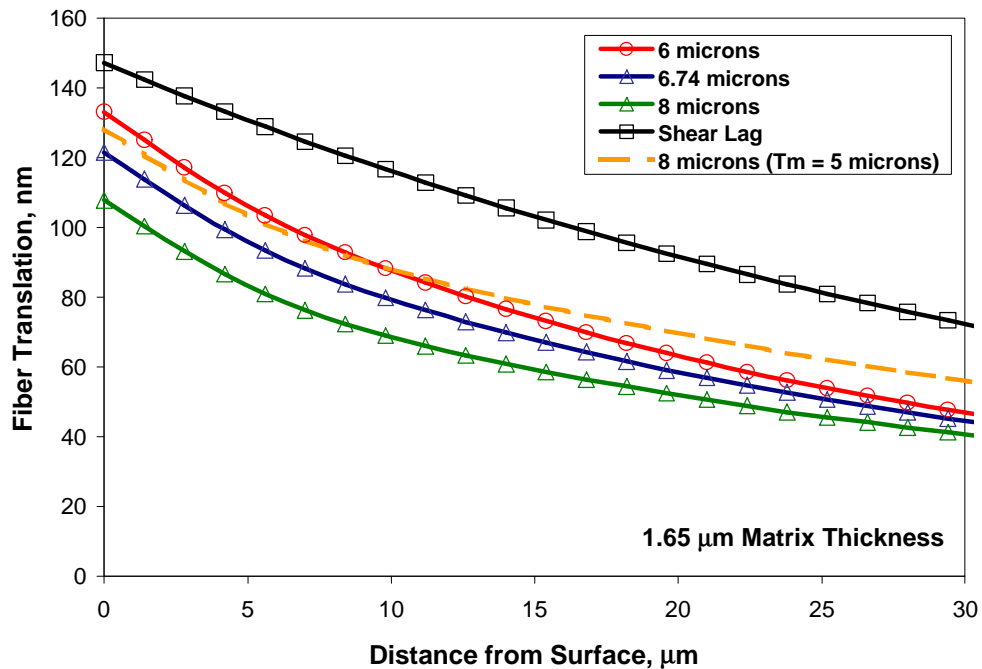


Figure 5-17. Effect of Fiber Diameter on Fiber Translation in the G' Material

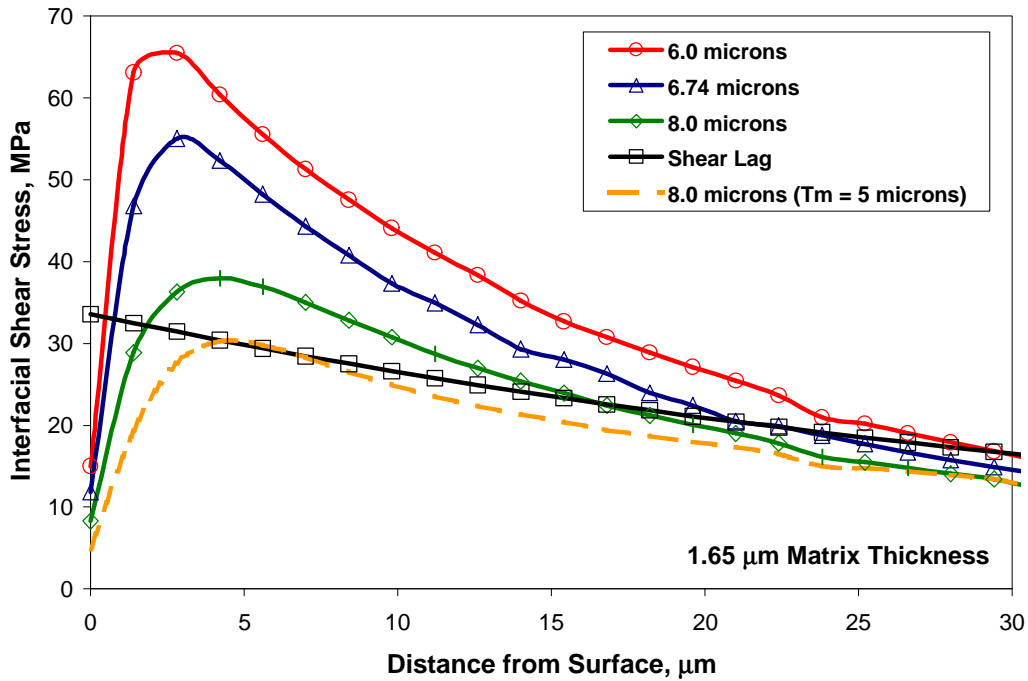


Figure 5-18. Effect of Fiber Diameter on Interfacial Shear Stress in the G' Material

5.2.2 Inclusion of Poisson Effects in Shear Lag Analysis

The shear lag analysis by Zidi et al. [19] is a very simple analytical tool for extracting interfacial shear strength plus it takes into account the effect of the real surroundings of the fiber, including matrix/interphase properties and the role of surrounding fibers. The analysis does not, however, include the effects of transverse radial stresses that increase and change during loading. The Poisson effect is one of the causes of these radial stresses because as the fiber is loaded the diameter expands in relation to the normal force applied, thus causing compressive radial stresses to develop along the fiber. These radial forces affect the normal strain in the fiber, and thus could have an impact on the value n , which is obtained by fitting the linear portion of the indentation load-displacement curve. The value of n is important in obtaining an accurate interfacial shear strength value.

Gao et al. [33] performed a rod-cylinder analysis on a fiber being pulled from the matrix and included the Poisson effects for calculations in the debonded zone. The attempt in this study is to utilize the term that is derived in Gao et al. [33] to add radial stresses to the analysis by Zidi et al. [19] in the bonded region to determine its affect on interfacial stresses and the value of n . The stress-strain relationship adopted from Gao et al. [33] is shown in Equation 5-1. The term is based on the Poisson ratios, elastic moduli, and volume fractions for the fiber and matrix.

$$\frac{du}{dx} = \frac{\mathbf{s}_f}{E_f} - \frac{2\mathbf{u}_f}{E_f} q^*$$

where:

$$q^* = \frac{\mathbf{a}\mathbf{u}_f\mathbf{s}_f - \mathbf{g}\mathbf{u}_m\mathbf{s}_m}{\mathbf{a}(1-\mathbf{u}_f)+1+\mathbf{u}_m+2\mathbf{g}} \quad 5-1$$

$$\mathbf{a} = \frac{E_m}{E_f}$$

$$\mathbf{g} = \frac{V_f}{V_m}$$

The matrix normal stress is set to zero because one of the initial shear lag assumptions is that the matrix carries no normal load and only shear. Differentiating Equation 5-1 with respect to x , and after a change in sign conventions, the resulting equation is shown in Equation 5-2.

$$\frac{d^2u}{dx^2} = -\frac{d\mathbf{s}_f}{dx} + \frac{2\mathbf{u}_f}{E_f} \left(\frac{\mathbf{a}\mathbf{u}_f \frac{d\mathbf{s}_f}{dx}}{\mathbf{a}(1-\mathbf{u}_f)+1+\mathbf{u}_m+2\mathbf{g}} \right) \quad 5-2$$

Collecting terms together yields Equation 5-4.

$$\frac{d^2u}{dx^2} = -\frac{1}{E_f}(1-K)\frac{ds_f}{dx} \quad 5-4$$

$$K = \frac{2au_f^2}{a(1-u_f) + 1 + u_m + 2g}$$

After applying the force balance from Equation 2-11 and conditions from Equation 2-13 and Equation 2-14, the resulting differential equation, Equation 5-5, only differs from the original differential equation for the bonded region, Equation 2-15, by a factor of $1-K$. A typical value of K for the composites evaluated in this work is 0.000432 (60% volume fraction).

$$\frac{d^2u}{dx^2} - (1-K)n^2u = 0 \quad 5-5$$

After the application of boundary conditions, Equation 2-9 and Equation 2-10, the resulting equations for fiber translation and interfacial shear stress are shown in Equation 5-6 and Equation 5-7.

$$u(x) = \frac{s_0}{E_f n \sqrt{1-K}} e^{-nx\sqrt{1-K}} \quad 5-6$$

$$t(x) = \frac{ans_0\sqrt{1-K}}{2} e^{-nx\sqrt{1-K}} \quad 5-7$$

The resulting curve is shown in Figure 5-19 in comparison to the original result that does not include the Poisson effects. It can be seen from the figure that the Poisson expansion of the fiber causes only a 0.02% increase in maximum interfacial shear stresses and fiber translation. The solution was carried out on a 60% volume fraction material using the properties of vinyl ester and AS-4 fibers and at a 30 mN indenter load. The radial stresses created due to the Poisson effect are not high enough to cause any change in the

shear lag results. The inclusion of the K parameter requires knowledge of matrix properties that are not known in as-processed composite, eliminating the simplicity of the empirical shear lag fitting method. Therefore, in this work the Poisson effect is not included in the analytical analysis of the nanoindentation test.

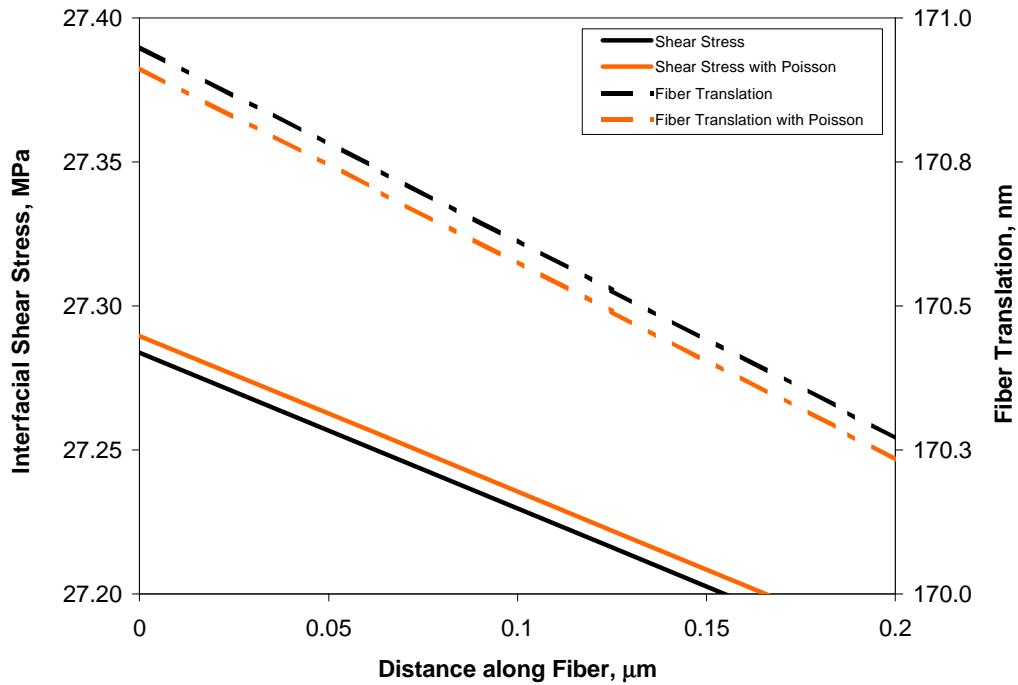


Figure 5-19. Fiber Poisson's Expansion Affect on Interfacial Shear Stress and Fiber Translation through Analytical Interpretation

5.3 Comparison of Fiber Sizings

5.3.1 Effect of Fiber Sizings on Interfacial Shear Strength

This study was conducted to compare the use of thermoplastic sizings to the industrial standard sizing, G'. Thermoplastic sizings are different in nature and diffuse into the surrounding matrix, making a gradient of properties. It is also believed that these thermoplastic sizings increase fiber/matrix adhesion. The results from the nanoindentation test, analyzed by the method outlined in Chapter 4, are shown in Figure 5-20. The plot shows that the standard industrial sizing performed better with regard to interfacial shear strength, followed closely by the LSP material and then the PVP material. The G' sizing also produced more consistent results, which can be seen by its superior Weibull modulus. The normal and Weibull means and standard deviations are shown in Table 5-3, along with the Weibull parameters α and β . It was previously believed that increased interfacial adhesion was the reason for improvement in static mechanical and enviro-mechanical properties for the thermoplastic sized materials, but these results seem to discredit that theory. The results could also suggest, however, that the test does not interrogate the interface in a meaningful way relative to the influence on composite strength.

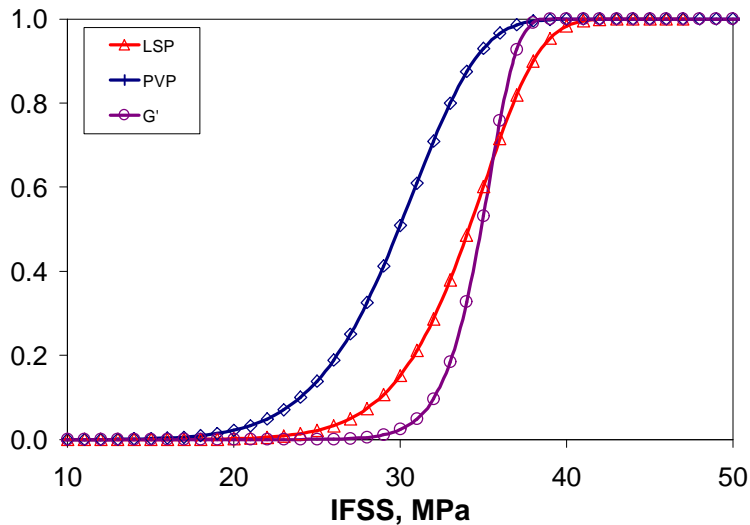


Figure 5-20. Weibull Cumulative Distribution Curves for the IFSS of Different Fiber Sizings

Table 5-3. Normal and Weibull Results for Interfacial Shear Strength

Sizing	Normal Mean	Normal Standard Deviation	Weibull Mean	Weibull Standard Deviation	α	β
LSP (22 fibers)	33.7 MPa	3.38 MPa	33.7 MPa	3.65 MPa	11.2	35.3
PVP (19 fibers)	29.5 MPa	3.68 MPa	29.5 MPa	4.11 MPa	8.6	31.2
G' (13 fibers)	34.6 MPa	1.71 MPa	34.6 MPa	1.92 MPa	22.4	35.4

5.3.2 Comparison to Microbond Technique

Increased interfacial adhesion was considered part of the reason for bulk composite property improvements because of the results obtained from microbond tests, a test for interfacial adhesion similar to fiber pull-out. The microbond results show that the G' sizing makes very little improvement in interfacial shear strength over an unsized fiber, but the PVP and especially the PHE sizings produced excellent results. Table 5-4 shows the microbond data as compared with the nanoindentation results. There are two sets of microbond results because the test is very sensitive to the vice used to hold the droplet of material during the pull-out process, and the vice was changed between the two series of tests. The new microbond data is somewhat suspect because the normalized PHE result of 84.8 MPa is 50% higher than the reported tensile strength for this sizing material. The original microbond data shows a 31% increase in interfacial shear strength of PHE over PVP with the same trend shown in the nanoindentation results but with an increase of only 14%. Complete agreement would not be expected because the microbond test is completed on a single fiber in a matrix that does not include the fillers and additives used in the pultrusion process, have the same residual stresses, or include the effects of neighboring fibers.

Table 5-4. Comparison of Nanoindentation and Microbond Results for IFSS

Sizing Material	Nanoindentation	Microbond [6]	New Microbond [34]
Unsize (<i>MPa</i>)	N/A	28 ± 8	53.5 ± 2.6
G' (<i>MPa</i>)	34.6 ± 1.7	33.0 ^a	63.0 ± 5.4
PVP (<i>MPa</i>)	29.5 ± 3.7	33.8 ± 6.5	64.5 ^b
PHE/LSP (<i>MPa</i>)	33.7 ± 3.4	44.4 ± 7.3	84.8 ^b

^aNormalized to microbond data based on the unsized fiber result

^bNormalized to the new microbond data based on the unsized fiber result

5.3.3 Tensile Strength Predictions

One of the main goals of this work is to predict bulk composite properties from micromechanical measurements. Many tensile strength models do not take into account the role of the fiber/matrix interphase region, but this region, formed by applied fiber sizings, can affect the tensile strength value and failure mode. Figure 5-21 shows failed LSP and PVP specimens, demonstrating the difference the fiber sizing causes. The LSP material shows a much more composite failure, while the PVP material shows a more brush-like or bundle strength type failure. This type of failure indicates more of an interfacial failure. Tensile strength predictions were made using the model by Gao and Reifsnider [21] and utilizing the MRLife12™ software [22]. The inputs for the model included fiber properties, matrix properties, and interfacial shear strength, all of which are shown in Table 5-5. Using typical properties for the composites tested, a plot was made showing the effect of interfacial shear strength on predicted tensile strength. It can be seen in Figure 5-22 that small changes in interfacial shear strength will not significantly effect bulk composite tensile strength as predicted by this model.

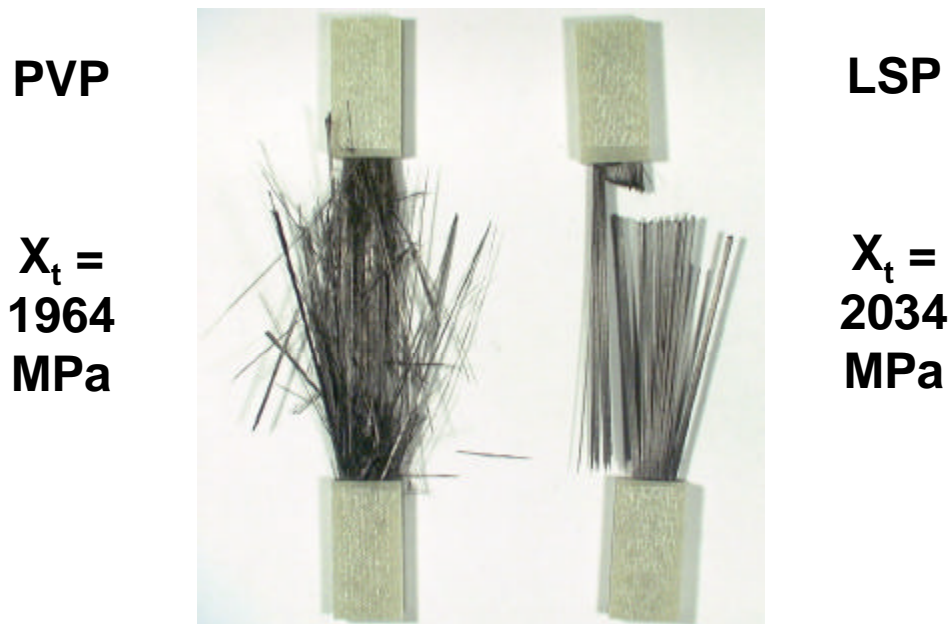


Figure 5-21. Comparison of Composite Tensile Failure for Two Different Fiber Sizings, PVP and PHE

Table 5-5. Tensile Strength Model Input Parameters

	LSP	PVP	G'
Fiber Properties			
E11	228 GPa	228 GPa	241 GPa
E22	20 GPa	20 GPa	20 GPa
G12	28 GPa	28 GPa	28 GPa
v12	0.25	0.25	0.25
v23	0.27	0.27	0.27
Xt	4.2 GPa	4.2 GPa	4.6 GPa
Xc	4.2 GPa	4.2 GPa	4.6 GPa
X0	5.2 GPa	5.2 GPa	5.2 GPa
m	10.65	10.65	10.65
Lo	1.0 mm	1.0 mm	1.0 mm
Diameter	7.1 μm	7.1 μm	6.7 μm
Matrix Properties			
E11	3.4 GPa	3.4 GPa	3.4 GPa
E22	3.4 GPa	3.4 GPa	3.4 GPa
G12	1.3 GPa	1.3 GPa	1.3 GPa
v12	0.30	0.30	0.30
v23	0.30	0.30	0.30
Xt	76 MPa	76 MPa	76 MPa
Xc	110 MPa	110 MPa	110 MPa
IFSS	33.7 MPa	29.5 MPa	34.6 MPa
Composite Properties			
Volume Fraction	57.7%	55.8%	60.8%
Gage Length	76.2 mm	76.2 mm	76.2 mm

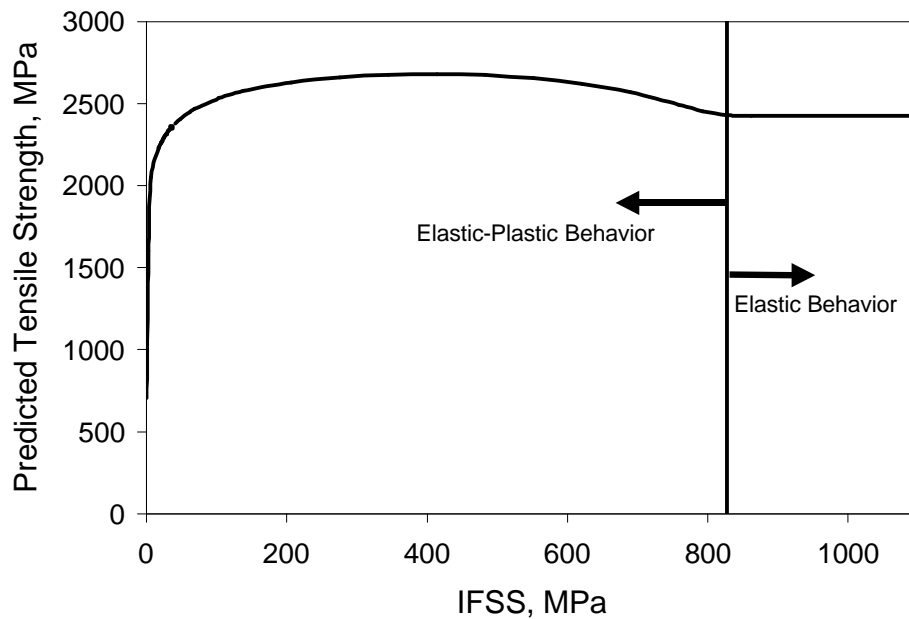


Figure 5-22. Predicted Tensile Strength versus Interfacial Shear Strength [35]

The results for the three sizing materials were obtained using the interfacial shear strengths from the nanoindentation and microbond tests for comparison in Figure 5-23. The predicted values for the LSP and PVP composites are within 1% to 5% of the experimental values; however, the model overpredicts the G' strength by 24% to 29%. This is most likely due to the processing difficulties encountered with this fiber. The results indicate that although the nanoindentation test is performed on an as-processed material, not all aspects of processing are taken into account. Fibers that are in good condition and bonded to the matrix are chosen for the testing, which eliminates broken fibers and partially debonded fibers from analysis. The nanoindentation test also requires the testing of fibers not in contact with other fibers, which could also have an impact on the result. Overall, the model by Gao and Reifsnider [21] does well in predicting the tensile strengths of these particular unidirectional composites, but it does not incorporate the effects of processing and is not heavily influenced by differences in interfacial shear strength.

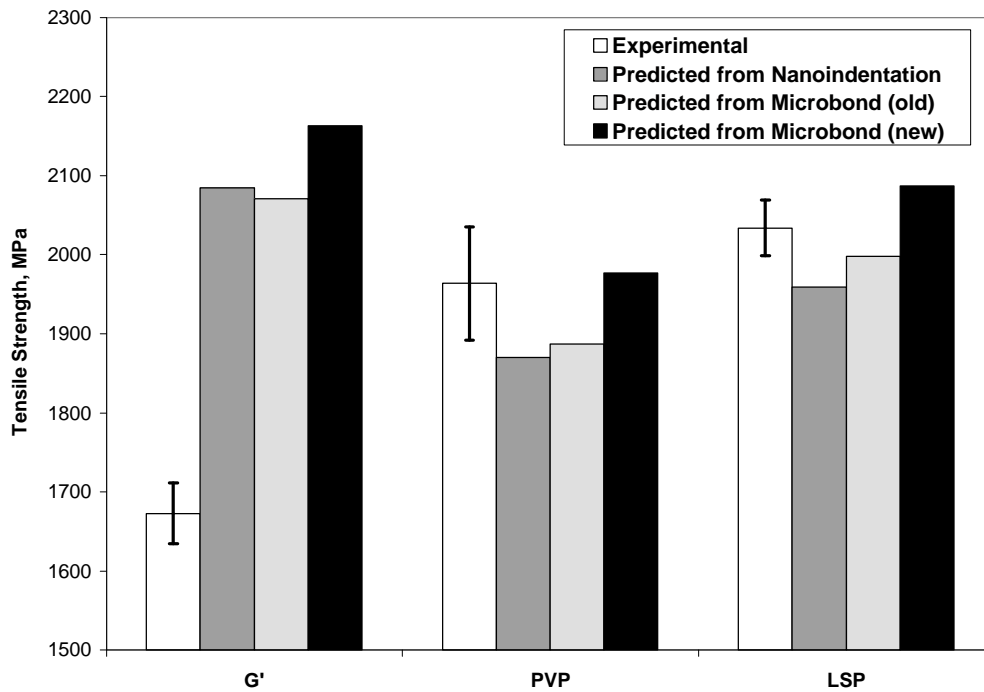


Figure 5-23. Comparison of Experimental and Predicted Tensile Strength Values

5.4 Effects of Hygrothermal Aging on IFSS and Composite Strength

5.4.1 Effect of Hygrothermal Aging on Interfacial Shear Strength

The diffusion of moisture into a composite is known to cause damage resulting in a decrease in properties. The G', PVP, and LSP composites all demonstrated reductions in tensile strength after saturation with water [9]. Until this point, the behavior of the interface during moisture diffusion has been unknown, but with the use of nanoindentation and the microindentation technique, the effect of hygrothermal aging on the fiber/matrix interface is explored. The 65°C moisture uptake curves for the 152.4 mm LSP and PVP tensile specimens are shown in Figure 5-24. Neat PVP is known to be hydrophilic and attract water to the interface, while the LSP is more hydrophobic. The hydrophilicity of PVP seems to be reduced, however, when complexed with matrix resin. The difference in this characteristic can be seen by the different levels of moisture diffusion in Figure 5-24. Samples were removed at 24, 96, 240, 288, and 576 hours for testing with nanoindentation. Additional samples were removed at 288 and 576 hours for tensile strength evaluation.

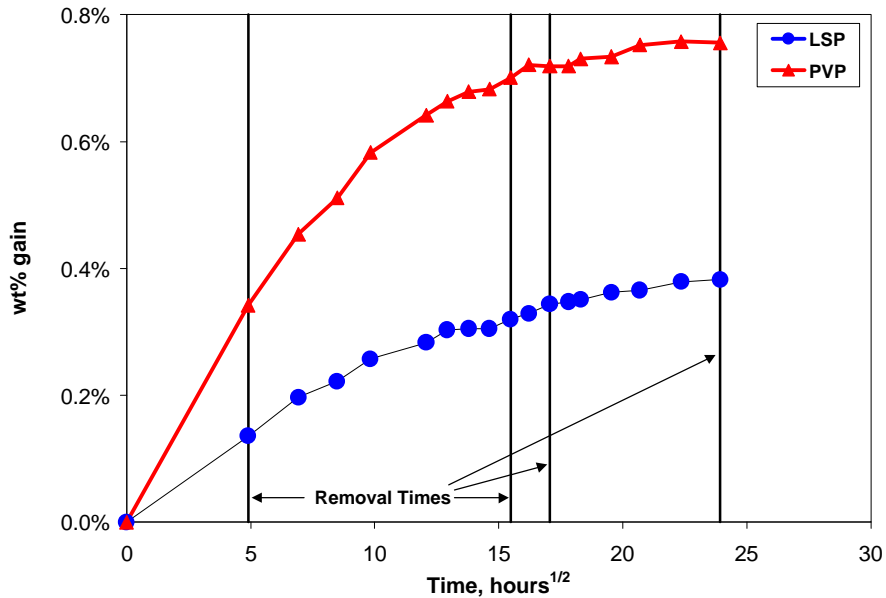


Figure 5-24. Moisture Uptake Curves for Composites in 65°C Water Bath

Specimens were kept wet to evaluate the effect of moisture in the sample. The resulting Weibull cumulative distribution curves are shown in Figure 5-25, Figure 5-26, and Figure 5-27. The LSP composite had an interfacial shear strength that increased up to 15% after 96 hours of moisture exposure. The trend then reversed, losing 10% of its original interfacial shear strength after 576 hours of exposure. It is believed that the increase in interfacial adhesion is due to either matrix swelling or chemical changes resulting from the moisture and temperature. Degradation of the interface began after 96 hours of exposure, overcoming the preliminary improvement in strength. The PVP composite showed the same improvement in interfacial shear strength with a 22% increase after 96 hours of exposure. The PVP interfacial shear strength then remained constant at additional aging times with the exception of the 288 hour results, which show a reduced increase. The low Weibull modulus for the 288 hour data suggests that this data may not be accurate due to either poor indenter or sample positioning. The increased interfacial adhesion observed in the PVP composite is possibly a result of matrix/interphase swelling or chemical changes. G' composites were only evaluated at 24 and 240 hours of moisture exposure and showed very quick reduction in interfacial shear strength, suggesting poor resistance to hygrothermal aging.

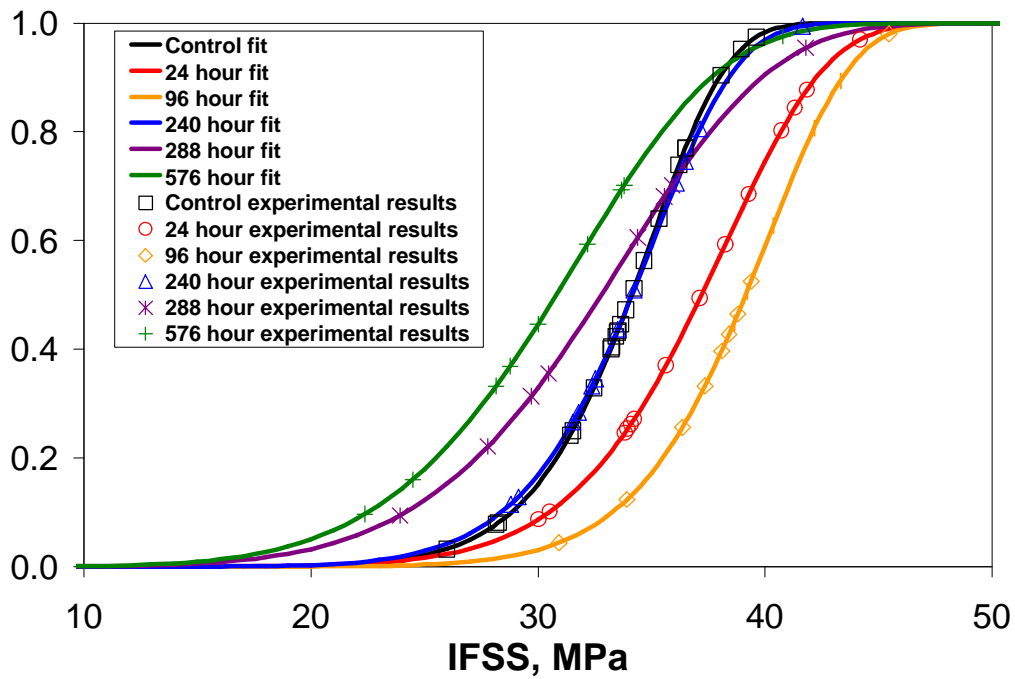


Figure 5-25. Weibull Cumulative Distribution Curves for LSP Aged in 65°C at for Different Aging Times

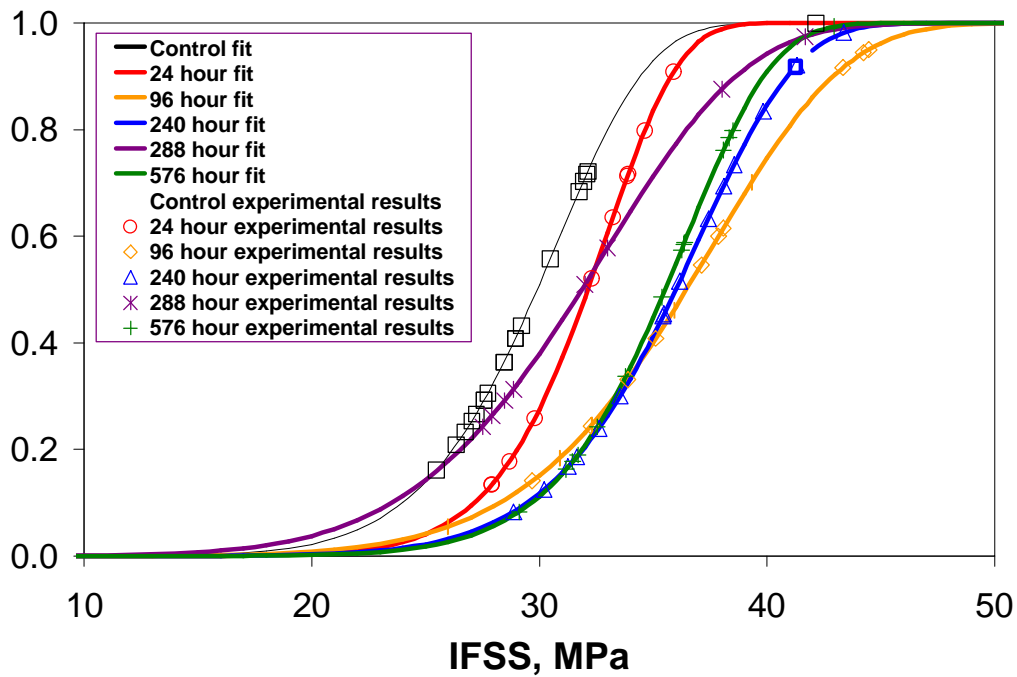


Figure 5-26. Weibull Cumulative Distribution Curves for PVP Aged in 65°C at for Different Aging Times

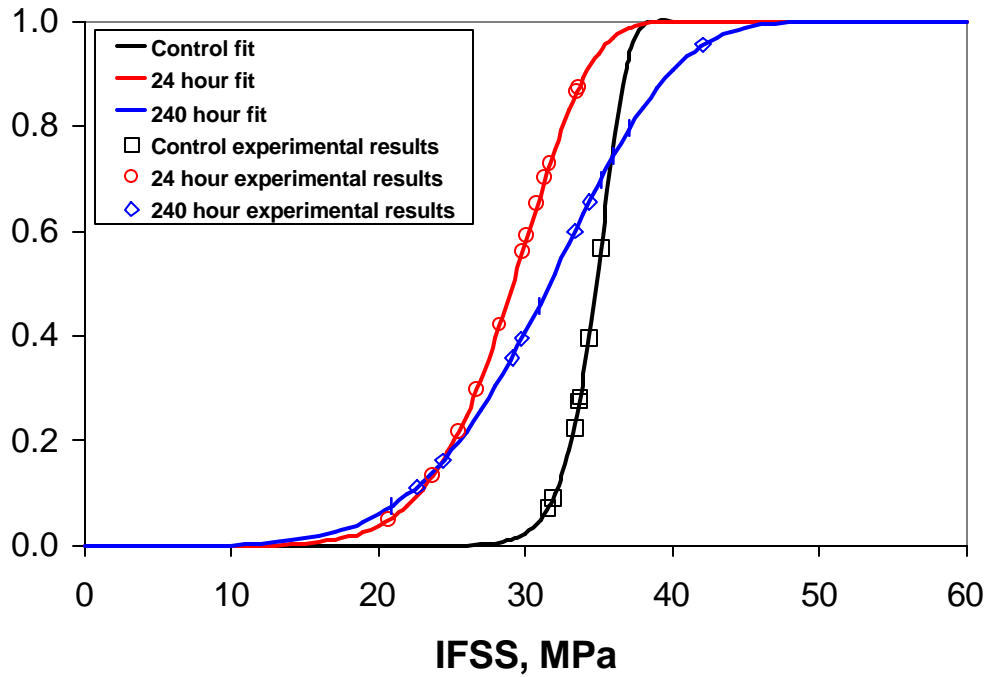


Figure 5-27. Weibull Cumulative Distribution Curves for G' Aged in 65°C at for Different Aging Times

In order to eliminate the effect of matrix/interphase swelling on the indentation results, samples removed at 288 and 576 hours were dried at 65°C in a vacuum oven for evaluation with nanoindentation. As shown in Figure 5-28, the LSP composite experienced very little change in interfacial adhesion after 288 hours of aging in both the wet and dry specimens. The wet specimen did however have a broader distribution of strength values as evident by a lower Weibull modulus. After 576 hours, Figure 5-29, the LSP composite began to show a noticeable decrease in interfacial shear strength. The wet curve maintained its lower Weibull modulus while the dry curve retained a higher mean value.

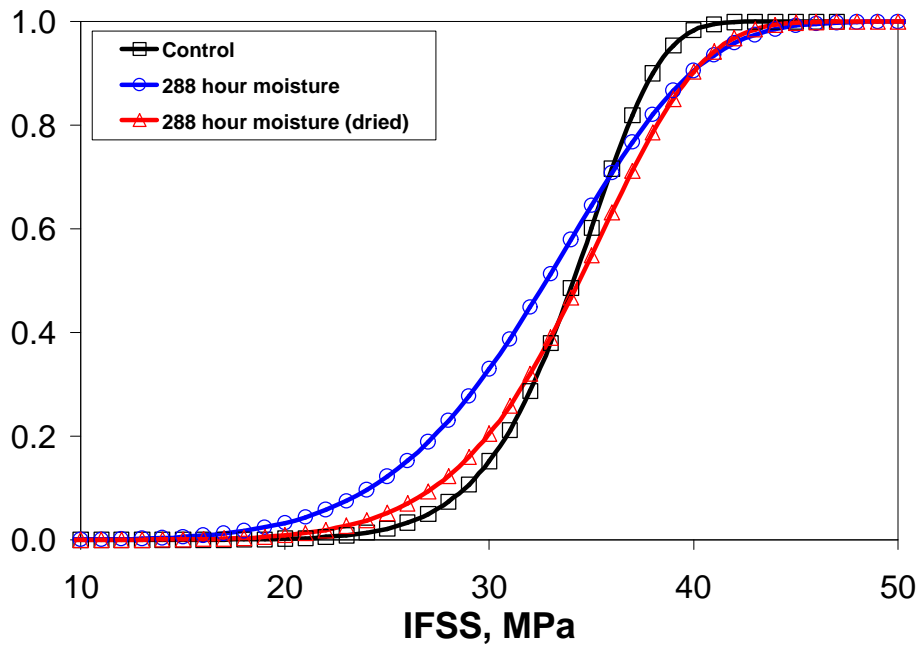


Figure 5-28. Weibull Cumulative Distribution Curves for LSP Aged 288 hours in a 65°C Water Bath, Tested Wet and Dry

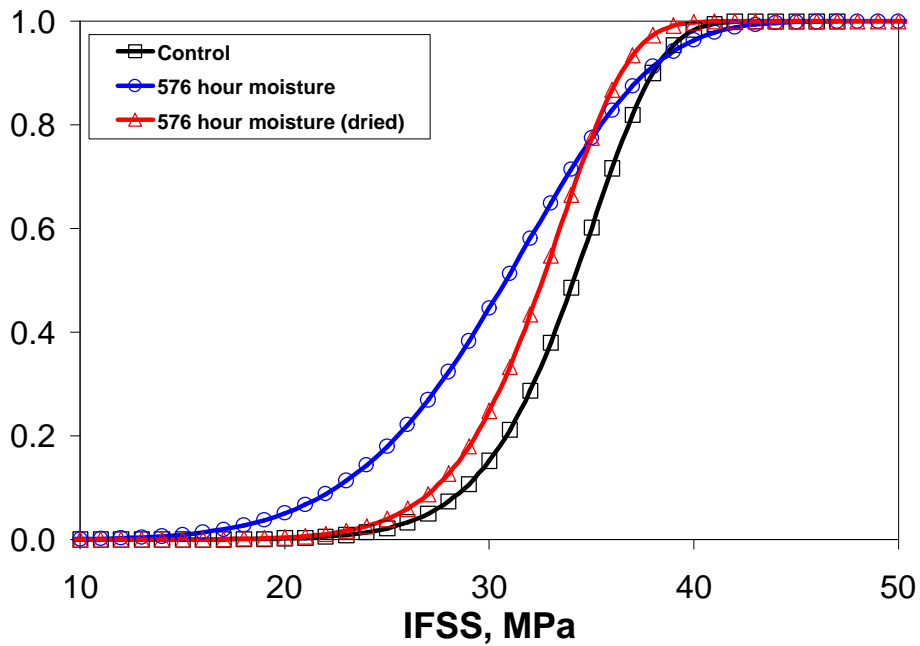


Figure 5-29. Weibull Cumulative Distribution Curves for LSP Aged 576 hours in a 65°C Water Bath, Tested Wet and Dry

PVP samples were also evaluated wet and dry after 288 and 576 hours of hydrothermal aging. The increase in interfacial adhesion observed by both the wet and dry specimens after 288 hours of exposure is shown in Figure 5-30. The wet curve again was very broad due to a low Weibull modulus. After 576 hours of aging, a further increase in interfacial adhesion occurred in both the wet and dry specimens as seen in Figure 5-31. Experimentally, this eliminates the idea that matrix/interphase swelling is the cause of the increase in interfacial shear strength in the PVP specimens.

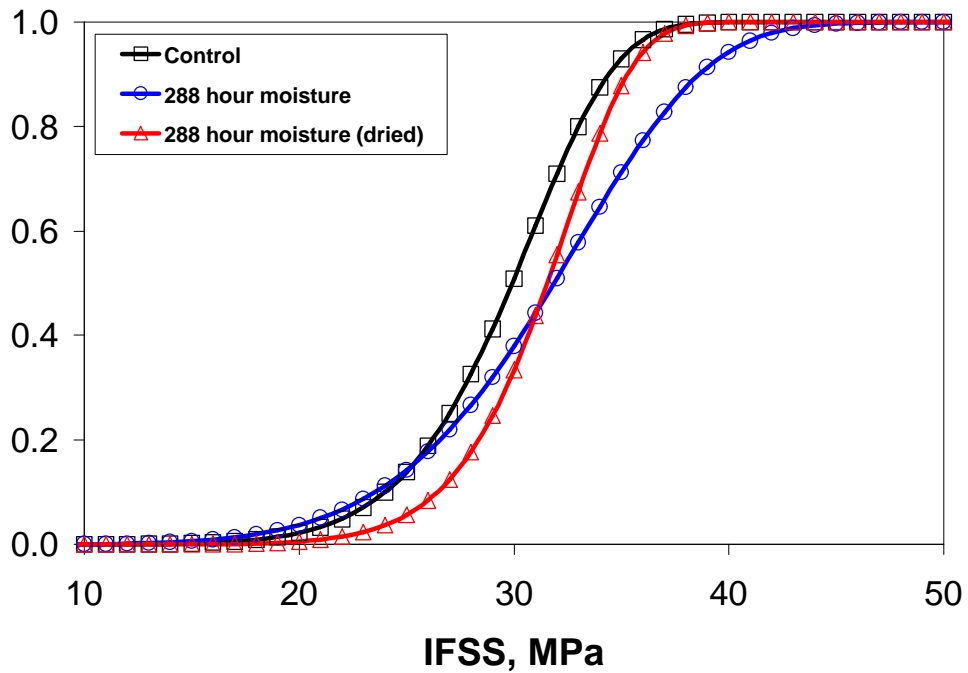


Figure 5-30. Weibull Cumulative Distribution Curves for PVP Aged 288 hours in a 65°C Water Bath, Tested Wet and Dry

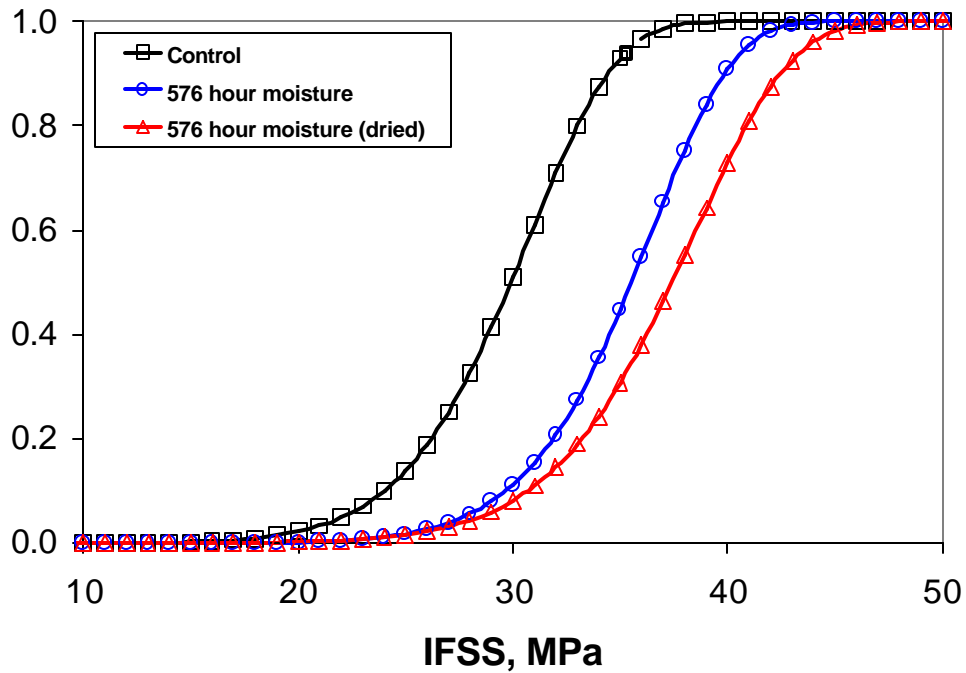


Figure 5-31. Weibull Cumulative Distribution Curves for PVP Aged 576 hours in a 65° C Water Bath, Tested Wet and Dry

5.4.2 Evaluation of Matrix Swelling using a Finite Element Analysis

A finite element analysis was conducted to determine the true effect of matrix swelling on interfacial shear strength. The G' material was modeled in this study because it was proven previously that the G' material produced better results in the finite element analysis. The properties from Table 5-2 were used with the addition of a parameter, β , relating the weight percent of moisture to strain in the material. The value of β for the vinyl ester material is $0.25 \text{ wt}\%^{-1}$. Assuming a moisture uptake of 0.8 wt% in the composite, the matrix absorbs 2.55 wt% with the assumption the carbon fibers do not absorb any water. The matrix expansion is modeled in ANSYS by setting the coefficient of thermal expansion, α , to β and loading the material with a change in temperature of 0.0255 ($\alpha\Delta T \rightarrow \beta\Delta M$, where $\alpha = \beta$ and $\Delta T = \Delta M$). The material was also loaded with the indenter at 30 mN. Two cases were evaluated: (1) a matrix thickness of 1.65 microns and (2) a matrix thickness of 5 microns.

As expected, matrix swelling causes an increase in radial stresses, the magnitude of which is governed by the matrix thickness. The increases in radial stresses occur within a fiber radius of the surface as seen in Figure 5-32. The effect of these stresses on interfacial shear stress and fiber translation is shown in Figure 5-33 and Figure 5-34. There are only minor effects at a matrix thickness of 1.65 microns, but at a matrix thickness of 5 microns, the results are significant. In this case, the maximum fiber translation is decreased 10.6% and the maximum interfacial shear stress is increased 39.9%. Experimentally, the decrease in maximum fiber translation would increase the global stiffness constant in the shear lag analysis.

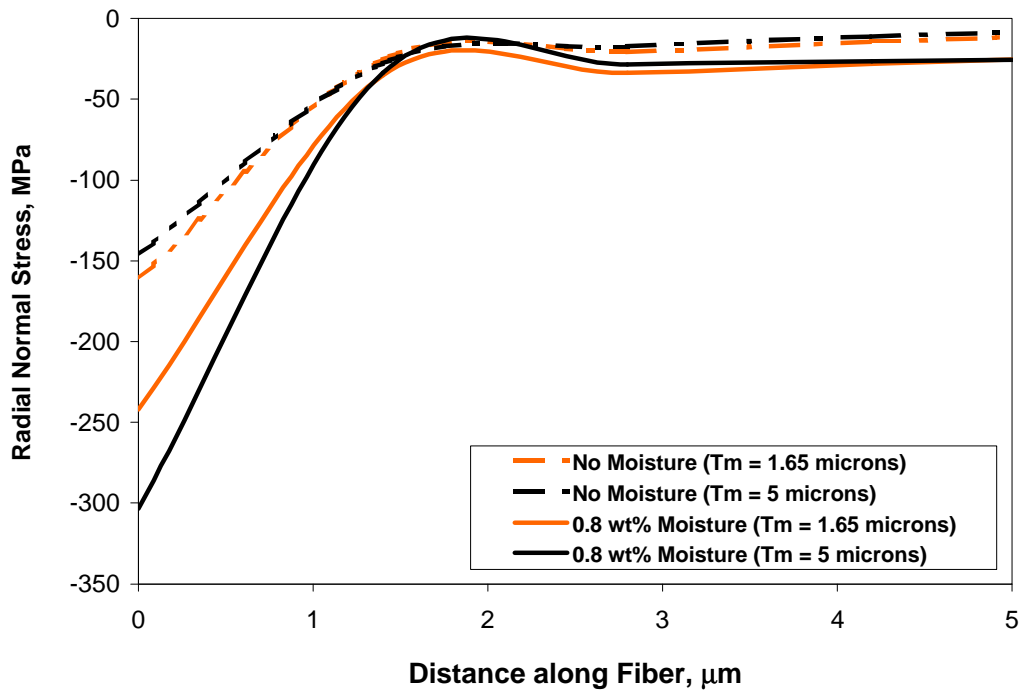


Figure 5-32. Increase in Radial Stresses on the Fiber due to Matrix Swelling

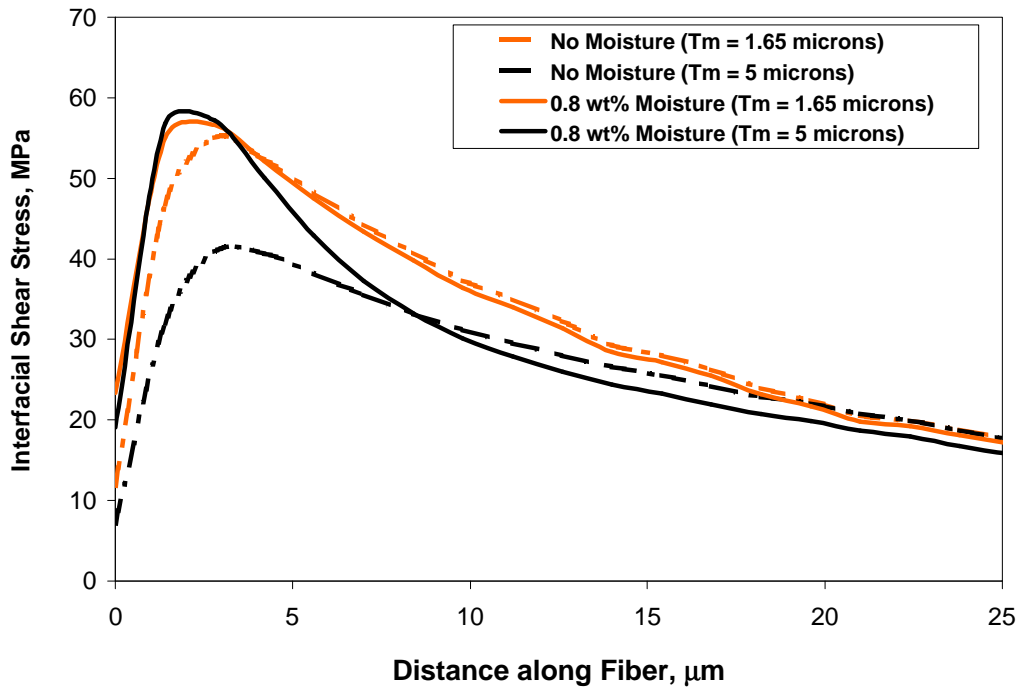


Figure 5-33. Change in Interfacial Shear Stresses due to Matrix Swelling

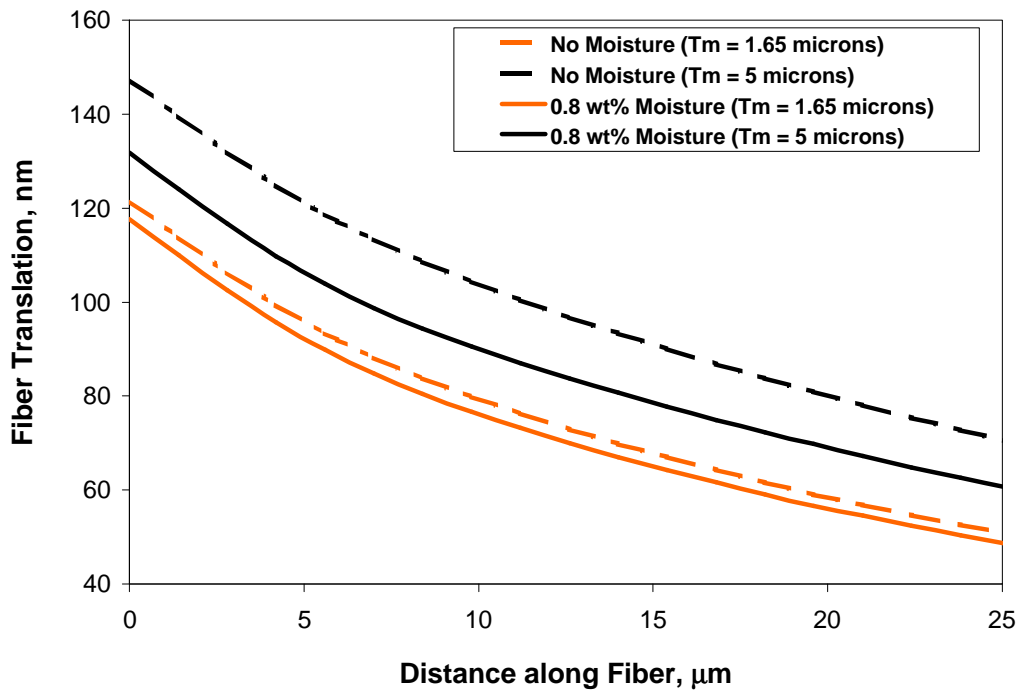


Figure 5-34. Change in Fiber Translation due to Matrix Swelling

In Figure 5-35 and Figure 5-36, finite element results are compared for two materials with equal global stiffness constants. The first material is loaded with 0.8 wt% moisture with a 5 micron matrix thickness, and the second material has no moisture with a 3 micron matrix thickness. Because of their similarities in fiber translation, these two fibers would appear identical experimentally under the initial loading when the global stiffness constant is obtained. The interfacial stresses, however, are drastically different with the moisture loaded sample having a maximum interfacial shear stress 17.6% higher than the no moisture sample. If the interfacial shear strengths are the same for the wet and dry material, then the higher interfacial stresses would result in a reduced debond load. Since the global stiffness constants are equal in this case, the moisture loaded interfacial shear strength, calculated by Equation 2-18, would be lower than the actual value. Therefore, it is expected that the wet samples will measure a lower interfacial shear strength than the dry ones. It is also expected that since there is a distribution of inter-fiber distances evaluated and moisture affects those different distances at different magnitudes, a broader distribution of interfacial shear strength values will be obtained. The experimental wet and dry data supports these conclusions as shown in Figure 5-28, Figure 5-29, Figure 5-30, and Figure 5-31.

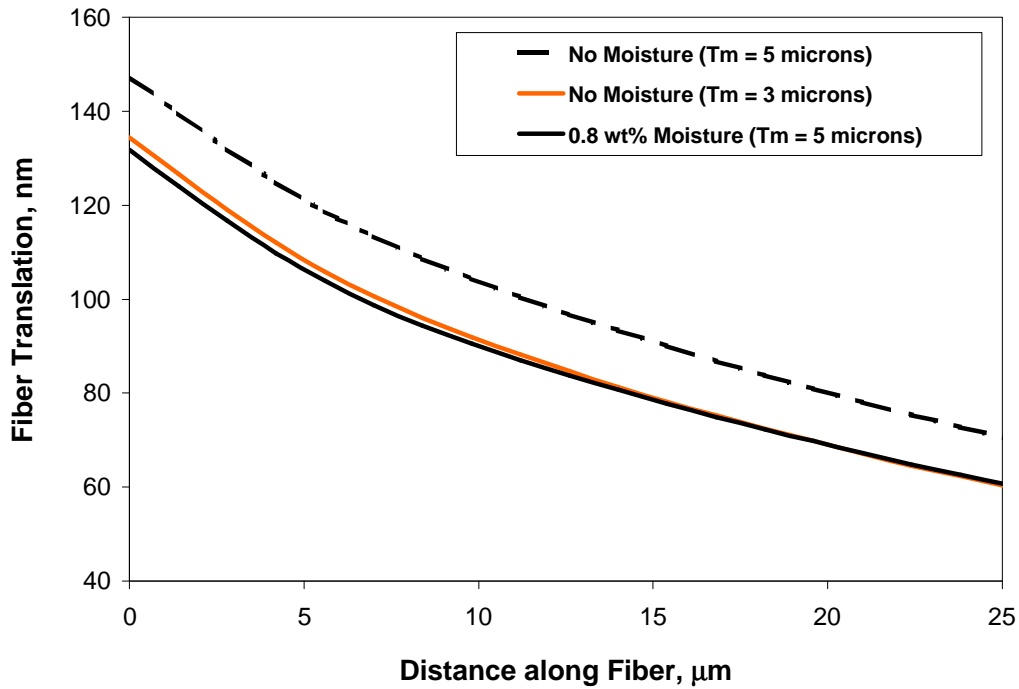


Figure 5-35. Translations of Fibers with Equivalent n values: (1) due to higher local volume fraction, (2) due to matrix swelling

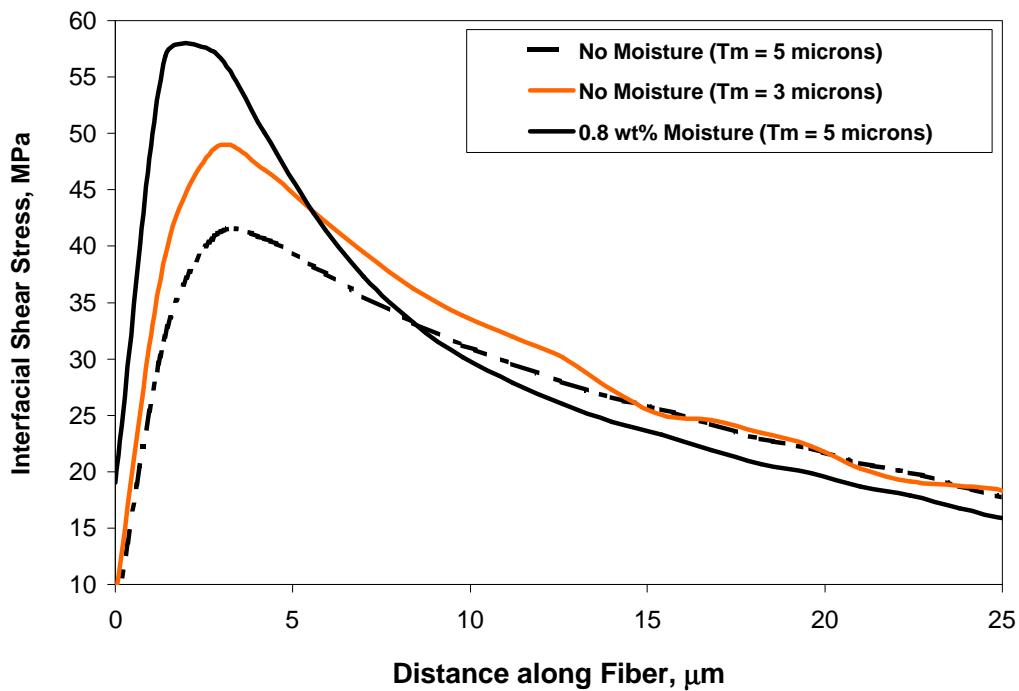


Figure 5-36. Interfacial Shear Stresses of Fibers with Equivalent n values: (1) due to higher local volume fraction, (2) due to matrix swelling

5.4.3 Comparison of IFSS to Tensile Strength in Hygrothermally Aged Samples

Tensile strengths were measured on the LSP and PVP materials aged 288 and 576 hours, both wet and dry. The purpose of this study is to compare the effects on interfacial shear strength to effects on tensile strength. The LSP material results are reported in Figure 5-37. The 288 hour wet and dry tensile strengths were respectively 5.4% and 4.3% less than the control sample. The interfacial shear strengths followed this same pattern with the dry strength higher than the wet strength. The same correlation continued at 576 hours of aging, where wet and dry tensile strengths dropped 7.4% and 4.5% respectively. There appears to be a strong connection between interfacial shear strength and tensile strength in the LSP material. The PVP material (Figure 5-38), however, shows a different trend. The dry tensile and interfacial shear strengths are again higher than the wet ones, but as the tensile strength goes down, the interfacial shear strength is increasing. For example, the 576 hour wet tensile strength drops 10.2%, while the interfacial shear strength increases 25.4%. These results demonstrate that interfacial adhesion alone does not control the strength of the material. A decrease in fracture toughness of the material in accordance with the increase in interfacial adhesion can cause transverse cracks to spread away from a fiber break, thus reducing composite tensile strength. From the evaluation of wet and dry specimens, there appears to be reversible and irreversible reductions in strength. The reversible part is related to matrix plasticization, which is not present in the dry samples, and the irreversible portion is related changes in interfacial properties, such as interphase toughness.

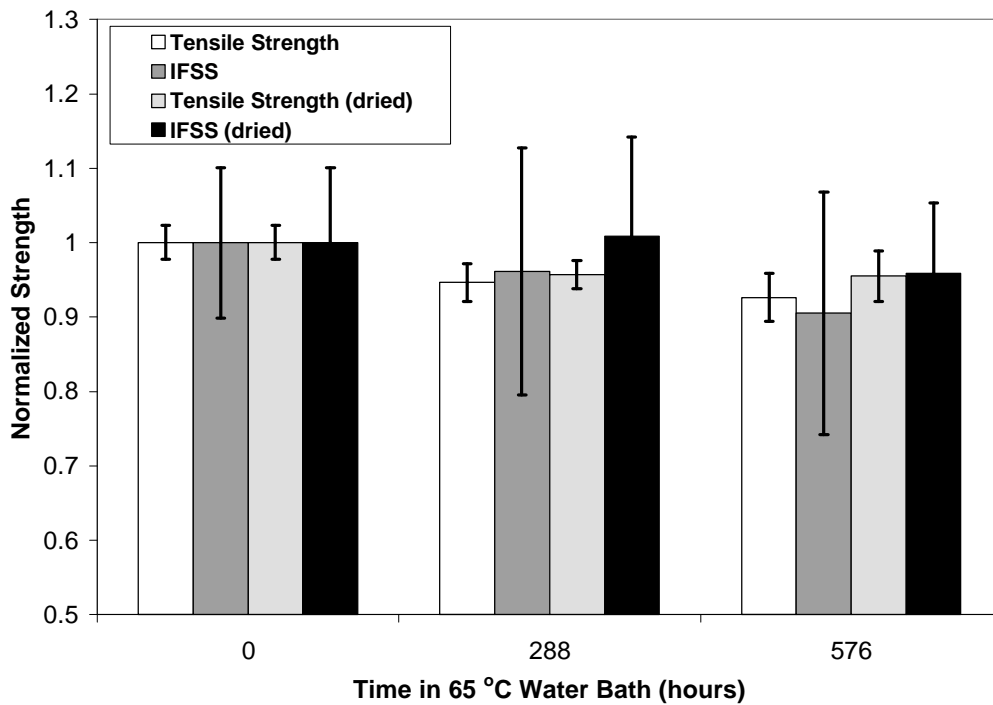


Figure 5-37. Comparison of LSP IFSS to Tensile Strength at Different Aging Times in a 65°C Water Bath

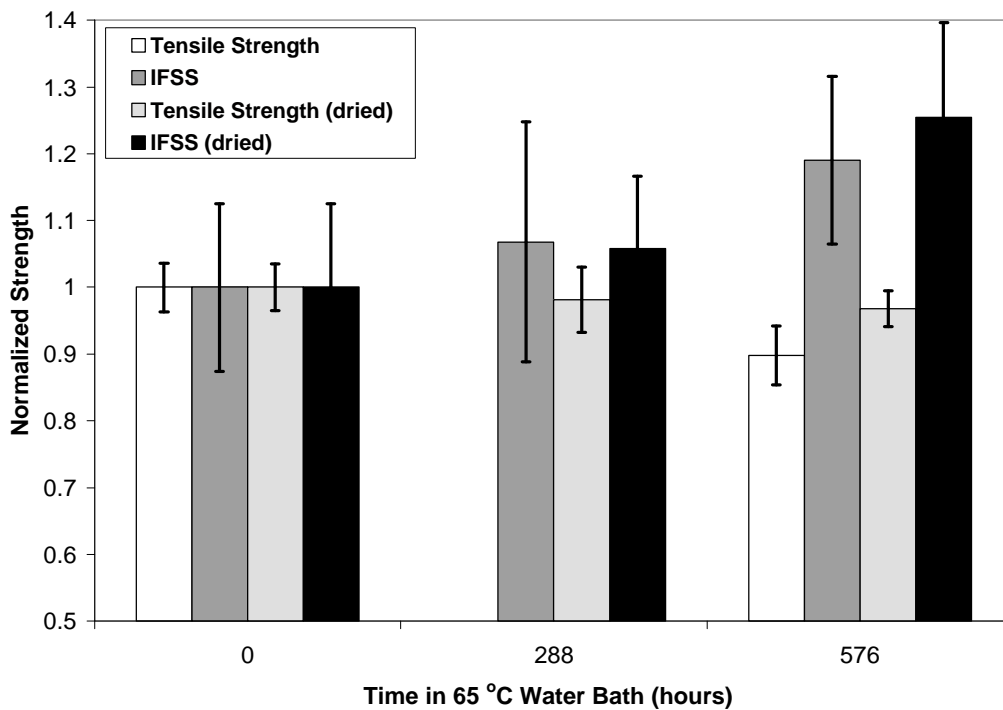


Figure 5-38. Comparison of PVP IFSS to Tensile Strength at Different Aging Times in a 65°C Water Bath

5.4.4 Tensile Strength Predictions

Tensile Strength predictions were made for the LSP and PVP materials at 288 and 576 hours of hygrothermal aging. Both wet and dry specimens were modeled, but the modulus was not changed for the wet composites to account for matrix plasticization due to moisture. The predictions were made using the model by Gao and Reifsnider [21], utilizing the MRLife12™ software [22]. The fiber, matrix, and composite model inputs are reported in Table 5-5 and the interfacial shear strength values are reported in Table 5-6. The results, shown in Figure 5-39 and Figure 5-40, demonstrate that these small changes in interfacial shear strength have little impact on the predicted tensile strength. Although these predictions are all within 7% of the measured tensile strength values, they do not follow the same trends. The clearest example of this is in the PVP material where the predicted tensile strength increases with the measured interfacial shear strength values while the measured tensile strength values decrease considerably. There is certainly another mechanism, such as interphase toughness, affecting composite strength with regard to moisture that is not included in the tensile strength model or measured by the nanoindentation test.

Table 5-6. Interfacial Shear Strength Values for Hygrothermally Aged Specimens

Exposure Time (hours)	LSP (MPa)	PVP (MPa)
0	33.7	29.5
288 wet	32.4	31.5
288 dry	34.0	31.2
576 wet	30.5	35.1
576 dry	32.3	32.4

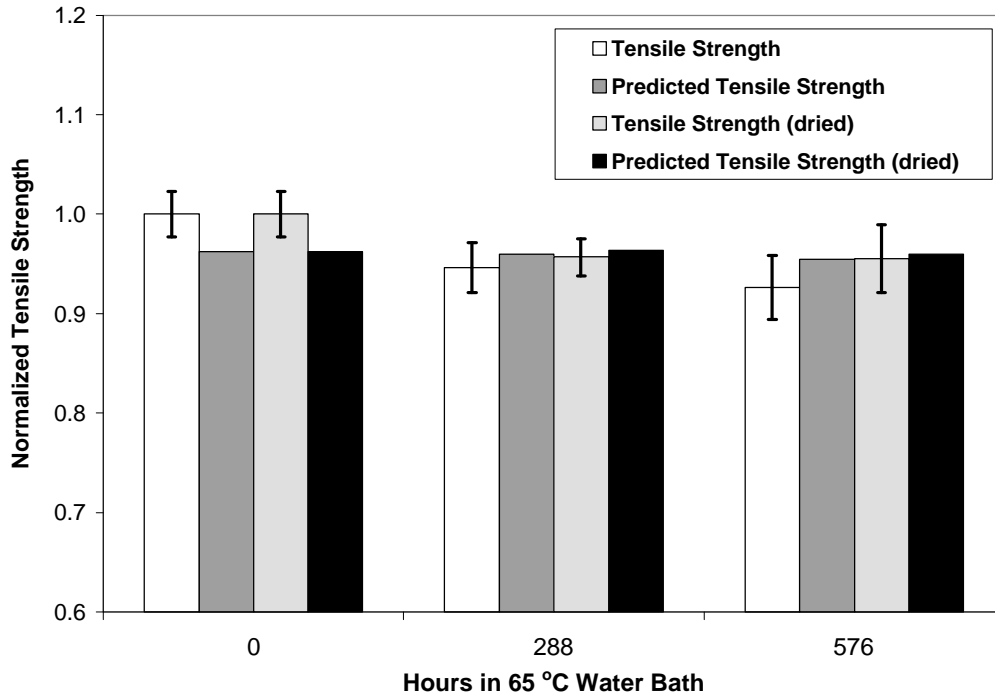


Figure 5-39. Comparisons of Actual Tensile Strengths and Predicted Tensile Strengths from IFSS Results for LSP Material at Different Aging Times

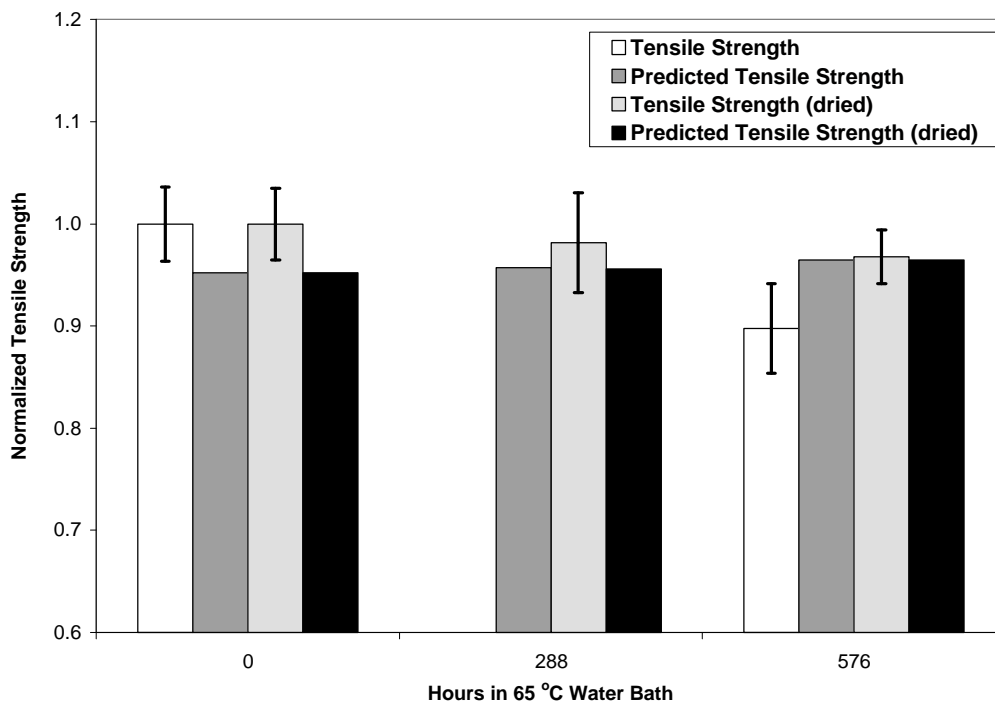


Figure 5-40. Comparisons of Actual Tensile Strengths and Predicted Tensile Strengths from IFSS Results for PVP Material at Different Aging Times

5.5 Effect of Mechanical Fatigue on IFSS and Composite Strength

A preliminary investigation was conducted to determine the effect of mechanical fatigue cycles on interfacial shear strength and bulk composite tensile strength. The specimens were subjected to tensile-tensile fatigue to 75% life at 50% their respective ultimate tensile strengths. The analysis was conducted on the G' and LSP materials. The G' material showed a 27% reduction in interfacial shear strength and a 16% reduction in tensile strength. The LSP material's interfacial shear strength dropped 9% with no reportable reduction in tensile strength. Weibull analysis results for both these materials is shown in Figure 5-41. Although these are preliminary results, it is evident that the degradation of the G' fiber/matrix interphase is at least partly responsible for the reduction in residual strength.

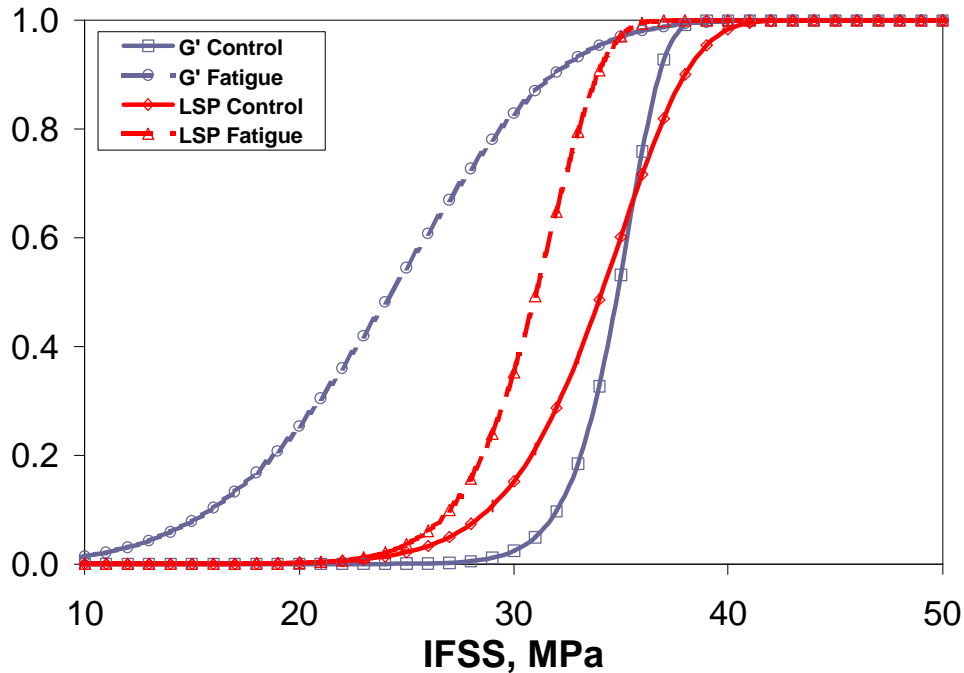


Figure 5-41. Weibull Cumulative Density Curves for LSP and G' Composites: Control versus Mechanically Fatigued

Chapter 6 Conclusions

6.1 Conclusions

6.1.1 Evaluation of Technique and Analysis Methods

The blunt tipped nanoindenter proved to provide the stress-state and resolution necessary to perform reliable microindentation tests. The instrument produced results quickly and with ease. The debond load was extracted from the load-displacement curve readily with the use of the shear lag curve fitting technique, eliminating the need for optical evaluation. As seen from the progressive nature of debonding, it is important to rely on methods other than optical ones for determining the debond load. The conversion of the debond load to the interfacial shear strength is questionable using the same shear lag technique due to the assumptions involved. The finite element analysis revealed the faults of the shear lag analysis, including its inability to handle radial stresses on the fiber and the assumption that the shear stress does not go to zero at the free surface. In fact, the stress-state is so complicated at the end of the fiber the finite element analysis is suspect as well. **The heavy dependence on fiber diameter (13.7 MPa $\Delta\tau$ per 1 μm change fiber diameter), location of the indenter on the fiber, interfiber spacing (4.1 MPa $\Delta\tau$ per 1 μm change in matrix thickness), and interphase properties make it extremely difficult to compare the finite element solution to any experimental results.** Therefore, the goal of determining actual interfacial shear strength values on as-processed composites was not fulfilled, but as with most microindentation results, the results are good for comparison.

6.1.2 Comparison of Fiber Sizings

The study of the G', LSP and PVP materials showed that the G' and LSP fibers outperform the PVP fiber in interfacial adhesion by 13%. The LSP and G' results were statistically equivalent. Results from the microbond test do not agree completely with the nanoindentation test but do show the same increase between the LSP and PVP fibers. Tensile strength results, expected to be highly dependent on interfacial shear strength, also do not follow the same trends in interfacial shear strength, especially with the G' composite. It

is expected that the poor tensile strength result in comparison with its interfacial shear strength result is a product of poor processing. Tensile strength predictions were within 5% of the LSP and PVP materials but only within 29% of the G' composite, again a result of poor processing. **Despite the success in predicting the tensile strengths for the LSP and PVP materials, the interfacial shear strength played a minor role and has little impact on the results.**

6.1.3 Effects of Hygrothermal Aging on IFSS and Composite Strength

Hygrothermal aging on the composites revealed interesting information about interfacial adhesion and the effectiveness of the shear lag evaluation method on samples with matrix swelling. Interfacial shear strengths initially increased in the LSP material before decreasing to below the original unaged value. It is believed that the combination of moisture and temperature causes improved interfacial adhesion numbers before degradation begins. It was not proved that tensile strengths increased at low levels of hygrothermal aging, but tensile strength values did decrease in accordance with the decrease in interfacial shear strength at longer aging times. The PVP material also experienced an increase in interfacial adhesion at short aging times, but in this case, the increase was maintained at longer aging times. Again, it is believed that the increase in interfacial shear strength is the result of changes in the material due to moisture and temperature, but in this case no degradation of the interphase occurred. These results do contradict, however, the dramatic tensile strength reductions observed in the PVP material aged at long times. It is possible that the mechanism responsible for improvement in interfacial adhesion causes a reduction in fracture toughness that leads to transverse cracking and rapid debond propagation on the fibers that do debond. A finite element analysis of the system, along with experimental data, showed that matrix swelling causes an observed decrease in interfacial shear strength, therefore, eliminating matrix swelling as the cause for improved interfacial adhesion. **From the evaluation of wet and dry specimens, there appears to be reversible and irreversible reductions in strength. The reversible part is related to matrix plasticization, which is not present in the dry samples, and the irreversible portion is related changes in interfacial properties, such as interphase toughness. Interfacial shear strength plays a minor role in composite strength at the values studied; a statement confirmed by the**

tensile strength model, which shows only small changes in strength as a result of the observed changes in interfacial shear strength.

6.1.4 Summary

This work demonstrated the effective use of the nanoindenter to obtain excellent microindentation results where the debond load could be extracted directly from the experimental load-deflection curve with only the knowledge of the fiber properties. The results showed that although the LSP material outperforms the PVP and G' materials in bulk composite properties, it is equivalent in interfacial shear strength to G' and experiences hygrothermal degradation in interfacial adhesion that the PVP does not. The relationship between tensile strength and interfacial adhesion proved to be small as predicted in the tensile strength model, but processing defects and other failure processes showed their strong influences over tensile strength. Interfacial adhesion is important in composite materials, but in the case of G', LSP and PVP materials other factors such as processing and interphase toughness dominated performance.

6.2 Recommendations for Future Work

A full and complete investigation into the mechanics of the microindentation test needs to be completed in order to satisfactorily obtain true interfacial shear strength values. Experiments run under controlled conditions, such as on model composites, should be included in this work. The true interfacial adhesion value would provide another building block in the improvement of tensile strength models. New models must take into account the effects of processing and fracture processes in order to accurately predict tensile strength values.

Additional testing at longer times of hygrothermal aging would provide better insight into the degradation behavior of the interphase. It would also be interesting to evaluate the interfacial adhesion based on location in the composite. The work presented here tested fibers near the surface but did not track the degradation into the thickness of the composite.

A more comprehensive look at the relationship between mechanical fatigue and interfacial adhesion should be explored as well. In mechanical fatigue, the changes in chemistry associated with moisture and temperature are avoided, thus providing a simpler look at how interphase degradation affects residual strength.

Finally, glass fiber-reinforced polymer composites should be studied due to their importance in low-cost composite structures. Glass fibers are known to experience significant reductions in interfacial adhesion do to moisture exposure. It would be useful to researchers to probe these composites under various environmental conditions in an effort to improve them for practical use without the expense and labor involved in a full-scale testing program.

References

- [1] Hayes, M.D., J.J. Lesko, J. Haramis, T.E. Cousins, J. Gomez, P. Massarelli, "Laboratory & Field Characterization of the Tom's Creek Bridge Composite Superstructure," *Journal for Composites and Construction*, Vol. 4, No. 3, August 1999, pp. 120-128.
- [2] Neely, W.D., "Evaluation of the In-Service Performance of the Tom's Creek Bridge," M.S. Thesis, Virginia Tech, May 2000.
- [3] Temeles, A.B., T.E. Cousins, and J.J. Lesko, "Composite Plate & Tube Bridge Deck Design: Evaluation in the Troutville, Virginia Weigh Station Test Bed," *Proceedings of the Advanced Composite Materials in Bridges and Structures 3rd International Conference*, Ottawa, Ontario, Canada, August 15-18, 2000, pp. 801-808.
- [4] Temeles, A.B., "Field and Laboratory Tests of a Proposed Bridge Deck Panel Fabricated from Pultruded Fiber-Reinforced Polymer Components," M.S. Thesis, Virginia Tech, May 2001.
- [5] Broyles, N.S., K.N.E. Verghese, R.M. Davis, J.J. Lesko, and J.S. Riffle, "Pultruded Carbon Fiber/Vinyl Ester Composites Processed with Different Fiber Sizing Agents Part I: Processing and Static Mechanical Performance," *Journal of Composites for Construction* (accepted), 2001.
- [6] Bump, M.M.B., "The Effect of Chemistry and Network Structure on Morphological and Mechanical Properties of Diepoxide Precursors and Poly(hydroxyethers)," Ph.D. Dissertation, Virginia Tech, May 2001.
- [7] ASTM 3410/D 3410M-95, "Standard Test Method for Compressive Properties of Polymer Matrix Composite Materials with Unsupported Gage Section by Shear Loading," *Annual Book of ASTM Standards*, Vol. 15.03. pp. 117-132.
- [8] Verghese, K.N.E, N.S. Broyles, J.J. Lesko, R.M. David, and J.S. Riffle, "Pultruded Carbon Fiber/Vinyl Ester Composites Processed with Different Fiber Sizing Agents Part III: Theoretical Aspects," *Journal of Composites for Construction* (accepted), 2001.
- [9] Verghese, K.N.E, N.S. Broyles, J.J. Lesko, R.M. David, and J.S. Riffle, "Pultruded Carbon Fiber/Vinyl Ester Composites Processed with Different Fiber Sizing Agents Part II: Enviro-mechanical Durability," *Journal of Composites for Construction* (accepted), 2001.

- [10] Herrera-Franco, P.J., and L.T. Drzal, "Comparison of methods for the measurement of fibre/matrix adhesion in composites," *Composites*, Vol. 23, No. 1, January 1992, pp. 2-27.
- [11] Narkis, M., E.J.H. Chen, and R.B. Pipes, "Review of Methods for Characterization of Interfacial Fiber-Matrix Interactions," *Polymer Composites*, Vol. 9, No 4., August 1988, pp. 245-251.
- [12] Miller, B., P. Muri, and L. Revenfeld, "A microbond method for determination of the shear strength of a fiber/resin interface," *Composites Science and Technology*, Vol. 28, 1987, pp. 17-32.
- [13] Rao, V., and L.T. Drzal, "The Dependence of Interfacial Shear Strength on Matrix and Interphase Properties," *Polymer Composites*, Vol. 12, No. 1, February 1991, pp. 48-56.
- [14] Mandell, J.F., D.H. Grande, T. Tsiang, and F.J. McGarry, "Modified Microbonding Test for Direct *In Situ* Fiber/Matrix Bond Strength Determination in Fiber Composites," *Composite Materials: Testing and Design, ASTM STP 893*, 1986, pp. 87-108.
- [15] Desaegeer M., and I. Verpoest, "On the Use of the Micro-Indentation Test Technique to Measure the Interfacial Shear Strength on Fibre-Reinforced Polymer Composites," *Composite Science and Technology*, Vol. 48, 1993, pp. 215-226.
- [16] Ho, H., and L.T. Drzal, "Evaluation of interfacial mechanical properties of fiber reinforced composites using the microindentation method," *Composites Part A*, Vol. 27A, 1996, pp. 961-971.
- [17] Xu, L., and L.T. Drzal, "Influence of Interphase Chemistry on the Adhesion between Vinyl Ester Resin and Carbon Fibers," *Proceedings of the 23rd Annual Adhesion Society Meeting*, Myrtle Beach, SC, 2000, pp. 183-185.
- [18] Kharrat M., A. Chateauinois, L. Carpentier, and P. Kapsa, "On the interfacial behaviour of a glass/epoxy composite during a micro-indentation test: assessment of interfacial shear strength using reduced indentation curves," *Composites Part A*, Vol. 28A, pp. 39-46.
- [19] Zidi, M., L. Carpentier, A. Chateauinois, and F. Sidoroff, "Quantitative analysis of the micro-indentation behaviour of fibre-reinforced composites: development and validation of an analytical model," *Composites Science and Technology*, Vol. 60, 2000, pp. 429-437.
- [20] Zidi, M. L. Carpentier, A. Chateauinois, P. Kapsa, and F. Sidoroff. "Development of a micro-indentation model simulating different mechanical responses of the

- fibre/matrix interface,” *Composites Science and Technology*, Vol. 61, 2001, pp. 369-375.
- [21] Gao, Z. and K.L. Reifsnider, “Tensile Failure of Composites: Influence of Interface and Matrix Yielding,” *Journal of Composites Technology & Research*, Vol. 14, No. 4, Winter 1992, pp. 201-210.
- [22] Case, S.W., and K.L. Reifsnider, *MRLife12: Simulation of Performance & Life Prediction for Composite Laminates*, Materials Response Group, Virginia Polytechnic Institute and State University, Blacksburg, VA, 1999.
- [23] Batdorf, S. B., “Tensile Strength of Unidirectionally Reinforced Composites I and II,” *Journal of Reinforced Plastics and Composites*, Vol. 1., April 1982, pp. 153-176.
- [24] Subramanian, S., K.L. Reifsnider, and W.W. Stinchcomb, “Tensile Strength of Unidirectional Composites: The Role of Efficiency and Strength of Fiber-Matrix Interface,” *American Society for Testing and Materials*, 1995, pp. 289-300.
- [25] Broyles, N.S., “Thermoplastic Sizings: Effects on Processing, Mechanical Performance, and Interphase Formation in Pultruded Carbon Fiber/Vinyl Ester Composites,” Ph.D. Dissertation, Virginia Tech, December 1999.
- [26] *AS4 Technical Product Information*, Hexcel, Inc., <http://www.hexcelfibers.com/index-mp.html>.
- [27] Dow Chemical Company. “DERAKANE Epoxy Vinyl Ester Resins: Technical Product Information,” 1996.
- [28] ASTM D 3039/D 3039M – 95a, “Standard Test Method for Tensile Properties of Polymer Matrix Composite Materials,” *Annual Book of ASTM Standards*, Vol. 14.02. pp. 99-109.
- [29] George Blann, Buehler LTD., Personal Communication.
- [30] Gregory Swadener, Oak Ridge National Laboratory, Personal Communication.
- [31] Weibull and Waloddi, “A Statistical Distribution Function of Wide Applicability,” *Journal of Applied Mechanics*, 1951, pp. 293-297.
- [32] Weibull and Waloddi, “A Statistical Representation of Fatigue Failures in Solids,” *Transitions of the Royal Institute of Technology* 27, Stockholm, Sweden, 1949.
- [33] Gao, Y., Y. Mai, and B. Cottrell, “Fracture in fiber-reinforced materials,” *Journal of Applied Mathematics and Physics*, Vol. 39, July 1988, pp. 550-572.

[34] Hyun Man Kang, Kwangju Institute of Science and Technology, Personal Communication.

[35] Haeberle, D.C., J.J. Lesko, and S.W. Case, "Enviro-mechanical Changes in the Interphase Properties and Relationships to Composite Durability," *Proceeding of SAMPE 2001: A Materials and Processes Odyssey*, Long Beach, CA, May 6-10, 2001.

Vita

David Claibourne Haeberle was born in Huntington, WV in 1976 to Ron and Harriet Haeberle. He graduated from Huntington East High School in 1994 before heading to Virginia Tech in Blacksburg, VA to pursue his undergraduate degree. While an undergraduate at Virginia Tech, David was active in the Society of Engineering Sciences, the Student Engineers' Council, and the German Club, a local service fraternity. He also participated in the co-op program, working three semesters for DuPont Tyvek[®] in Richmond, VA performing research and product development. David completed his B.S. in Engineering Science and Mechanics in May of 1999 and stayed at Virginia Tech to complete his MS degree in Engineering Mechanics. Following graduation in June of 2001, he will begin work for ExxonMobil in Houston, TX for their Upstream Research Company in the Wells and Materials Division.